Universidad de Huelva

Departamento de Geología

Trace elements mobility during the early diagenesis of iron precipitates in acid drainage systems

Memoria para optar al grado de doctor
presentada por:

Pablo Cruz Hernández

Fecha de lectura: 18 de noviembre de 2016

Bajo la dirección de los doctores:

Rafael Pérez López

Matthew B. J. Lindsay

José Miguel Nieto Liñán

Huelva, 2016

Trace elements mobility during the early diagenesis of iron precipitates in acid drainage systems

Movilidad de los metales traza durante la diagénesis temprana de precipitados de hierro en sistemas de drenaje ácido

Memorandum presented by PABLO CRUZ HERNÁNDEZ, under the supervision of Dr. RAFAEL PÉREZ LÓPEZ, Dr. MATTHEW B. J. LINDSAY and Dr. JOSÉ MIGUEL NIETO LIÑÁN, to obtain the International PhD Degree.

This thesis has been performed within the framework of the doctoral program "Ciencia y Tecnología Industrial y Ambiental" under the research line "Geología y Gestión Ambiental de los Recursos Minerales" at the Department of Earth Sciences (Facultad de Ciencias Experimentales, Universidad de Huelva).

PhD candidate

PABLO CRUZ HERNÁNDEZ

Directors:

RAFAEL PÉREZ LÓPEZ
Ramón y Cajal Fellowship
Departamento de Geología
Universidad de Huelva

MATTHEW B. J. LINDSAY
Assistant Professor
Department of Geological Sciences
University of Saskatchewan

JOSÉ MIGUEL NIETO LIÑÁN
Associated Professor
Departamento de Geología
Universidad de Huelva

Huelva, November 2016

Trace elements mobility during the early diagenesis of iron precipitates in acid drainage systems

Movilidad de los metales traza durante la diagénesis temprana de precipitados de hierro en sistemas de drenaje ácido

Pablo Cruz Hernández
Noviembre de 2016

La presente tesis ha sido financiada por el proyecto METODICA "*El ciclo de los metales y su impacto en la calidad de las aguas en la cuenca del río Odiel*" (CGL2010-21956-C02-02) del Ministerio de Ciencia e Innovación del gobierno de España, convocatoria Proyectos I+D+i 2010. Además, esta tesis también ha sido cofinanciada por el proyecto EMPATIA "*Estabilidad de metales en precipitados de drenajes ácidos de mina; uso sostenible e implicaciones ambientales*" (CGL2013-41862-C02-01-K) del Ministerio de Economía y Competitividad del gobierno de España convocatoria Proyectos I+D+i 2013.

El doctorando ha disfrutado de un contrato predoctoral del programa de Formación de Personal Investigador (FPI) del ministerio de Ciencia e Innovación (Contrato BES-2011-048173).

El trabajo se ha llevado a cabo fundamentalmente en la Facultad de Ciencias Experimentales de la Universidad de Huelva. Parte del trabajo se realizó gracias a dos estancias en el "*Department of Geological Sciences*" de la "*University of Saskatchewan*", ambas financiadas por los proyectos del Ministerio de Economía y Competitividad (EEBB-I-13-07137 y EEBB-I-14-08645) asociados al contrato predoctoral FPI. Los experimentos de radiación sincrotrón se llevaron a cabo en líneas del "*Canadian Light Source (CLS)*" en Saskatoon (Canadá) y el "*Argonne National Laboratory Advance Photon Source (APS)*", ambos financiados por los proyectos EEBB. Por otro lado, los experimentos en la línea ID15 (experimento MA-1754) del "*European Synchrotron Radiation Facility (ESRF)*" fueron financiados por el propio ESRF.

A mis hermanos, mi padre,
mi madre y las otras seis
enanitas de Blancanieves.

-Mamá, ¿Por qué usan ese Río como un medio marciano?

-Es el Río Tinto, que por culpa de los minerales es rojo y está ácido, y hace que sea único en el mundo y parezca marciano.

-Y, ¿por qué está rojo?

-Porque la pirita se disuelve y el hierro lo vuelve así.

-Qué chulo… Mamá, cuando yo sea mayor, ¿voy a poder ir a verlo?

-Claro Pablo, tu estudia mucho, verás que algún día podrás ir.

Cabezón de la Sal, Septiembre 1991

Mira, Platero, cómo han puesto el río entre las minas, el mal corazón y el padrastreo. Apenas si su agua roja recoge aquí y allá, esta tarde, entre el fango violeta y amarillo, el sol poniente; y por su cauce casi sólo pueden ir barcas de juguete. ¡Qué pobreza!

Antes, los barcos grandes de los vinateros, laúdes, bergantines, faluchos —El Lobo, La Joven Eloísa, el San Cayetano, que era de mi padre y que mandaba el pobre Quintero, La Estrella, de mi tío, que mandaba Picón—ponían sobre el cielo de San Juan la confusión alegre de sus mástiles—¡sus palos mayores, asombro de los niños!—; o iban a Málaga, a Cádiz, a Gibraltar, hundidos de tanta carga de vino... Entre ellos, las lanchas complicaban el oleaje con sus ojos, sus santos y sus nombres pintados de verde, de azul, de blanco, de amarillo, de carmín... Y los pescadores subían al pueblo sardinas, ostiones, anguilas, lenguados, cangrejos... El cobre de Riotinto lo ha envenenado todo. Y menos mal, Platero, que con el asco de los ricos, comen los pobres la pesca miserable de hoy... Pero el falucho, el bergantín, el laúd, todos se perdieron.

¡Qué miseria! ¡Ya el Cristo no ve el aguaje alto en las mareas! Sólo queda, leve hilo de sangre de un muerto, mendigo harapiento y seco, la exangüe corriente del río, color de hierro igual que este ocaso rojo sobre el que La Estrella, desarmada, negra y podrida, al cielo la quilla mellada, recorta como una espina de pescado su quemada mole, en donde juegan, cual en mi pobre corazón las ansias, los niños de los carabineros.

El río, Platero y yo. XCV. Juan Ramón Jiménez

ABSTRACT

Both mining and industrial activities are the main pollution sources for the environment. However, many of these processes have a natural origin, as in the case of the acid rock drainage (ARD). The ARD results from the exposure of metal sulfide minerals to atmospheric conditions. When interacting with meteoric water, oxidative dissolution of sulfides releases protons, metals and sulfates to solution and provokes the acidification of the environment. Acid mine drainage (AMD) is a leaching process derived from the mining activity increasing this effect provoked by ARD. The main metallic sulfide mineral associated with AMD environments is pyrite [FeS_2], yet it is commonly associated with other sulfides as arsenopyrite [$FeAsS$], chalcopyrite [$CuFeS_2$], galena [PbS], or sphalerite [ZnS]. Many of the metal(loid)s (from now on metals) hosted by sulfides are thought to be toxins for the environment, making its control something important. One of the main metallogenic provinces of massive sulfide deposits in the world is located at the SW of the Iberian Peninsula, in the Iberian Pyrite Belt (IPB), where the mining activity dates back to Pre-Roman times.

Even so, the huge discharge of contaminants to the water causes the formation of a series of low-crystallinity mineral phases that are able to retain metal traces. Schwertmannite [$Fe_8O_8(OH)_{(8-2x)}(SO_4)_x \cdot nH_2O; 1 \leq x \leq 1.75$] is the nano-crystalline Fe oxy-hydrosulfate that spontaneously precipitates, creating sedimentary terraces in waters affected by AMD and buffering the pH between 2 and 4. Its poor crystallinity leads to two characteristics (1) it can capture a high quantity of trace metals from solution and (2) as it is a metastable phase, it is easily and rapidly transformed into goethite [$FeOOH$] and jarosite [$KFe_3(SO_4)_2(OH)_6$], and at long-term into hematite [Fe_2O_3]. The behavior of the trace metals previously retained by schwertmannite during its transformation is a focus for discussion in the scientific community; it is here where the present thesis is framed.

Several samples at different maturation stages were collected and chemically and mineralogically characterized by micro-Raman spectroscopy, reflected optic microscope, X-ray diffraction (XRD), scanning electron microscopy (SEM), electronic probe micro-analyzer (EPMA) and total acid digestion. In AMD environments, newly-formed terraces were observed to be composed by schwertmannite in the early stage, which was formed on the riverbed, trapping As from the solution. It was also noticed that as going deeper in a terrace profile goethite and, eventually, jarosite appear, being finally goethite the predominant phase at deeper levels. After diagenetic maturation, fossil terraces were composed by highly crystalline goethite and hematite. It is shown in this study that μ-Raman is a useful tool for the mineralogical characterization of Fe(III) phases, for oxides, hydroxides, and oxy-hydroxysulfates. However, it was not possible to detect the As incorporation to the structure, due to the low As concentration in the natural precipitates.

In a second study, representative samples of the extreme diagenetic stages were used; a sample of a present-day terrace and an old terrace. The samples were mineralogically characterized by μ-Raman. Moreover, acid digestions of the samples were done, as well as

microprobe analysis and, most importantly, X-ray fluorescence maps with synchrotron radiation (μ-XRF) focalized on those ranges of major trace metals; As, Cu, Zn. The high number of data obtained was analyzed using statistic techniques such as principal component analysis (PCA). A progressive loss of metal affinity of the trace metals was detected with PCA in favor of the main element, Fe, as the phases were more crystalline (Fe R^2 schwertmannite > goethite > crystalline goethite >> hematite).

Finally, experiments with synthetic samples were performed in order to simulate the diagenetic transformation processes of schwertmannite. Schwertmannite was precipitated at different temperatures (40, 60 and 85 ºC), during different exposure times and with different initial As(V) concentrations, $[As]_0$. The supernatant water was analyzed and the precipitates characterized by high-energy X-ray diffraction (HEXD) with synchrotron radiation. During the synthesis process, schwertmannite was the only phase of the initial precipitates, except for those cases with $[As]_0 > 0.5$ mM, where a amorphous Fe- and As-rich phase was formed. As a result, a delay in the schwertmannite precipitation and its transformation was observed in those experiments with a higher As added concentration. During the experiment a release of As was detected at long-term aging. Also, the introduction of As to the structure can generate local defects that have been elucidated with Pair distribution function (PDF) analysis. It mainly affects to Fe-octahedra, disappearing in part from the structure.

This thesis aims to clear up the behavior of trace elements during the diagenesis of AMD precipitates. These studies should be taken into consideration for the design of new AMD water treatment plants, as what was meant to be a solution for the pollution in water courses might be a potential source of problems in the future.

RESUMEN

Tanto las actividades mineras como industriales son los principales focos de contaminación del medio natural. Sin embargo, muchos de estos procesos tienen un origen natural, como es el caso del conocido como drenaje ácido de roca (ARD, *acid rock drainage*). El ARD es resultado directo del afloramiento de sulfuros metálicos a condiciones ambientales. Cuando interactúan con agua meteórica, la disolución oxidativa de los sulfuros libera protones, metales y soluciones a la solución y provoca la acidificación del medio. El drenaje ácido de mina (AMD, *acid mine drainage*) es un proceso de lixiviación derivado de la actividad minera, acrecentando el efecto producido por el ARD. El principal sulfuro metálico asociado a estos medios AMD es la pirita [FeS_2], pero comúnmente está asociado con otros sulfuros como la arsenopirita [$FeAsS$], calcopirita [$CuFeS_2$] o galena [PbS], o esfalerita [ZnS]. Muchos de estos metal(oid)es (a partir de ahora *metales*) contenidos en los sulfuros son considerados toxinas para el medio natural, por lo que su control es importante. Una de las principales provincias metalogénicas de sulfuros masivos en el mundo se encuentra en el SW de la Península Ibérica, la Faja Pirítica Ibérica (IPB, *Iberian Pyrite Belt*), donde la actividad minera se remonta a tiempos prerromanos.

No obstante, la gran descarga de contaminantes al agua hace que se formen una serie de fases minerales poco cristalinas que son capaces de retener metales traza. Schwertmannita [$Fe_8O_8(OH)_{(8-2x)}(SO_4)_x \cdot nH_2O; 1 \leq x \leq 1.75$] es un oxi-hidroxisulfato de Fe nanocristalino que precipita de espontáneamente formando terrazas sedimentarias en el lecho de corrientes de agua afectadas por AMD tamponando el pH entre 2 y 4. Su pobre cristalinidad le confiere 2 características (1) que capte una gran cantidad de metales traza en solución, y (2) al ser una fase metaestable, se transforma fácil y rápidamente en goethita [$FeOOH$] y jarosita [$KFe_3(SO_4)_2(OH)_6$] y, a largo plazo, a hematite [Fe_2O_3]. El comportamiento de los metales traza previamente retenidos por la schwertmannita durante su transformación es un foco de discusión en la comunidad científica, y es ahí donde se enmarca la presente tesis.

Varias muestras de diferentes estadios de maduración fueron recogidas y caracterizadas química y mineralógicamente por espectroscopía micro-Raman, por microscopía óptica reflejada, difracción de rayos-X (XRD, *x-ray diffraction*), microscopia electrónica de barrido (SEM, *scanning electron microscopy*), microsonda electrónica (EPMA, *electronic probe micro-analyzer*) y digestión ácida total. En ambientes de AMD, se observaorn que en las terrazas modernas la fase principal era la schwertmannita, la cual se forma en el lecho del río, sorbiendo el As en solución. En un perfil de terraza se observa que a medida que profundizamos la goethita y, eventualmente, la jarosita aparecen, siendo finalmente la goethita la fase predomínate en los niveles más profundos. Después de una maduración diagenética, las terrazas fósiles están formadas por goethita muy cristalina y hematite. En este estudio se muestra la μ-Raman como una herramienta útil para la caracterización mineralógica de fases de Fe(III), tanto óxidos, como hidróxidos y oxi-hidroxisulfatos. Sin embargo, no se puedo detectar la incorporación del As en la estructura, debido a la pobre concentración de As en los precipitados naturales.

En el segundo estudio se utilizaron sendas muestras representativas de los estadios extremos de la diagénesis; una muestra de una terraza actual y otra antigua. Las muestras fueron caracterizadas mineralógicamente por μ-Raman. Además, se hicieron digestiones ácidas de las muestras, análisis de microsonda y, principalmente, mapas de μ-fluorescencia de rayos-X con radiación sincrotrón (μ-XRF) focalizado en los rangos de los metales traza más abundantes; As, Cu y Zn. El gran número de datos obtenidos se analizó utilizando técnicas estadísticas como el análisis de componentes principales (PCA, *principal components analysis*). Con este tratamiento de datos se detectó una pérdida progresiva de la afinidad de los metales traza por el elemento principal, el Fe, a medida que las fases eran más cristalinas (Fe R^2 schwertmannita > goethita > goethita cristalina ≫ hematite).

Por último, se realizaron experimentos con muestras sintéticas para poder simular los procesos diagenéticos de transformación de la schwertmannita. Para ello, se ha precipitado schwertmannita a diferentes temperaturas (40, 60 y 85°C), durante diferentes tiempos de exposición y con diferentes concentraciones de As(V), $[As]_0$. El agua sobrenadante fue analizada y los precipitados caracterizados por difracción de rayos-x de alta energía (HEXD, *high energy x-ray diffraction*). Durante el proceso de síntesis, schwertmannita ha sido la única fase de formación, salvo en casos en los que $[As]_0 < 0.5$ mM, en los que se ha formado una fase pseudoamorfa rica en Fe y As. Como resultado, se observó un retardo en la precipitación de la schwertmannita y de su transformación en los experimentos con mayor concentración de As añadida. Durante los experimentos se detectó una liberación del As en envejecimiento a largo plazo. Además, la introducción del As en la estructura parece generar defectos locales, los cuales han sido analizados con función de distribución de pares (PDF, *pair distribution function*). Principalmente afecta algunos octaedros de Fe, desapareciendo en parte de la estructura.

En esta tesis se ha tratado de esclarecer el comportamiento de los metales traza durante la diagénesis de los precipitados de AMD. Estos estudios deben de ser tenidos en cuenta en el diseño de nuevas plantas de tratamiento de aguas de AMD, ya que lo que en un principio parece ser una solución a la contaminación de los cursos de agua puede ser un potencial foco de problemas en el futuro.

THESIS OUTLINE

The present Doctoral Thesis has been divided into 5 chapters; an initial introduction, three main chapters based on three original scientific works and a final chapter for concluding remarks. The three main chapters have been distributed in order to provide different insights, which at some points might be redundant since some samples have been used several times as well as some techniques have been repeatedly employed in different samples. The information contained can be summarized as follows:

Chapter I: Introduction

Issues, motivations, challenges and techniques used to perform the study are described in this chapter. This section includes a *state of art* about generation and treatment of the acid mine drainage associated with sulfide-rich mining environments, as well as the processes of precipitation and transformation of secondary Fe(III) phases, natural attenuation of pollution, the behavior of the trace elements, a geological description of the field area - the Iberian Pyrite Belt, a brief explanation of the methodology conducted, and a final section with the aims and objectives of the thesis.

Chapter II: Raman identification of Fe precipitates and evaluation of As fate during phase transformation in Tinto and Odiel River Basins (Chemical Geology; Parviainen et al., 2015)

The Fe-precipitates formed in the acid mine drainages are accumulated on the riverbeds of the affected watercourses. Schwertmannite, as a metastable phase, transforms in short-term periods to goethite, but both phases can coexist, so the characterization of both might be difficult. Moreover, in a longer period (centuries) goethite is transformed to hematite, coexisting with goethite. Raman μ-spectrometry has been proved to be a good technique to perform point-analyses of this kind of iron precipitates. In this chapter, natural terrace samples have been characterized chemically and mineralogically. This will help to perform a better detection of the minerals in heterogeneous Fe-precipitates samples such as these. A better characterization of the minerals and its composition, will help to determine the relation with the phases.

Chapter III: Trace element-mineral associations in modern and ancient iron terraces in acid drainage environments (Catena; Cruz-Hernández et al., 2016)

One of the main *hot spots* in environmental research is the behavior of the trace elements originally removed by metastable phases over long-term periods. In this part of the thesis, two natural terrace samples have been analyzed by micro-compositional mapping with synchrotron-based X-ray fluorescence to detect the relation between the trace elements and the minerals forming the terraces. It has been possible to determine the affinity of the trace elements to each forming phase with a thorough statistical treatment of the data. The increase

of crystallinity of the precipitates is linked with the loss of affinity of the trace elements with the main component, Fe, which indicates the possible remobilization of the toxins.

Chapter IV: The role of As(V) during the early diagenesis of Fe-precipitates

Since it is not possible to reproduce the mineralogical transformation of Fe(III) phases throughout an entire diagenetic process, this has been simulated in the laboratory by accelerating the kinetics by heating synthetic solutions. In this study, schwertmannite has been synthesized with As(V) in solution, in order to examine the role of As in the formation and transformation of this phase. As a result, As seems to stabilize the Fe-phases, delaying their precipitation and transformation into more crystalline phases. This recrystalization of goethite entails the release of part of the As retained, meaning that the precipitates are temporal sinks of As. In addition, some local defects have been pinpointed, as provoked by the introduction of As into the structure of the schwertmannite.

Chapter V: General Conclusions

The information obtained by the successive studies performed has been summarized in this chapter, including some future recommendations.

TABLE OF CONTENTS

FIGURE CAPTIONS

TABLE CAPTIONS

Table 3.2: Electron microprobe analyses (n=100) of goethite (*gt*) and hematite (*hm*) levels in the ancient terrace. Depth intervals match those shown in Figure 5. 76

CHAPTER I

INTRODUCTION

INTRODUCTION

Acid drainage (AD) is one of the biggest environmental problems related to coal and sulfide deposits worldwide. This phenomenon is initiated by the interaction of sulfide minerals, mainly pyrite [FeS_2], with meteoric water under oxidizing conditions (Nordstrom, 1982; Moses et al., 1987). The oxidative dissolution of sulfide minerals can lead to widespread acidification of watercourses. When this process occurs at natural outcroppings of sulfide orebodies it is referred to as acid rock drainage (ARD). Although ARD itself can drastically degrade local watercourses, the exposure of sulfide minerals by mining activities can accelerate and escalate contamination associated with AD. As a result of ore extraction and processing, non-economic sulfides are accumulated in open-air piles as gangue. This activity accelerates oxidative weathering and leads to generation of acid mine drainage (AMD), which is generally produced at a greater rate than ARD (Olías et al., 2004). Intensive mining in many parts of the world has left behind a vast quantity of sulfide mine wastes, which has accelerated sulfide oxidation and, therefore, the contamination of watercourses.

Acidification of watercourses is not the only environmental problem associated with AD. Linked to those sulfides, there are a wide range of heavy metals and other toxic elements, which are released together with Fe and SO_4 during their oxidation. Meanwhile heavy metals are always in solution in watercourses in small concentrations, the increase of these elements in solution becomes a source of toxicity for the autochthonous organisms. Furthermore, high concentration of toxic elements in solution causes the death of some of the species and the accumulation along the food chain, inasmuch as heavy metals are not biodegradable (Woodwell et al., 1971).

1.1 Acid drainage generation

Sulfide tailings and outcrops are the main source of AD. The sulfide exposure to the open-air by mining activities enhances the reactivity of these minerals and hence the generation of AMD. Pyrite is the most common sulfide associated to metallic deposits. The oxidative weathering of sulfide minerals has been studied extensively (e.g. Lowson, 1982; Evangelou, 1995; Evangelou and Zhang, 1995; Nordstrom and Southam, 1997; Nordstrom and Alpers, 1999; Rimstidt and Vaughan, 2003). The weathering process involves a series of chemical, biological, and electrochemical reactions with the consequent dissolution of ferrous cations and oxidation onto ferric. These reactions release SO_4 and associated trace elements, and generate protons that acidify the water (Singer and Stumm, 1970):

$$FeS_{2(s)} + \frac{7}{2}O_2 + H_2O \rightarrow Fe^{2+} + 2SO_4 + 2H^+ \qquad \text{Eq. (1.1)}$$

$$Fe^{2+} + \frac{1}{4}O_2 + H^+ \leftrightarrow Fe^{3+} + \frac{1}{2}H_2O \qquad \text{Eq. (1.2)}$$

$$Fe^{3+} + 3H_2O \leftrightarrow Fe(OH)_{3(s)} + 3H^+ \qquad \text{Eq. (1.3)}$$

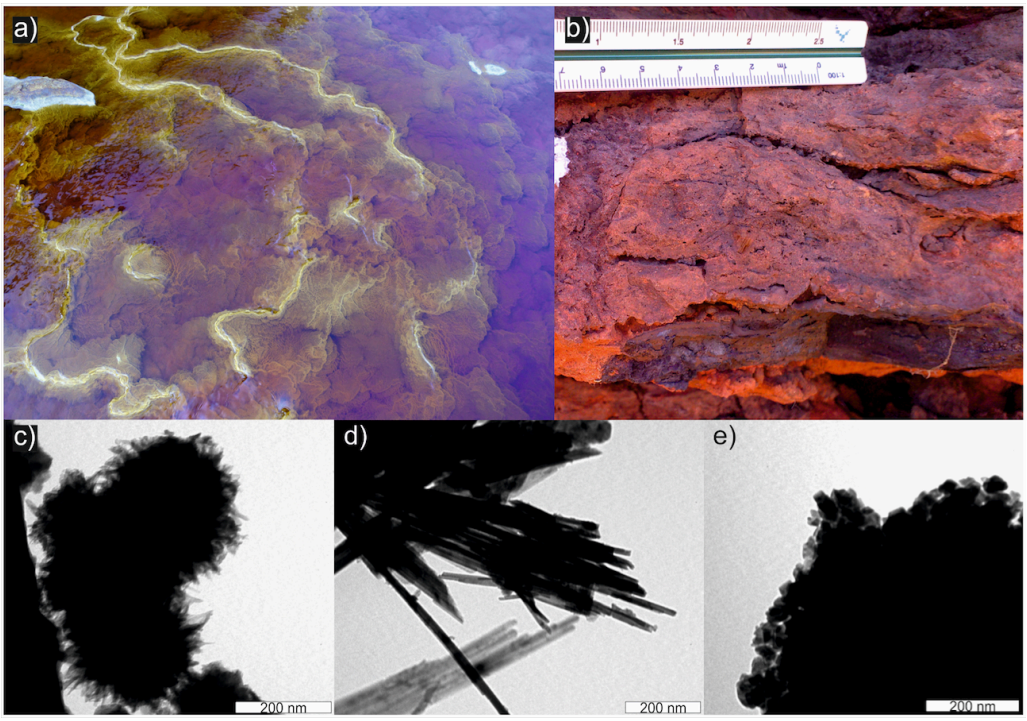

***Fig. 1.1**: Filed pictures of a) an AMD affected riverbed in Tharsis (Huelva, SW Spain), and b) an ancient Fe-terrace in Riotinto (Huelva, SW Spain). Transmission Electronic Microscope (TEM) images of synthetic c) schwertmannite, d) goethite, and e) hematite.*

Pyrite is firstly dissolved in presence of O_2 in solution (Eq. 1.1), releasing protons, Fe^{2+} and SO_4^{-2} to the water. Thus, the acidification of the water leads to a rise in the concentration of dissolved solids. When there is enough aqueous O_2 in solution, Fe^{2+} is oxidized to Fe^{3+} (Eq. 1.2) giving the water a reddish color. The permanence of Fe^{3+} in solution is pH-dependent; at pH level higher than 3.5, Fe^{3+} precipitates often as a Fe-oxy-hydroxide called ferrihydrite [$Fe_2^{3+}O_3 \cdot 0.5H_2O$]. During its precipitation, more protons are released, acidifying the water (Eq. 1.3). However, in acid-sulfate waters including AMD, Fe-oxy-hydroxysulfates such as schwertmannite [$Fe_8O_8(OH)_{(8-2x)}(SO_4)_x \cdot nH_2O;\ 1 \leq x \leq 1.75$] or jarosite [$KFe_3(SO_4)_2(OH)_6$] may form instead of ferrihydrite depending on pH conditions (Bigham et al., 1996).

Thanks to a relatively high specific surface area and the big tunnels forming its structure, schwertmannite is an effective scavenger of potential pollutants including As, Zn, Pb, Mn, and Se (Webster et al., 1998; Fukushi et al., 2003, 2004; Fernandez-Martinez et al., 2010). These toxic elements are commonly associated to metallic sulfides. Similar to pyrite, these sulfides are oxidized and dissolved, releasing these metals to the water, becoming a source of pollutants. Following pyrite, most common sulfides are arsenopyrite [$FeAsS$, (Eq. 1.4)], chalcopyrite [$CuFeS_2$, (Eq. 1.5)], sphalerite [ZnS, (Eq. 1.6)], and galena [PbS, (Eq. 1.7)]:

$$4FeAsS_{(s)} + 11O_2 + 6H_2O \leftrightarrow 4Fe^{2+} + 4H_3AsO_{3(aq)} + SO_4 \quad \text{Eq. (1.4)}$$

$$CuFeS_{2(s)} + 4O_2 \rightarrow Cu^{2+} + Fe^{2+} + 2SO_4 \quad \text{Eq. (1.5)}$$

$$ZnS_{(s)} + 2O_2 \rightarrow Zn^{2+} + SO_4 \quad \text{Eq. (1.6)}$$

$$PbS_{(s)} + 2O_2 \rightarrow Pb^{2+} + SO_4 \quad \text{Eq. (1.7)}$$

Nonetheless, the natural oxidation rates of these minerals in aseptic conditions do not correspond with what is observed in the field. Despite the water acidification and the large amount of metals in solution derived from the dissolution of the sulfides, there are some, so-called “extremophiles”, organisms capable of living under these conditions. Some bacterium, such as *Thiobacillus ferroxidans or Leptospirillum ferroxidans*, have adapted to AD environments. Moreover, some of them oxidize sulfides (Boon and Heijnen, 1998), while others use ferrous ion oxidizing it to Fe^{3+} (Leduc et al., 2002). This bacteriological activity can accelerate the oxidation process from 10^4 to 10^6 times (Singer and Stumm, 1970).

1.2 Schwertmannite; precipitation and transformation

Schwertmannite is a poorly crystalline oxyhydroxysulfate that often precipitates and covers the riverbed of the watercourses affected by AMD (Fig. 1.1a). This oxyhydroxysulfate is accumulated forming bands of loose-dust Fe precipitates ending as a stromatolite-like structure. These stromatolites display a morphological pattern similar to calcareous travertines, generating terraces, where new precipitates overlap older ones. Schwertmannite forms aggregates of nanoparticles (up to 2 μm) "hedge-hog" like consisting of radially oriented acicular nanocrystals (Fig. 1.1c). Due to its poor crystallinity, schwertmannite is not an stable phase and it evolves into goethite (Eq. 1.8) and, eventually, jarosite in some weeks (Fig. 1.1d) (Acero et al., 2006; Bigham et al., 1996; Gagliano et al., 2004):

$$Fe_8O_8(OH)_{5.5}(SO_4)_{1.25(s)} + 2.5H_2O \rightarrow$$
$$8FeOOH_{(s)} + 2.5H^+ + 1.25SO_4 \qquad \text{Eq. (1.8)}$$

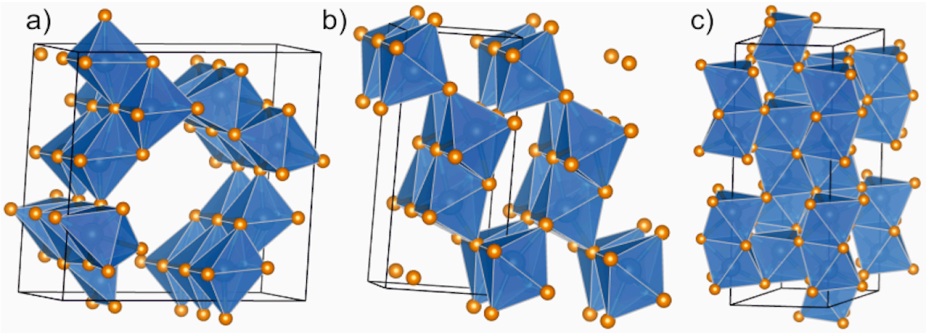

***Fig. 1.2**: Structures of a) schwertmannite (Fernandez-Martinez et al., 2010), b) goethite (Alvarez et al., 2008) and c) hematite (Gualtieri and Venturelli, 1999). In the figures, Fe-octahedra are represented in blue, and oxygen with orange spheres.*

Schwertmannite is formed by Fe-octahedra settled in a network of square tunnels (Fig. 1.2a; Fernandez-Martinez et al., 2010). The sulfate tetrahedral position remains unclear; sulfate seems to occur in both inner and outer-sphere positions depending on pH and hydration conditions (Wang et al., 2015). During the transformation from schwertmannite into goethite, SO_4 is released along with two Fe-octahedra in the unit cell (Regenspurg and Peiffer, 2005; Paikaray and Peiffer, 2012), converting the square tunnels in schwertmannite to rectangular tunnels in goethite (Fernandez-Martinez et al., 2010) (Fig. 1.2a, b). In addition, protons are released causing acidification (Eq. 1.8). Some researches, such as Schroth and Parnell (2005), suggested a dissolution of schwertmannite and a precipitation of goethite

instead of SO_4^{2-} loss during recrystallization. The formation, transformation and structure of schwertmannite have been dominant research topics lately due to their relevance in the Earth and environmental sciences.

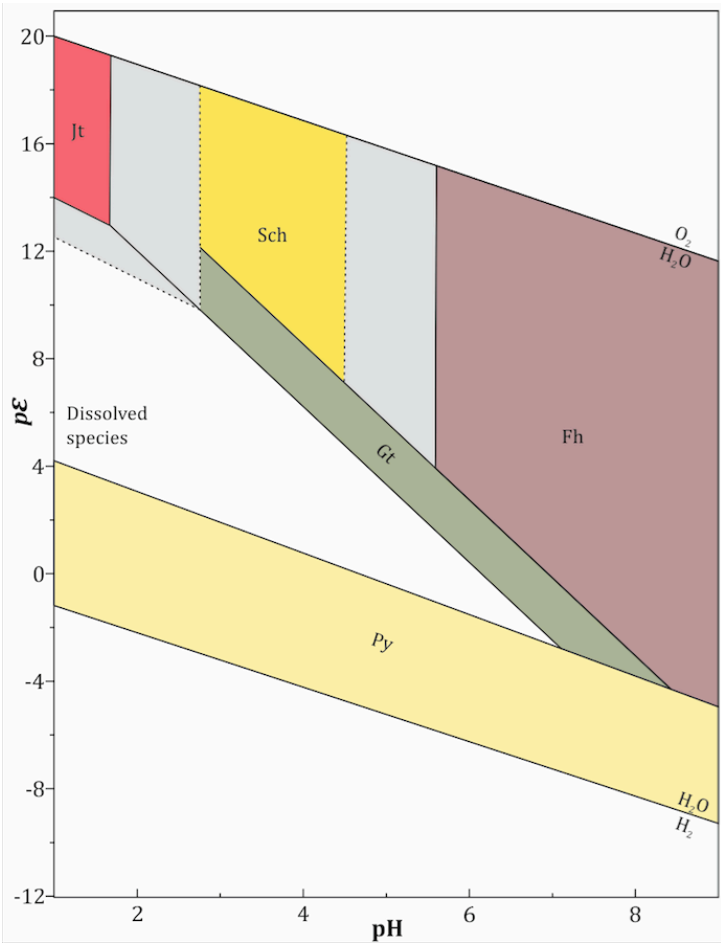

***Fig. 1.3**: pε − pH diagram of Fe-S-K-O-H systems at 25°C and 1 bar. $pε = Eh(meV)/59.2$. Solid phase fields: Jt = K-jarosite, Sch = schwertmannite, Gt = goethite, Fh = ferrihydrite, Py = pyrite. Grey fields correspond to expansions stability areas of jarosite, schwertmannite and ferrihydrite (modified from Bigham et al., 1996).*

Some ancient stromatolite-like structures of goethite-hematite bands are often found in the vicinity of AD systems (Fig. 1.1b). Although direct transformation of schwertmannite into hematite [Fe_2O_3] (Figs. 1.1e and 1.2c) has been observed under hydrothermal conditions at 200°C (Barham, 1997), in these bands of ancient deposits hematite replacement of goethite has been reported by means of textural observations (Bowell, 1994; Cudeenec and Lecref, 2005; Mamindy-Pajany et al., 2011; Pérez-López et al., 2011). Goethite might transformation

into hematite by means of dehydration, which has previously been hypothesized (Eq. 1.9; Langmuir, 1971; Davidson et al., 2008);

$$2FeOOH_{(s)} \rightarrow Fe_2O_{3(s)} + H_2O \qquad \text{Eq. (1.9)}$$

Gualtieri and Venturelli (1999) defined “protohematite” as an intermediate phase after goethite decomposition that would transform progressively to hematite.

1.3 Natural attenuation processes

As previously mentioned, AMD has a particularly harmful impact on natural environments due to the release of toxic pollutants to watercourses (Eq. 1.1, 1.4, 1.5, 1.6, 1.7) turning these settings virtually uninhabitable (Alpers et al., 1994; Bowell and Bruce, 1995; Cánovas et al., 2007). Secondary Fe precipitates that form in these AMD-affected watercourses are often effective scavengers of toxic elements (Chapman et al., 1983; Berger et al., 2000; Fukushi et al., 2003a). Schwertmannite precipitation spontaneously occurs by oversaturation once the ideal conditions of pH and Eh have been reached ($2.5 \leq pH \geq 4.5$ and $500\ eV \leq Eh$; Fig. 1.3). Poor crystallinity and large surface area result in schwertmannite having a strong capacity to remove trace elements from solution by sorption or co-precipitation (Acero et al., 2006; Courtin-Nomade et al., 2003; Schwertmann et al., 1995).

In AMD environments, affected watercourses are usually mixed with pristine waters along its path, increasing the pH favoring the formation of Fe oxy-hydroxides (eq. 1.3). The pH increases and decreases due to the buffer provoked by the release of protons (eq. 1.3) till the total precipitation of Fe (III) from solution (eq. 1.8). However, in AMD media derived from sulfide orebodies SO_4 concentration is also high, but the limiting factor is Fe (III). Once the Fe (III) has been depleted by precipitation SO_4 interacts with other major cations, such as Al. Basaluminite $[Al_4(SO_4)(OH)_{10} \cdot 4{\sim}5H_2O]$ is a poorly crystalline Al-hydroxysulphate (Hollingworth and Bannister, 1950; Nordstrom, 1982b). It also has a good capacity for retaining trace metals (Nordstrom and Alpers, 1999b; Bigham and Nordstrom, 2000), although in continuous treatment assays the basaluminite capacity is masked by schwertmannite during the precipitation sequence (Carrero et al., 2015). However, the concentration of Al is much lower than those of Fe, and the long-term record of Al-phases in natural AD systems is practically nil.

In any case, there is a certain lack of knowledge with the final fate of the retained traces during the recrystallization of the precursor phases to more crystalline ones. It seems logical that with a higher crystallinity of the precipitates the void content for metals should decrease, but some researches suggest an adsorption on the surface of these transformed phases (Gimenez et al., 2007; Mamindy-Pajany et al., 2011).

1.4 AMD treatment systems

AMD treatment systems are classified into active and passive technologies, depending on the energy source required (Younger, 2000; Jarvis and Younger, 2001). Active treatment plants need to be connected to energy power and the addition of chemical reagents, while passive systems use natural energy sources, such as water flow and gravity, as well as biochemical reactions. As active plants require power generation installations, unprofitable for orphan mines, passive treatments are often regarded as the best option. The lack of earlier environmental legislation has expedited the massive forsaking of old mining facilities, including tailings and pits. These abandoned mines are the primary contamination source in many mining districts. The fact that legal responsibilities cannot be claimed since those mining companies do not exist nowadays makes passive treatment systems the best remediation method from an economic and environmental perspective.

Traditionally, the passive treatment systems have been based on flowing contaminated water through different tanks with different pH neutralizing agents to immobilize metals as oxyhydroxysulfates and/or with organic matter enhancing sulfate-reducing conditions to immobilize contaminants as sulfides. (Hedin et al., 1994; Jage et al., 2001). Still, studies carried out in AMD environments with very high metals concentrations using different alkaline tanks showed problems of passivation and clogging of the reactive substrate (Röting et al., 2003). Dispersed alkaline substrate (DAS) uses a mixture of fine-grained reagents (e.g., limestone, MgO powder) with coarse wood shavings to reduce the clogging and increase the reactive area, optimizing the reagents (Rötting et al., 2008). Lately, DAS systems have been enhanced increasing the oxidation of the water with a system of small waterfalls and pools as pretreatment (Macías et al., 2012a, b).

1.5 Trace elements mobility *state of art*

Research into trace element mobility during the transformation of host phases – particularly studies focused on nanoparticles and mine wastes – has recently received a great attention. As stated before, schwertmannite, which is a key phase formed in SO_4-Fe-rich acid drainage, is an effective scavenger of trace elements because of its poor crystallinity and relatively high surface area (e.g.: Banfield et al., 2000; Bigham et al., 1996; Paikaray et al., 2012, 2011; Stipp et al., 2002; Waychunas et al., 2005, 1992; Zhu et al., 2012). However, there remains controversy regarding the behavior of trace elements during the schwertmannite transformation into more stable phases.

During the schwertmannite recrystallization to goethite, the inter-atomic space decreases due to a reduction of Fe-Fe distances (Combes et al., 1990; Manceau and Drits, 1993); hence, trace elements should be released from the structural positions, being re-mobilized to the water media. Nevertheless, several studies support the idea that the retention capacity of goethite is in the same order of magnitude as its precursor schwertmannite (Acero et al., 2006). Moreover, the debate is also focused on the transformation to hematite. Several studies claim that hematite has lower retention capacity than goethite (Bowell, 1994; Manceau, 1995; Pérez-López et al., 2011) while, on the contrary, other studies affirm that goethite retains less traces into its structure and surface (Gimenez et al., 2007; Mamindy-Pajany et al., 2011). Other works suggest the existence of an intergrowth of several phases during the transformation; e.g. Bolanz et al. (2013) reject the As incorporation into hematite structure and they state that an epitaxial intergrowth of hematite with angelite [$Fe_4(AsO_4)O_3$] is plausible. Thus, As would be mainly retained by angelite and only a small part would stay on the surface of hematite.

Knowing the behavior of trace elements during the phase transformation is crucial to understand the natural attenuation of contamination in AD-affected waters. As a sink of some toxic elements, the long-term stability of the Fe-oxyhydroxydes should be also considered. In fact, some studies have calculated the transformation rates for schwertmannite and ferrihydrite (Burton et al., 2008; Ford, 2002; Jönsson et al., 2005; Paikaray and Peiffer, 2012; Regenspurg and Peiffer, 2005). Specifically, Burton et al. (2008) asserts that the presence of oxyanions such as SO_4 stabilize the structure of the poorly crystalline Fe(III) oxy-hydroxides retarding their transformation comparing with those calculated for ferrihydrite. Davidson et al. (2008) and Ford (2002) went beyond and tried to evaluate the transformation of goethite

to hematite without detecting a delay on the maturation. Thus, they hypothesized that, since oxyanions are not incorporated as a part of the mineral structure in inner-sphere positions, the presence of these elements do not affect the stability of more crystalline phases.

During the acid drainage treatment, the effective management of the resulting solid wastes has received limited attention. In some cases, it is planned to deposit the solid wastes in landfills, being burned previously in order to remove the wood shavings and reduce their volume. Most wastes are Fe and Al oxy-hydroxydes, so the remobilization of the pollutants could happen, inasmuch as burning them enhances the potential recrystallization of the precipitates.

1.6 The Iberian Pyrite Belt

The Iberian Pyrite Belt (IPB) is one of the most prolific metallogenic provinces of massive metallic sulfides orebodies. It hosts some of the most extensive massive sulfide bodies worldwide. Reserves have been estimated in excess of 1700 Mt, which represents 22% of the world class volcanic massive sulfides deposits (Sáez et al., 1999; Tornos, 2006). It is located in the SW of the Iberian Peninsula (Fig. 1.4), encompassing approximately 230 km E-W and 40 km N-S, from Seville, in Spain, to southern part of Lisbon (Portugal). Due to the great concentration of metallic sulfides, the IPB has been intensively exploited by mining activity during the last 4,500 years (Nocete et al., 2014). So far, the IPB hosts more than 100 active and inactive mines, being one of the most active massive sulfide mining areas worldwide.

Stratigraphically, IPB is subdivided in 3 main lithostratigraphic units. From the footwall to the hanging wall there are: the Devonian Phyllite-Quartzite group (PQ Group); the early Carboniferous Volcano-Sedimentary Complex (VSC); and the late Carboniferous post-volcanic succession phyllite-grawackes (Culm group) (Schermerhorn, 1971). Massive sulfide orebodies are associated to VSC, which consists of an intercalation of volcanic rocks with detrital sedimentary sequences of shales and sandstones derived of volcanic episodes ranging in age from late Famennian to early Visean (Barrie et al., 2002; Nesbitt et al., 1999; Nieto et al., 2000). The massive sulfides occur as lenses associated mostly with felsic-volcanoclastic and/or black shale sequences (Sáez et al., 1996). The massive sulfide deposits in the IPB are composed mostly of pyrite, with subordinated arsenopyrite, sphalerite, galena, chalcopyrite, tetrahedrite-tennantite $[(Cu, Fe)_{12}Sb_{14}S_{13} - Cu_{12}As_4S_{13}]$, pyrrhotite $[Fe_{1-x}S; x = 0 - 0.2]$ and many other minor phases such as Bi- and Pb-sulfosalts, cassiterite $[SnO_2]$, magnetite $[Fe^{2+}Fe_2^{3+}O_4]$, stannite $[Cu_2FeSnS_4]$, electrum [Au, Ag], and cobaltite [CoAsS] (García de Miguel, 1990; Marcoux et al., 1996).

The extensional tectonic period that took place during late Devonian-early Carboniferous collapsing and fracturing the basin, caused the later volcanism episodes, favoring the deposition of sulfides (Moreno et al., 1996). The deposition of sulfides was interbedded with black-shales and volcanoclastic rocks from two felsic volcanic episodes (Barriga, 1990). The gradual ascension of magma created a the necessary hydrothermal system for the transportation and deposition of metals intercropped with the shales (Sáez et al., 1999). Culm group covers the VSC. It is a thick turbiditic sequence derived from the rising of the basin as a response to the tectonic pulses (Moreno, 1993).

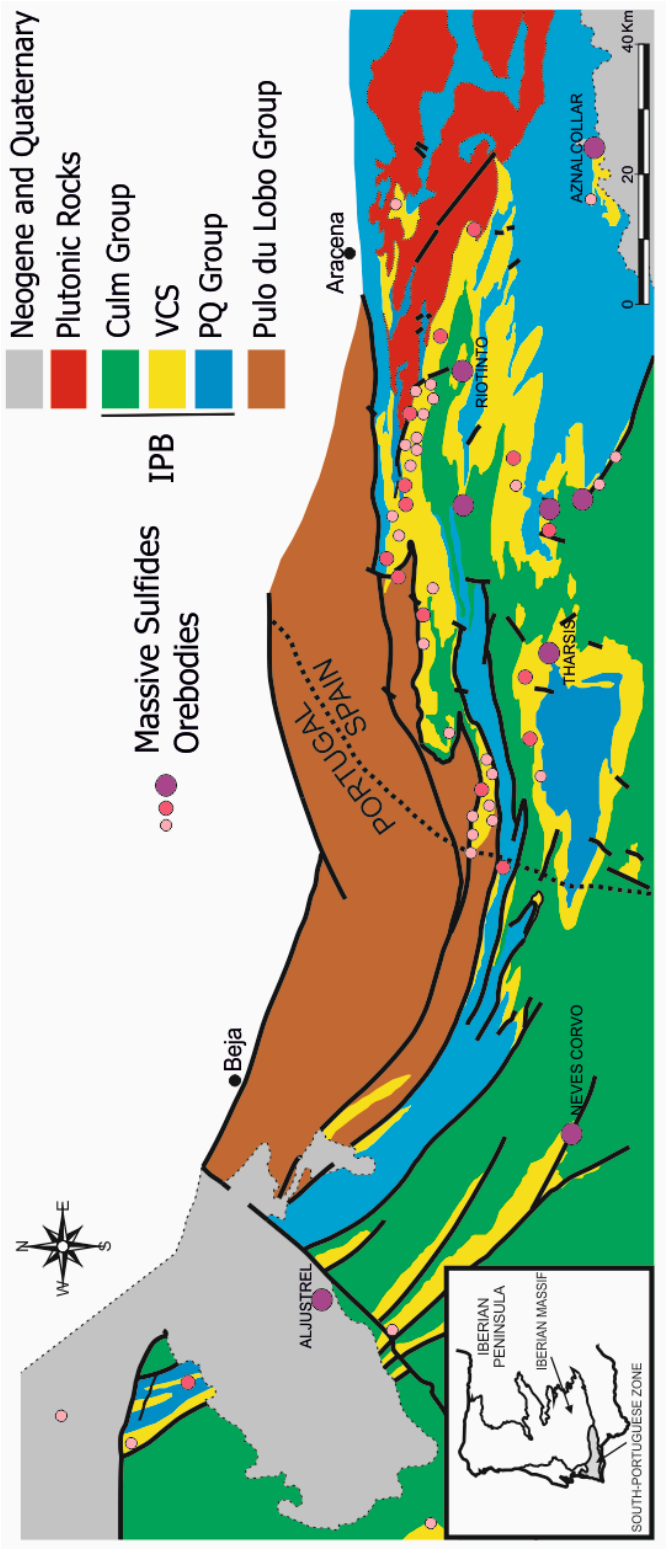

***Fig.1.4**: Iberian Pyrite Belt area geological map and location of the main massive sulfidic orebodies.*

The IPB was deformed during the Variscan orogeny in three different stages. The first stage, middle Westaphalian in age (Silva et al., 1990), caused an intense folding of the basin, with the consequent new compressive episode that formed a N-S directed foliation. Then, during the late-Variscan fracturing phase, the E-W fault system was formed (Fig. 1.4) finally followed by NW-SE extensional episode. Once the Variscan deformation ended, the marine transgression on the Tertiary covered the IPB with sediments of the Guadalquivir and Sado basins (Strauss and Madel, 1974). It was buried by a Neogene infill of carbonate and detrital sequences, disconformably with the Paleozoic basement.

The natural exposure of sulfide orebodies involves the development of iron oxide caps on top known as gossan. A gossan is a poplar mining term coined to refer to a deposit mainly formed by iron oxides and hydroxides derived from the weathering of sulfide orebodies above the phreatic level (García Palomero et al., 1986; Scott et al., 2001; Velasco et al., 2013). Gossans are differentiated by their formation, since their origin could be either sedimentary (erosive action produced by watercourses) or hydrothermal, as an alteration of porphyries (massive gossan or stockwork).

In the IPB case, the weathering process began in the upper Oligocene-lower Miocene (Essalhi et al., 2011; Velasco et al., 2013). The exhumation and surface exposition of some massive sulfide deposits caused the generation of gossan caps. Some examples of gossans in the IPB are seen at Tharsis, Riotinto, San Miguel and São Domingos (Arribas, 1998; García Palomero et al., 1986).

Beside goethite and hematite, the IPB gossan are composed by quarts and newly-formed oxyhydroxides, oxides, sulfates, oxy-sulfates, sulfo-arsenates, arsenates, halides, native metals and phyllosilicates after leaching its protores, under acidic and oxidizing conditions (Velasco et al., 2013; Yesares et al., 2017). In addition, gossans in the Iberian Pyrite Belt have been target of Au and Ag exploration and mining since 3000 BC (Nocete et al., 2014) and most supergene Au deposits in the belt, including Riotinto, La Lapilla, and Filo Sur-Tharsis, were mined for precious metals during the past century (Arribas, 1998; García Palomero et al., 1986; Roca et al., 1999; Sánchez et al., 1996; Viñals et al., 1995; Williams, 1950).

The erosion and remobilization of these gossan caps in the IPB, led to the formation of alluvial deposit of "transported gossans", ironstone sedimentary breccias, or iron-rich hardpans. The displacements use to be around a few dozen meters, and can extend 1 km (e.g. *Alto de la Mesa,* Riotinto) (Velasco et al., 2013; Williams, 1950).

Moreover, Essalhi et al. (2011) found structural similarities between transported gossans and modern iron terraces in AMD affected areas of the IPB. Nieto et al. (2003) has hypothesized that these transported gossans are actually ancient iron oxy-hydroxysulfate terraces which have been transformed over the last 6 million years from the Miocene to Pliocene. The morphology of these gossans is described as a fluvial point-bar with alternation of coarse and fine sediments with a preferential pebble orientation (Essalhi et al., 2011).

Thus, terraces were formed from the oxidation and erosion of the sulfide orebodies, which are the host rocks, and the subsequent precipitation and transformation of the precipitates (explained in sections 1.1 and 1.2 of this introduction). Their mineralogical composition depends on the maturity of the precipitates, being the oldest the richest in in hematite, and the newest richer in sulfates and sulfides.

1.7 Methodology

Conventional methodologies are not amenable to the study of poorly crystalline phases including schwertmannite. The nano-order that forms this and other phases such as ferrihydrite is not perceptible to conventional techniques such as X-ray diffraction (XRD). However, synchrotron-based techniques have successfully been used to examine chemical and structural aspects of poorly crystalline and nano-crystalline materials (Gilbert et al., 2004; Maillot et al., 2013; Waychunas et al., 1995).

An additional issue related to the association of these phases in field samples as natural terraces is the heterogeneous distribution at nano and micrometric scale, which limits the use of bulk analysis methods. In terms of gradual transformation, a point technique is required in order to identify the phase transition. Point techniques, such as electronic microscopy, might help to determine the composition of the samples with a considerable detail. Synchrotron techniques are suitable for examining these changes; however, access to general users requires a process of submission, review and acceptation of proposals of interest. Instead, Raman μ-spectroscopy can be also used to identify these phases, since each phase has characteristic band spectra. Commonly, Raman microscopes are coupled with optical microscopy and can be used to identify areas for more detailed synchrotron analyses. Following, it is briefly explained the theoretical foundation of these techniques, which have been used during this research:

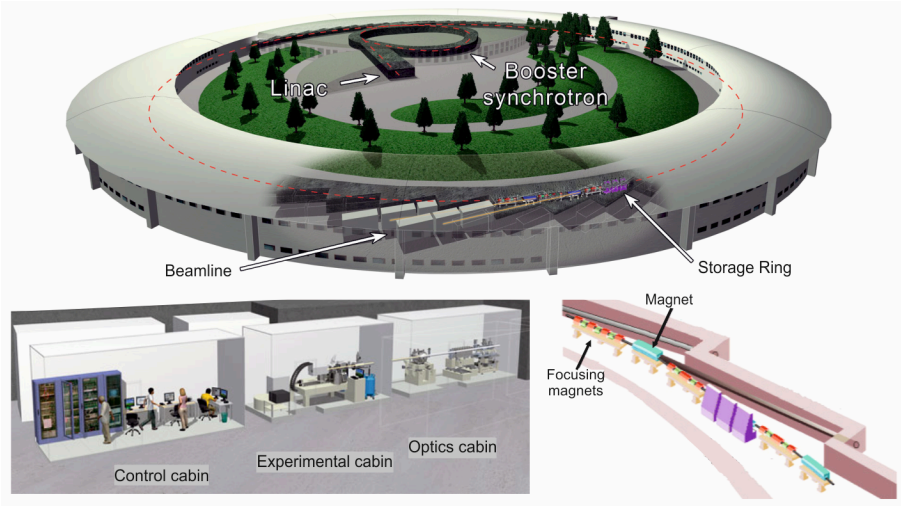

***Fig. 1.5**: Synchrotron facility schema. A general view of a synchrotron building is shown on the top , and in the bottom part, detailed figures of a beamline and the storage ring. Modified from European Synchrotron Radiation Facility (ESRF) website (www.esrf.eu).*

1.7.1 Synchrotron radiation

A Synchrotron is basically a source of photons with a wide distribution of wavelength radiations. The electrons are pre-accelerated at the booster beginning at the gun (Linac, a linear accelerator). Photons are produced by accelerating electrons around a storage ring; electrons get charged while moving, emitting energy at different wavelengths depending on their velocity. Synchrotron accelerates the electrons by magnetic fields generated by magnets positioned concentrically. X-rays are emitted through beamline channels (Fig. 1.5), which are tangentially disposed to the circular pathway (storage beam) of the electrons and come into the *beamlines* as a beam of X-rays. This beam is focused by a series of mirrors and crystals directed through the sample to the detector(s) (ESRF, n.d.).

1.7.1.1 Hard x-ray microprobe for focused μ x-ray fluorescence (μ-XRF)

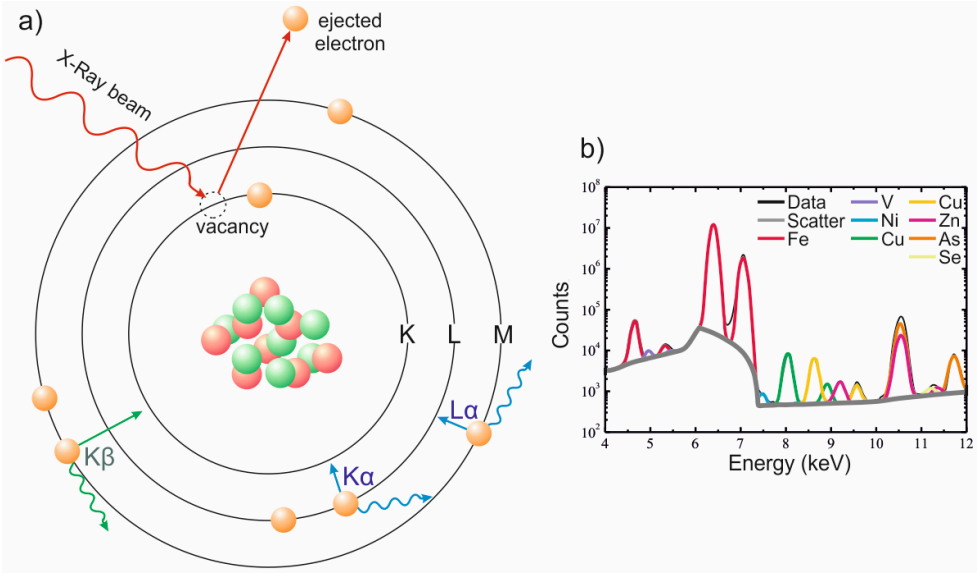

***Fig. 1.6**: a) Fluorescence effect schema. Orange spheres represent the electrons, and red and green are protons and neutrons. Radiations are represented with wavelines, b) μ − XRF spectrum (4-12 keV).*

Fluorescence is a non-destructive technique, although beam can damage some redox-sensitive elements and metastable phases. The sample in question is exposed to γ and X-ray radiation. The electrons in the lowest orbitals are excited and some are ejected, leaving behind an energetic vacancy (Fig. 1.6a). Electrons from more energetic orbitals will then transfer to lower energetic levels, in order to promote lower levels filling the vacancies left by the ejected electrons. The transition provokes the emission of a fluorescence photon, being characteristic

of each element its spectrum of energy released (Fig. 1.6b). There are infinite variants of transition, yet there are 3 main transitions, corresponding to the lowest levels K L M:

- Transition $L \rightarrow K: K\alpha$
- Transition $M \rightarrow K: K\beta$
- Transition $M \rightarrow L: L\alpha$ $(and\ so\ on)$

The photon emitted by each transition is endowed with a characteristic energy, equivalent to the difference between the energy of both involved orbitals.

Synchrotron radiation incorporates microprobe analysis, ultra-high spatial resolution (spot < 1 μm), on the fly imaging at detection limits of ppb, and a big range of energy (from 2.4 to 28 keV). Multiple elements could be analyzed at the same time. Maps are compound of a continuous scanning approach of pixels containing a complete spectrum of the composition of the analyzed area.

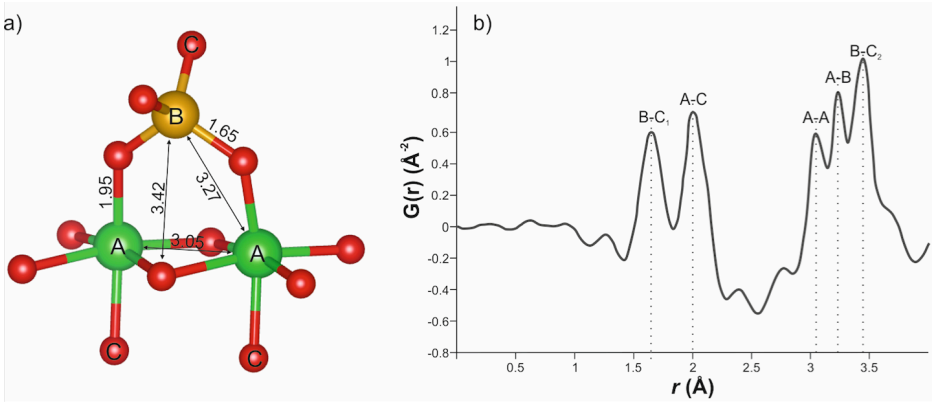

***Fig. 1.7**: a) schema of the structure of a theoretical molecule with atomic distances. b) Fourier transformation of a diffraction of the "a" molecule.*

1.7.1.2 High energy X-ray diffraction and pair distribution function

Pair distribution function (PDF) an analysis obtained from high energy X-ray diffraction (HEXD) patterns. Powder samples are disposed on kapton capillaries and exposed to an X-ray beam with a $\lambda < 0.2$Å $(E > 62\ keV)$. The beam impacts on the sample, diffracts in it and impresses a pattern in the detector. Higher-energy reduces the X-ray wavelength, increasing the diffraction range on the reciprocal space (Q) (Eq. 1.10):

$$Q = 4\pi\ sin(\theta)/\lambda \qquad \text{Eq. (1.10)}$$

Such a small wavelength favors the analysis of poorly structured materials due to it improves the PDF resolution. The interaction of the X-rays with the sample structure is defined as a summation of sins functions of distance in the reciprocal space for each atomic

pair in the structure [$sin\ (Qr_{ij})$]. This function is called "*total scattering function*" [$S(Q)$] or "*observed scattering intensity*" (I_N) and represents the peaks created by all the elements (Debye, 1915);

$$S(Q) = 1 + \frac{1}{N}\sum_{i,j}^{N} b_i b_j \frac{\sin\,(Qr_{ij})}{Qr_{ij}} \qquad \text{Eq. (1.11)}$$

Where the scattering amplitude of this sins function is related to the atomic weight of the elements involucrate in each pare (b_i and b_j). The real-space analysis by Fourier transformation of *S(Q)* results in *g(r)*, so-called PDF:

$$g(r) = 1 + \frac{1}{2\pi^2 r\rho}\int_{Q_{min}}^{Q_{max}} Q\,[S(Q) - 1]\sin(Qr)\,dr \qquad \text{Eq. (1.12)}$$

It is a function of the probability of finding a pair of atoms separated by r distance. As a result, the spectrum obtained will give a pattern with all the pair-distances between the atoms (r) (Fig. 1.7).

1.7.2 Raman μ-spectroscopy

When photons interact with matter, even when a sample is illuminated, the light can be reflected, absorbed or scattered. Raman spectroscopy deals with the scattered light (Raman and Krishnan, 1928). It is based on the inelastic scattering of the monochromatic light in or close to the visible range when electrons are excited to a virtual stage (Fig. 1.8). The light, usually a laser, interacts with phonons stimulating the vibration of the light photons, upward and downward (Gardiner et al., 1990). When photons are excited to a virtual state decaying to a new real vibronic state, they might have a different energy state than initially (as an inelastic scatter). The shifts are reported as bands dimensioned as inverse of wavelength (cm^{-1}) related to the energy.

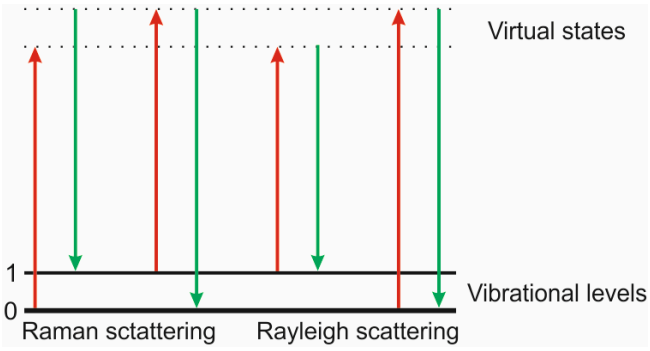

***Fig. 1.8**: Schema of energy level transition of the photons involved in Raman spectroscopy.*

Raman microspectroscopy allows the identification of species in very small volumes, as it has an inverted optical microscope and a bichromatic beam splitter. Thus, the scattered light is collected by the same objective and divided into two ways. In one way, the beam is filtered in order to remove the range wavelengths out of the Raman band is focused on. Each photon is collected and counted by a photodiode. In the other, the light is collected and filtered by a notch filter to remove Rayleigh scattering (elastic scattering). Both signals are combined by the spectrograph and projected on a charge-coupled device (CCD) (Fig. 1.8).

1.8 Aims and objectives

The present Doctoral Thesis has as purpose broadening the knowledge related to the ultimate outcome of the trace elements, initially removed by schwertmannite in AD systems, during its transformation by means of comparing natural samples and laboratory experiments. To this aim, several objectives have been set to be fulfilled throughout this research:

1. To tune up an analytical instrument available in conventional laboratories, i.e. Raman micro-spectroscopy, to identify the mineralogy of the involved phases and their transformation on natural newly-formed and ancient Fe terraces. **Novelty**: note that the mineralogical characterization might be unclear by conventional techniques such as X-Ray diffraction due to the low crystallinity of the involved phases; however, μ-Raman has been successfully applied to several studies of characterization of Fe(III) phases but never in natural AD terraces.

2. To reveal the long-term behavior of the trace elements initially captured by schwertmannite during the mineralogical transformation in natural terraces. **Novelty:** note that most of studies focus on As and results are controversial; however, correlation between chemical analysis obtained by high-spatial resolution synchrotron-XRF mapping and mineralogy will allow shedding light not only on As but also other important trace elements.

3. To evaluate the potential (enhancing or retarding) effect of some trace elements on the schwertmannite precipitation and mineral transformation rates in batch experiments with synthetic AD systems. **Novelty:** Crystallinity increase of nanocrystalline Fe-oxyhidroxides seems to be retarded with the increase of initial As concentration in solution, but this has not proved previously with schwertmannite. Besides, the possible remobilization of the elements with the crystallinity increase of the phases was modeled. To this aim, batch experiments were performed synthetizing samples which were characterized mineralogically and chemically, being exposed at different temperatures (different oxidation acceleration rates), during different periods (maturation lapses), and different $[As]_0$ concentrations.

4. To obtain information on the structural changes inducted by the presence of As (V) during schwertmannite transformation into more crystalline phases. **Novelty**: These poorly crystalline phases contain big gaps into their structure capable of hosting big cations, the structure is affected by the input of "guest" elements. In addition, the maturation of the phases involves chemical and structural changes. The interaction with other elements during the transformation is also noteworthy in order to determine the final fate of the trace elements. The use of PDF techniques has been implemented.

5. To compare the data obtained in laboratory with those recorded in natural systems. **Novelty**: The applicability of this study lies in the management of AMD wastes products. Some of these trace elements are considered harmful for the environment, therefore, treatment systems must be designed considering future aspects such as their final outcome.

REFERENCES

Acero, P., Ayora, C., Torrentó, C., Nieto, J.M., 2006. The behavior of trace elements during schwertmannite precipitation and subsequent transformation into goethite and jarosite. Geochim. Cosmochim. Acta 70, 4130–4139. doi:10.1016/j.gca.2006.06.1367

Alpers, C.N., Blowes, D.W., Nordstrom, D.K., Jambor, J.L., 1994. Secondary Minerals and Acid mine-water Chemistry. Environ. Geochemistry Sulfide Mine Wastes1 247–270.

Alvarez, M., Sileo, E.E., Rueda, E.H., 2008. Structure and reactivity of synthetic Co-substituted goethites. Am. Mineral. 93, 584–590. doi:10.2138/am.2008.2608

Arribas, A., 1998. Los yacimientos de oro asociados con las monteras limoníticas de la FPI. Boletín Geológico y Min. 109, 429–434.

Banfield, J.F., Welch, S.A., Zhang, H., Ebert, T.T., Penn, R.L., 2000. Aggregation-based crystal growth and microstructure development in natural iron oxyhydroxide biomineralization products. Science (80-.). 289, 751–754. doi:10.1126/science.289.5480.751

Barham, R.J., 1997. Schwertmannite: A unique mineral, contains a replaceable ligand, transforms to jarosites, hematites, and/or basic iron sulfate. J. Mater. Res. 12, 2751–2758.

Barrie, T.C., Amelin, Y., Pascual, E., 2002. U-Pb geochronology of VMS mineralization in the Iberian Pyrite belt. Miner. Depos. 37, 684–703. doi:10.1007/s00126-002-0302-7

Barriga, F.J.A.S., 1990. Pre-Mesozoic Geology of Iberia, in: Dallmeyer, R.D., Garcia, E.M. (Eds.), . Springer Berlin Heidelberg, Berlin, Heidelberg, pp. 369–379. doi:10.1007/978-3-642-83980-1_26

Berger, A.C., Bethke, C.M., Krumhansl, J.L., 2000. A process model of natural attenuation in drainage from a historic mining district. Appl. Geochemistry 15, 655–666. doi:10.1016/S0883-2927(99)00074-8

Bigham, J.M., Nordstrom, D.K., 2000. Iron and Aluminum Hydroxysulfates from Acid Sulfate Waters. Rev. Mineral. Geochemistry 40, 351–403. doi:10.2138/rmg.2000.40.7

Bigham, J.M., Schwertmann, U., Traina, S.J., Winland, R.L., Wolf, M., 1996. Schwertmannite and

the chemical modeling of iron in acid sulfate waters. Geochim. Cosmochim. Acta 60, 2111–2121. doi:10.1016/0016-7037(96)00091-9

Bolanz, R.M., Maria Wierzbicka-Wieczorek, M.C.´aplovicova, Peter Uhlík, J., Göttlicher, R., Ralph Steininger, and J.M., 2013. Structural incorporation of arsenic (V) into hematite 47, 9140–9147. doi:dx.doi.org/10.1021/es305182c

Boon, M., Heijnen, J.., 1998. Chemical oxidation kinetics of pyrite in bioleaching processes. Hydrometallurgy 48, 27–41. doi:10.1016/S0304-386X(97)00072-8

Bowell, R.J., 1994. Sorption of arsenic by iron-oxides and oxyhydroxides in soils. Appl. Geochemistry 9, 279–286.

Bowell, R.J., Bruce, I., 1995. Geochemistry of iron ochres and mine waters from Levant Mine, Cornwall. Appl. Geochemistry 10, 237–250. doi:10.1016/0883-2927(94)00036-6

Burton, E.D., Bush, R.T., Sullivan, L.A., Mitchell, D.R.G., 2008. Schwertmannite transformation to goethite via the Fe(II) pathway: Reaction rates and implications for iron-sulfide formation. Geochim. Cosmochim. Acta 72, 4551–4564. doi:10.1016/j.gca.2008.06.019

Cánovas, C.R., Olías, M., Nieto, J.M., Sarmiento, a. M., Cerón, J.C., 2007. Hydrogeochemical characteristics of the Tinto and Odiel Rivers (SW Spain). Factors controlling metal contents. Sci. Total Environ. 373, 363–382. doi:10.1016/j.scitotenv.2006.11.022

Carrero, S., Pérez-López, R., Fernandez-Martinez, A., Cruz-Hernández, P., Ayora, C., Poulain, A., 2015. The potential role of aluminium hydroxysulphates in the removal of contaminants in acid mine drainage. Chem. Geol. 417, 414–423. doi:10.1016/j.chemgeo.2015.10.020

Chapman, B.M., Jones, D.R., Jung, R.F., 1983. Processes controlling metal ion attenuation in acid mine drainage streams. Geochim. Cosmochim. Acta 47, 1957–1973. doi:10.1016/0016-7037(83)90213-2

Combes, J.M., Manceau, A., Calas, G., 1990. Formation of ferric oxides from aqueous solutions: A polyhedral approach by X-ray Absorption Spectroscopy: II. Hematite formation from ferric gels. Geochim. Cosmochim. Acta 54, 1083–1091. doi:10.1016/0016-7037(90)90440-V

Courtin-Nomade, A., Bril, H., Neel, C., Lenain, J.-F., 2003. Arsenic in iron cements developed within tailings of a former metalliferous mine—Enguialès, Aveyron, France. Appl. Geochemistry 18, 395–408. doi:10.1016/S0883-2927(02)00098-7

Cudennec, Y., Lecerf, A., 2005. Topotactic transformations of goethite and lepidocrocite into hematite and maghemite. Solid State Sci. 7, 520–529. doi:10.1016/j.solidstatesciences.2005.02.002

Debye, P., 1915. X-ray dispersal. Ann. Phys. 46, 809–823.

ESRF, n.d. ESRF; The European Synchrotron [WWW Document]. URL http://www.esrf.eu/ (accessed 6.1.16).

Essalhi, M., Sizaret, S., Barbanson, L., Chen, Y., Lagroix, F., Demory, F., Nieto, J.M., Sáez, R., Capitán, M.Á., 2011. A case study of the internal structures of gossans and weathering processes in the Iberian Pyrite Belt using magnetic fabrics and paleomagnetic dating. Miner. Depos. 46, 981–999. doi:10.1007/s00126-011-0361-8

Evangelou, V.P. (Bill), Zhang, Y.L., 1995. A review: Pyrite oxidation mechanisms and acid mine drainage prevention. Crit. Rev. Environ. Sci. Technol. 25, 141–199. doi:10.1080/10643389509388477

Fernandez-Martinez, A., Timon, V., Romaman-Ross, G., Cuello, G.J., Daniels, J.E., Ayora, C., 2010. The structure of schwertmannite, a nanocrystalline iron oxyhydroxysulfate. Am. Mineral. 95, 1312–1322. doi:10.2138/am.2010.3446

Ford, R.G., 2002. Rates of hydrous ferric oxide crystallization and the influence on coprecipitated arsenate. Environ. Sci. Technol. 36, 2459–2463. doi:10.1021/es015768d

Fukushi, K., Sasaki, M., Sato, T., Yanase, N., Amano, H., Ikeda, H., 2003a. A natural attenuation of arsenic in drainage from an abandoned arsenic mine dump. Appl. Geochemistry 18, 1267–1278. doi:10.1016/S0883-2927(03)00011-8

Fukushi, K., Sato, T., Yanase, N., 2003b. Solid-solution reactions in As(V) sorption by schwertmannite. Environ. Sci. Technol. 37, 3581–3586. doi:10.1021/es026427i

Fukushi, K., Sato, T., Yanase, N., Minato, J., Yamada, H., 2004. Arsenate sorption on

schwertmannite. Am. Mineral. 89, 1728–1734.

Gagliano, W.B., Brill, M.R., Bigham, J.M., Jones, F.S., Traina, S.J., 2004. Chemistry and mineralogy of ochreous sediments in a constructed mine drainage wetland. Geochim. Cosmochim. Acta 68, 2119–2128. doi:10.1016/j.gca.2003.10.038

García de Miguel, J.M., 1990. Mineralogía, paragénesis y sucesión de los sulfuros masivos de la Faja Pirítica en el suroeste de la Península Ibérica. Boletín Geológico y Min. 101, 73–105.

García Palomero, F., Bedia Fernández, J.L., García Magariño, M., Sides, E.J., 1986. Nuevas investigaciones y trabajos de evaluación de reservas de Gossan en Minas de Riotinto. Boletín Geológico y Min. 97, 622–642.

Gardiner, D.J., Graves, P.R., Luck, W.A.P., 1990. Practical Raman Spectroscopy. Berichte der Bunsengesellschaft für Phys. Chemie 94, 1047. doi:10.1002/bbpc.19900940938

Gilbert, B., Huang, F., Zhang, H., Waychunas, G.A., Banfield, J.F., 2004. Nanoparticles: Strained and stiff. Science (80-.). 305, 651–654. doi:10.1126/science.1098454

Gimenez, J., Martinez, M., de Pablo, J., Rovira, M., Duro, L., 2007. Arsenic sorption onto natural hematite, magnetite, and goethite. J. Hazard. Mater. 141, 575–580. doi:10.1016/j.jhazmat.2006.07.020

Gualtieri, A.F., Venturelli, P., 1999. In situ study of the goethite-hematite phase transformation by real time synchotron powder diffraction. Am. Mineral. 84, 895–904.

Gusek-Schneider, G.-C., 2002. Congenital ptosis: Amblyogenic refractive errors, amblyopia, manifest strabismus and stereopsis related to the types of ptosis - Data on 77 patients and review of literature . Klin. Monbl. Augenheilkd. 219, 340–348. doi:10.1055/s-2002-32638

Hedin, R.S., Watzlaf, G.R., Nairn, R.W., 1994. Passive treatment of acid mine drainage with limestone. J. Environ. Qual. 23, 1338–1345.

Hollingworth, S.E., Bannister, F.A., 1950. Basaliminite and hydrobasaluminite, two new minerals from Northamptonshire. J. Mineral. Soc. 29, 1–17.

Jage, C.R., Zipper, C.E., Noble, R., 2001. Factors affecting alkalinity generation by successive

alkalinity-producing systems: Regression analysis. J. Environ. Qual. 30, 1015–1022.

Jarvis, a. P., Younger, P.L., 2001. Passive treatment of ferruginous mine waters using high surface area media. Water Res. 35, 3643–3648. doi:10.1016/S0043-1354(01)00089-6

Jönsson, J., Persson, P., Sjöberg, S., Lövgren, L., 2005. Schwertmannite precipitated from acid mine drainage: Phase transformation, sulphate release and surface properties. Appl. Geochemistry 20, 179–191. doi:10.1016/j.apgeochem.2004.04.008

Langmuir, D., 1971. Particle size effect on the reaction goethite = hematite + water.pdf. Am. J. Sci.

Leduc, D., Leduc, L.G., Ferroni, G.D., 2002. Quantification of bacterial populations indigenous to acidic drainage streams. Water. Air. Soil Pollut. 135, 1–21. doi:10.1023/A:1014778301817

Lowson, R.T., 1982. Aqueous Oxidation of Pyrite by Molecular Oxygen. Chem. Rev. 82, 461–497. doi:10.1021/cr00051a001

Macías, F., Caraballo, M.A., Rotting, T.S., Perez-Lopez, R., Nieto, J.M., Ayora, C., 2012a. From highly polluted Zn-rich acid mine drainage to non-metallic waters: Implementation of a multi-step alkaline passive treatment system to remediate metal pollution. Sci. Total Environ. 433, 323–330. doi:10.1016/j.scitotenv.2012.06.084

Macías, F., Caraballo, M. a., Nieto, J.M., Rötting, T.S., Ayora, C., 2012b. Natural pretreatment and passive remediation of highly polluted acid mine drainage. J. Environ. Manage. 104, 93–100. doi:10.1016/j.jenvman.2012.03.027

Maillot, F., Morin, G., Juillot, F., Bruneel, O., Casiot, C., Ona-Nguema, G., Wang, Y., Lebrun, S., Aubry, E., Vlaic, G., Brown, G.E., 2013. Structure and reactivity of As(III)- and As(V)-rich schwertmannites and amorphous ferric arsenate sulfate from the Carnoulès acid mine drainage, France: Comparison with biotic and abiotic model compounds and implications for As remediation. Geochim. Cosmochim. Acta 104, 310–329. doi:10.1016/j.gca.2012.11.016

Mamindy-Pajany, Y., Hurel, C., Marmier, N., Roméo, M., 2011. Arsenic (V) adsorption from aqueous solution onto goethite, hematite, magnetite and zero-valent iron: Effects of pH,

concentration and reversibility. Desalination 281, 93–99. doi:10.1016/j.desal.2011.07.046

Manceau, A., 1995. The mechanism of anion adsorption on iron oxides: Evidence for the bonding of arsenate tetrahedra on free Fe(O, OH)6 edges. Geochim. Cosmochim. Acta 59, 3647–3653. doi:10.1016/0016-7037(95)00275-5

Manceau, A., Drits, A., 1993. Local Structure of Ferrihydrite and Feroxyhite by EXAFS Spectroscopy. Clay Miner. 28, 165–184. doi:10.1180/claymin.1993.028.2.01

Marcoux, E., Moëlo, Y., Leistel, J.M., 1996. Bismuth and cobalt minerals as indicators of stringer zones to massive sulphide deposits, Iberian Pyrite Belt. Miner. Depos. 31, 1–26.

Moreno, C., 1993. Postvolcanic Paleozoic of the Iberian Pyrite Belt: an example of basin morphologic control on sediment distribution in a turbidite basin. J. Sediment. Petrol. 63, 1118–1128. doi:10.1306/D4267CBC-2B26-11D7-8648000102C1865D

Moreno, C., Sierra, S., Saez, R., 1996. Evidence for catastrophism at the Famennian-Dinantian boundary in the Iberian Pyrite Belt. Recent Adv. Low. Carbonif. Geol. 153–162.

Moses, C.O., Kirk Nordstrom, D., Herman, J.S., Mills, A.L., 1987. Aqueous pyrite oxidation by dissolved oxygen and by ferric iron. Geochim. Cosmochim. Acta 51, 1561–1571. doi:10.1016/0016-7037(87)90337-1

Nesbitt, R.W., Pascual, E., Fanning, C.M., Toscano, M., Sáez, R., Almodóvar, G.R., 1999. U–Pb dating of stockwork zircons from the eastern Iberian Pyrite Belt. J. Geol. Soc. London. 156, 7–10. doi:10.1144/gsjgs.156.1.0007

Nieto, J.M., Almodóvar, G.R., Pascual, E., Jagoutz, R.S.Y.E., 2000. Evidencias isotópicas sobre el origen de los metales en los sulfuros masivos de la Faja Pirítica Ibérica. Cuad. Lab. Xeol. Laxe 25, 139–142.

Nocete, F., Sáez, R., Bayona, M.R., Nieto, J.M., Peramo, A., López, P., Gil-Ibarguchi, J.I., Inácio, N., García, S., Rodríguez, J., 2014. Gold in the Southwest of the Iberian Peninsula during the 3rd Millennium BC. J. Archaeol. Sci. 41, 691–704. doi:10.1016/j.jas.2013.10.006

Nordstrom, D.K., 1982a. Aqueous pyrite oxidation and the consequent formation of secondary

iron minerals, in: Kittrick, J.A., Fanning, D.S., Hossner, L.R. (Eds.), Acid Sulfate Weathering. Soil Science Society of America Publication, pp. 37–56.

Nordstrom, D.K., 1982b. The effect of sulfate on aluminum concentrations in natural waters: some stability relations in the system Al2O3-SO3-H2O at 298 K. Geochim. Cosmochim. Acta 46, 681–692. doi:10.1016/0016-7037(82)90168-5

Nordstrom, D.K., Alpers, C.N., 1999a. Geochemistry of acid mine waters, in: Plumlee, G.S., Logsdon, M.J. (Eds.), The Enviromental Geochemistry of Mineral Deposits. Society of Economic Geologists, Littleton, pp. 133–160.

Nordstrom, D.K., Alpers, C.N., 1999b. Geochemistry of acid mine waters. Soc. Econ. Geol. 6A, 133–160.

Nordstrom, D.K., Southam, G., 1997. Geomicrobiology of sulfide mineral oxidation. Rev. Mineral. 35, 381–390.

Olías, M., Nieto, J.M., Sarmiento, a. M., Cerón, J.C., Cánovas, C.R., 2004. Seasonal water quality variations in a river affected by acid mine drainage: The Odiel River (South West Spain). Sci. Total Environ. 333, 267–281. doi:10.1016/j.scitotenv.2004.05.012

Paikaray, S., Göttlicher, J., Peiffer, S., 2012. As(III) retention kinetics, equilibrium and redox stability on biosynthesized schwertmannite and its fate and control on schwertmannite stability on acidic (pH 3.0) aqueous exposure. Chemosphere 86, 557–564. doi:10.1016/j.chemosphere.2011.07.055

Paikaray, S., Göttlicher, J., Peiffer, S., 2011. Removal of As(III) from acidic waters using schwertmannite: Surface speciation and effect of synthesis pathway. Chem. Geol. 283, 134–142. doi:10.1016/j.chemgeo.2010.08.011

Paikaray, S., Peiffer, S., 2012. Abiotic schwertmannite transformation kinetics and the role of sorbed As(III). Appl. Geochemistry 27, 590–597. doi:10.1016/j.apgeochem.2011.12.013

Parviainen, A., Cruz-Hernández, P., Pérez-López, R., Nieto, J.M., Delgado-López, J.M., 2015. Raman identification of Fe precipitates and evaluation of As fate during phase transformation in Tinto and Odiel River Basins. Chem. Geol. 398, 22–31. doi:10.1016/j.chemgeo.2015.01.022

Pérez-López, R., Asta, M.P., Román-Ross, G., Nieto, J.M., Ayora, C., Tucoulou, R., 2011. Synchrotron-based X-ray study of iron oxide transformations in terraces from the Tinto-Odiel river system: Influence on arsenic mobility. Chem. Geol. 280, 336–343. doi:10.1016/j.chemgeo.2010.11.021

Raman, C. V, Krishnan, K.S., 1928. A new type of secondary radiation [11]. Nature 121, 501–502.

Regenspurg, S., Peiffer, S., 2005. Arsenate and chromate incorporation in schwertmannite. Appl. Geochemistry 20, 1226–1239. doi:10.1016/j.apgeochem.2004.12.002

Rimstidt, D.D., Vaughan, D.J., 2003. Pyrite oxidation: A state-of-the-art assessment of the reaction mechanism. Geochim. Cosmochim. Acta 67, 873–880. doi:10.1016/S0016-7037(02)01165-1

Roca, A., Viñals, J., Arranz, M., Calero, J., 1999. Characterization and Alkaline Decomposition/Cyanidation of Beudantite–Jarosite Materials From RIO Tinto Gossan Ores. Can. Metall. Q. 38, 93–103. doi:10.1179/cmq.1999.38.2.93

Röting, T., Ayora, C., Carrera, J., 2003. Passive treatment of Acid Mine Drainage with high metal concentrations : Results from experimental treatment tanks in the Iberian Pyrite Belt (SW Spain). Proc. 9th Int. Mine Water Assoc. Congr. Oviedo, Spain 641–647.

Rötting, T.S., Thomas, R.C., Ayora, C., Carrera, J., 2008. Passive treatment of acid mine drainage with high metal concentrations using dispersed alkaline substrate. J. Environ. Qual. 37, 1741–1751. doi:10.2134/jeq2007.0517

Sáez, R., Almodóvar, G.R., Pascual, E., 1996. Geological constraints on massive sulphide genesis in the Iberian Pyrite Belt. Ore Geol. Rev. 11, 429–451. doi:10.1016/S0169-1368(96)00012-1

Sáez, R., Pascual, E., Toscano, M., Almodóvar, G.R., 1999. The Iberian type of volcano-sedimentary massive sulphide deposits. Miner. Depos. 34, 549–570. doi:10.1007/s001260050220

Sánchez, L., Cruells, M., Roca, A., 1996. Sulphidization-cyanidation of jarosite species: Applicability to the gossan ores of Rio Tinto. Hydrometallurgy 42, 35–49.

doi:10.1016/0304-386X(95)00076-S

Schermerhorn, L.J.G., 1971. An outline stratigraphy of the Iberian Pyrite Belt. Boletín Geológico y Min. 82, 23–52.

Schroth, A.W., Parnell, R.A., 2005. Trace metal retention through the schwertmannite to goethite transformation as observed in a field setting, Alta Mine, MT. Appl. Geochemistry 20, 907–917. doi:10.1016/j.apgeochem.2004.09.020

Schwertmann, U., Bigham, J.M., Murad, E., 1995. The 1st Occurrence of Schwertmannite in a Natural Stream Environment. Eur. J. Mineral. 7, 547–552.

Scott, K.M., Ashley, P.M., Lawie, D.C., 2001. The geochemistry, mineralogy and maturity of gossans derived from volcanogenic Zn-Pb-Cu deposits of the eastern Lachlan Fold Belt, NSW, Australia. J. Geochemical Explor. 72, 169–191. doi:10.1016/S0375-6742(01)00159-5

Silva, J.B., Oliveira, J.T., Ribeiro, A., 1990. Pre-Mesozoic Geology of Iberia, in: Dallmeyer, R.D., Garcia, E.M. (Eds.), . Springer Berlin Heidelberg, Berlin, Heidelberg, pp. 348–362. doi:10.1007/978-3-642-83980-1_24

Singer, P.C., Stumm, W., 1970. Acidic Mine Drainage: The Rate-Determining Step. Science (80-.). 167, 1121–1123.

Stipp, S.L.S., Hansen, M., Kristensen, R., Hochella, M.F., Bennedsen, L., Dideriksen, K., Balic-Zunic, T., Léonard, D., Mathieu, H.J., 2002. Behaviour of Fe-oxides relevant to contaminant uptake in the environment. Chem. Geol. 190, 321–337. doi:10.1016/S0009-2541(02)00123-7

Strauss, G.K., Madel, J., 1974. Geology of massive sulphide deposits in the Spanish-Portuguese Pyrite Belt. Geol. Rundschau 63, 191–211. doi:10.1007/BF01820984

Tornos, F., 2006. Environment of formation and styles of volcanogenic massive sulfides: The Iberian Pyrite Belt. Ore Geol. Rev. 28, 259–307. doi:10.1016/j.oregeorev.2004.12.005

Velasco, F., Herrero, J.M., Suárez, S., Yusta, I., Alvaro, A., Tornos, F., 2013. Supergene features and evolution of gossans capping massive sulphide deposits in the Iberian Pyrite Belt.

Ore Geol. Rev. 53, 181–203. doi:10.1016/j.oregeorev.2013.01.008

Viñals, J., Roca, A., Cruells, M., Núñez, C., 1995. Characterization and Cyanidation of Río Tinto gossan ores. Can. Met. Q. 34, 115–122.

Wang, X., Gu, C., Feng, X., Zhu, M., 2015. Sulfate Local Coordination Environment in Schwertmannite. Environ. Sci. Technol. 49, 10440–10448. doi:10.1021/acs.est.5b02660

Waychunas, G.A., Kim, C.S., Banfield, J.F., 2005. Nanoparticulate iron oxide minerals in soils and sediments: Unique properties and contaminant scavenging mechanisms. J. Nanoparticle Res. 7, 409–433. doi:10.1007/s11051-005-6931-x

Waychunas, G.A., Rea, B.A., Fuller, C.C., Davis, J.A., 1992. Surface chemistry of ferrihydrite: Part 1.EXAFS studies ongeometrie of coprecipitated and adsorbed arsenate 57, 2251–2269.

Waychunas, G.A., Xu, N., Fuller, C.C., Davis, J.A., Bigham, J.M., 1995. XAS study of AsO 3- and SeO 2- substituted schwertmannites. Phys. B 209, 481–483.

Webster, J.G., Swedlund, P.J., Webster, K.S., 1998. Trace Metal Adsorption onto an Acid Mine Drainage Iron (III) Oxy Hydroxy Sulfate. Environ. Sci ence Technol. 32, 1361–1368. doi:DOI: 10.1021/es9704390

Williams, D., 1950. Gossanized breccia-ores, jarosites and jaspers at Rio Tinto, Spain. Bull. Inst. Min. Met. 526, 1–12.

Woodwell, G.M., Craig, P.P., Johnson, H.A., 1971. DDT in the biosphere: Where does it go? Science (80-.). 174, 1101–1107.

Yesares, L., Sáez, R., Ruiz De Almodóvar, G., Nieto, J.M., Gómez, C., Ovejero, G., 2017. Mineralogical evolution of the Las Cruces gossan cap (Iberian Pyrite Belt): From subaerial to underground conditions. Ore Geol. Rev. 80, 377–405. doi:10.1016/j.oregeorev.2016.05.018

Younger, P.L., 2000. The adoption and adaptation of passive treatment technologies for mine waters in the United Kingdom. Mine Water Environ. 19, 84–97. doi:10.1007/BF02687257

Zhu, M., Legg, B., Zhang, H., Gilbert, B., Ren, Y., Banfield, J.F., Waychunas, G. a., 2012. Early stage

formation of iron oxyhydroxides during neutralization of simulated acid mine drainage solutions. Environ. Sci. Technol. 46, 8140–8147. doi:10.1021/es301268g

CHAPTER II

RAMAN IDENTIFICATION OF FE PRECIPITATES AND EVALUATION OF AS FATE DURING PHASE TRANSFORMATION IN TINTO AND ODIEL RIVER BASINS

BASED ON:

PARVIAINEN, A., CRUZ-HERNÁNDEZ, P., PÉREZ-LÓPEZ, R., NIETO, J.M., DELGADO-LÓPEZ, J.M., 2015. RAMAN IDENTIFICATION OF FE PRECIPITATES AND EVALUATION OF AS FATE DURING PHASE TRANSFORMATION IN TINTO AND ODIEL RIVER BASINS. **CHEMCAL GEOLOLOGY** 398, 22–31. DOI:10.1016/J.CHEMGEO.2015.01.022

RAMAN IDENTIFICATION OF FE PRECIPITATES AND EVALUATION OF AS FATE DURING PHASE TRANSFORMATION IN TINTO AND ODIEL RIVER BASINS

Newly-formed Fe terrace samples and corresponding water samples of Tinto and Odiel River, as well as, ancient terrace samples representing conditions of ancient Tinto River, were collected and studied by optical microscopy, Raman spectroscopy, X-ray diffraction, scanning electron microscopy, microprobe analysis, pseudo-total digestions, and by chemical analytics. The newly-formed terraces showed that currently schwertmannite is precipitating on the riverbed acting as a sink for arsenic. In a matter of months, this metastable phase transforms into goethite and, eventually, jarosite which are found in the deeper sediments below one centimeter. Due to long-term transformation, well-crystallized goethite and diagenetic hematite were the major phases in the ancient terraces. The microanalyses suggested that goethite retained slightly higher concentrations of As than hematite suggesting As is mobilized in the transformation process. Additionally, this study shows that Raman spectroscopy is an efficient tool in the mineralogical characterization of Fe(III) oxides, hydroxides, and oxyhydroxysulfates at micro to millimeter scale in these types of samples. However, Raman spectra did not provide insights on the incorporation of As within the crystal lattice of schwertmannite, probably due to its low concentration.

2.1 Introduction

The outcropping massive sulfides of the Iberian Pyrite Belt (IPB) and the subsequent formation of gossans (thick cap of iron oxides formed as a result of chemical weathering) have influenced the microbiochemistry of the Tinto and Odiel River basins, SW Spain (Nieto et al., 2013; Nieto et al., 2007). Sulfide oxidation led to natural Acid Rock Drainage (ARD) over millions of years, and intensive mining since 4500 years ago (Nocete et al., 2014) provoked Acid Mine Drainage (AMD) enhancing the extreme acidic conditions of the river systems. Over prolonged time span a unique microbiochemical environment was created, and iron oxyhydroxides and oxyhydroxysulfates precipitated forming terrace-like iron formations i.e. the precipitates settled as thick, stepped iron accumulations on the riverbed. The ancient Fe terraces are located tens of meters above the current river and they may be as old as several million years (Fernández-Remolar et al., 2005; Essalhi et al., 2011).Tinto River has been pointed out as a terrestrial analog to iron formations on Early Earth and Meridiani Planum on Mars (Fernández-Remolar et al., 2005).

In AMD-after mining environments, metastable schwertmannite [$Fe_8O_8(OH)_{5.5}(SO_4)_{1.25}$] has proven to be good at scavenging arsenic (AsV) from solution (Acero et al., 2006; Asta et al., 2010). However, over time the schwertmannite tends to transform spontaneously into more crystalline phases such as goethite [α-$FeOOH$] in a matter of months (Acero et al., 2006). Bigham et al. (1996) describes this reaction:

$$Fe_8O_8(OH)_{5.5}(SO_4)_{1.25(s)} + 2.5H_2O \rightarrow 8FeOOH_{(s)} + 1.25SO_{4(aq)}^{2-} + 2.5H_{(aq)}^{+} \qquad \text{Eq (2.1)}$$

The eventual precipitation of jarosite [$KFe_3(SO_4)_2(OH)_6$] is also reported (Acero et al., 2006). On a longer time scale of centuries, goethite is transformed into hematite [Fe_2O_3] through diagenetic processes (Pérez-López et al., 2011) according to the following reaction described by Langmuir, (1971):

$$2FeOOH_{(s)} \rightarrow Fe_2O_{3(s)} + H_2O_{(aq)} \qquad \text{Eq (2.2)}$$

Identifying these phases and quantifying the potentially toxic elements that they may carry by adsorption or co-precipitation is important in assessing contaminated soils and sediments. Moreover, the search for stability in this type of poorly crystalline iron oxyhydroxysulfate could determine the fate of arsenic with time, and what is now considered a sink could become a long-term source of contamination.

Raman micro-spectroscopy has many applications including biotechnology, mineralogy, environmental monitoring, material science, pharmaceutical etc. (Das and Agrawal, 2011). In recent studies it has also proven as an efficient method for characterizing Fe(III) oxides, hydroxides, and oxyhydroxysulfates (Burton et al., 2009; Courtin-Nomade et al., 2003; Das and Hendry, 2011; Frost et al., 2005; Mazzetti and Thistlethwaite, 2002; Müller et al., 2010). This study focused on the iron-rich alluvial terraces of different ages in the Tinto and Odiel Rivers. The mineralogical and geochemical composition was studied by optical microscopy, Raman μ-spectroscopy, scanning electron microscope equipped with energy dispersive X-ray spectroscopy (SEM-EDX), electron microprobe analysis (EMPA), bulk powder X-ray diffraction (XRD), and by a pseudo-total digestion. Raman spectroscopy was used to study the mineralogical composition in millimeter scale in undisturbed samples, and the effectiveness of this technique for identifying mineral phases was verified by comparing the Raman spectra and XRD diffractograms of the ground bulk samples.

2.2 Materials and Methods

2.2.1 Site description

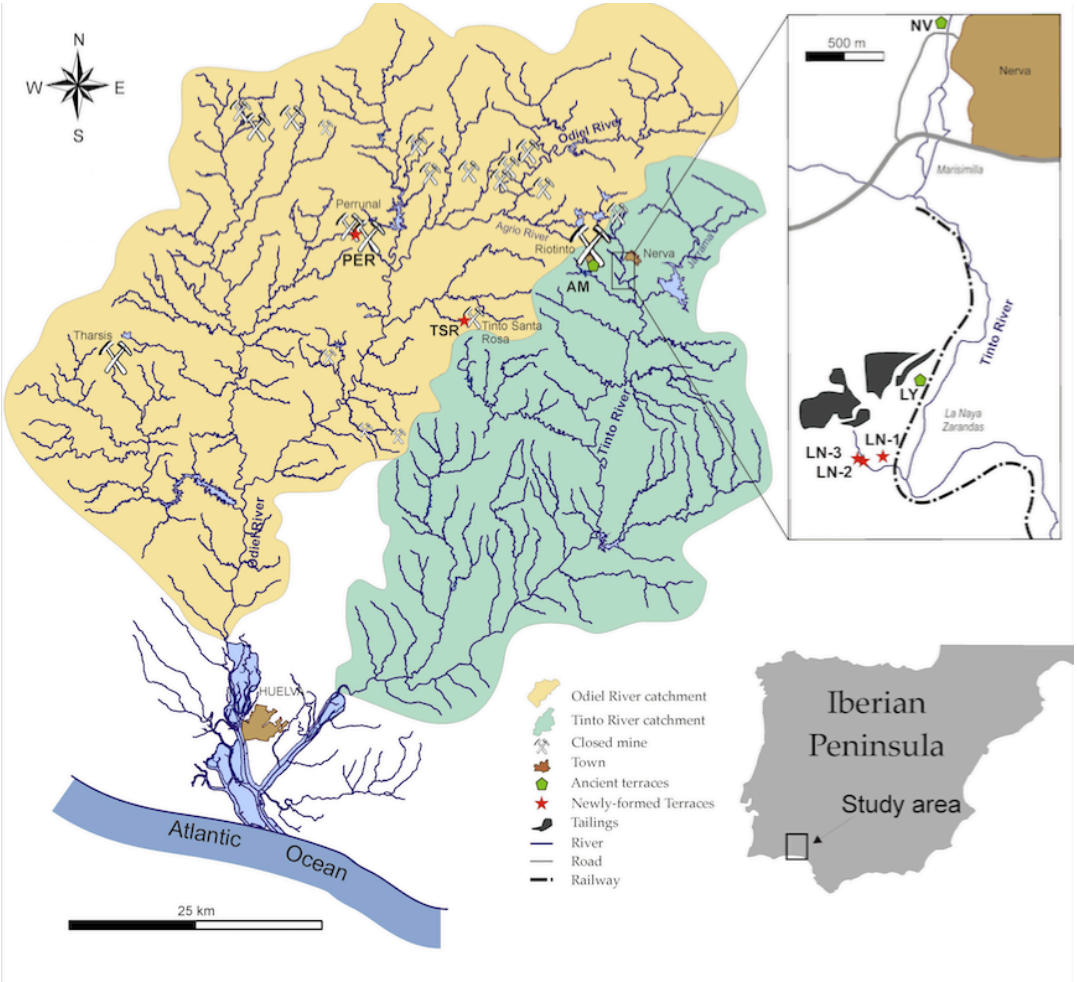

Fig. 2.1: *Index map showing the Tinto and Odiel River catchments and the sampling sites. The recent terrace samples are marked with red stars and ancient samples with green pentagon. The map was modified from* (Sarmiento et al., 2009).

Tinto and Odiel River Basins cross through the IPB, which is one of the largest massive sulfide deposits worldwide with estimated total reserves of over 1700 Mt (Leistel et al., 1998; Sáez et al., 1999). The IPB extends from south of Lisbon in Portugal to north of Seville in Spain. The ore deposits, consisting mainly of metal sulfides (*e.g.* pyrite [FeS_2], pyrrhotite [$Fe_{(1-x)}S$], chalcopyrite [$CuFeS_2$], sphalerite [ZnS], galena [PbS], arsenopyrite [$FeAsS$], tetrahedrite - tennantite [$(Cu,Fe)_{12}Sb_4S_{14}$ - $Cu_{12}As_4S_{13}$)] and hosted by shales and

volcanic rocks, were formed from the Late Devonian to the Early Carboniferous (Tornos, 2006). Parts of the ore deposits have been exposed to atmospheric conditions over a prolonged period since Oligocene, *i.e.* over 24 Ma (Essalhi et al., 2011) causing the oxidation of sulfides, natural ARD, and deposition of iron-rich sediments in the riverbeds. These authors suggest that the formation of the iron terraces probably was a continuous process. The older terraces represent natural conditions before mining era, whereas due to extensive mining in the area since 2500 B.C. (Nocete et al., 2014) the water quality further decreased and the same terraces but associated with AMD processes occurred since then. Over a hundred mines have operated in the area during the last centuries (Tornos, 2006), which discharge their highly-polluted acidic leachates into the river systems. Nearly all of the mining districts are currently abandoned representing an almost inexhaustible source of AMD, characterized by low pH (0.88-3.2) and high elemental concentrations (Asta et al., 2010; Egal et al., 2008; Hubbard et al., 2009; J. M. Nieto et al., 2013). As a consequence, iron terraces precipitate reflecting the mining impact.

2.2.2 Sampling, sample preparation, and analysis

On the one hand, water and undisturbed samples of newly-formed iron terraces were collected in some AMD-affected streams of three abandoned mine districts. The terrace samples were collected at La Naya (LN) district within the Tinto river basin in October 2012 and February 2013, whereas water samples were only collected during the latter sampling campaign. The sample LN-1 was collected at an underground gallery pithead (tunnel 16), and samples LN-2 and LN-3 were taken from a nearby ditch receiving water from pyrite-rich tailings. The sample LN-3 represents a recent terrace located only few meters from the current flow path of the ditch that was formed probably a few years ago. Moreover, solid and water samples were collected at Tinto Santa Rosa (TSR) and Perrunal (PER) districts within the Odiel river basin in February 2013 (Fig. 1). On the other hand, solid samples were taken in October 2012 from ancient terraces of the Tinto River at formations outcropping at La Naya (LY), Nerva (NV), and Alto de la Mesa (AM). The ancient terraces of LY and NV are located 10 to 15 m above the current riverbed, whereas AM has the highest location at 60 m being the oldest formation. The Alto de la Mesa terraces are defined as an alluvial deposit with alternating sequences of coarse and fine sediment layers as a consequence of different flow regimens. The sample AM-1 corresponds to distal and AM-2D to proximal location in the ancient Tinto River, and the other samples represent intermediate locations.

The water samples were filtered with 0.45 μm nylon filters and acidified with HNO_3 to pH 1 in the field. In the laboratory they were kept at 4°C until analysis. The pH, redox potential (Eh), and electric conductivity (EC) were measured in the field using a portable Multiparametric Cison Mm 40+ equipment, and both dissolved oxygen (DO) and temperature were measured in the field using Hanna Instruments HI 9142. Water samples were analyzed for trace and major elements using by inductively coupled plasma mass spectrometry (ICP-MS, X-series II Thermo instrument) and inductively coupled plasma optical emission spectrometry (ICP-OES, Thermo Jarrel-Ash instrument), respectively, at Institute of Environmental Assessment and Water Research (CSIC Barcelona). The detection limits were on the order of 1 ppb for traces and between 1 and 0.2 ppm for major elements.

The newly-formed sediments were dried at room temperature at the laboratory. Polished thin sections of approx. 50 μm were prepared of all solid samples using epoxy resin and polyester resin. They were examined by reflected-light optical microscope, SEM-EDX and EMPA qualitative chemical characterization, and Raman μ-spectroscopy for mineralogical identification of the iron phases. Additionally, the newly-formed terraces and samples LY-2B and AM-2D were divided into subsamples according to the observed layering where number one corresponds to the top layer and the lowest sample corresponds to the average depth of 3 to 5 cm depending on the sample thickness. Aliquots of all of the solid samples were ground using an agate mortar. The ground samples were investigated using bulk XRD, Raman spectroscopy, and chemical digestion.

The acceleration voltage of the Leo 1430VP SEM equipped with EDX (Oxford instruments, INCA 350) was set to 20 keV and the beam current to 80 nA at the Centro de Servicios Científicos (CIC) at the University of Granada. The JEOL JXA 8200 EMPA was set to 15 keV and beam current of 10 nA was used at the University of Huelva. The exposure time of the microprobe was prolonged to 100 s in order to better gauge the trace elements that appear in concentrations close to their detection limits. Additionally, to better quantify the trace concentrations in the terrace samples, aliquots of 0.2 g of ground samples were digested with *aqua regia* which is considered as a pseudo-total digestion. The chemistry of these samples was analyzed by ICP-MS and ICP-OES at Institute of Environmental Assessment and Water Research (CSIC Barcelona). Raman spectra were collected with a LabRAMHR spectrometer (Jobin–Yvon, Horiba, Japan) with backscattering geometry at Instituto Andaluz de Ciencias de la Tierra (IACT). The excitation beam (a diode laser emitting at 784 nm) was focused with a confocal Olympus microscope. Raman signals were collected in a Peltier-cooled

CCD detector (1064 x 256 pixels). The spectral range was from 150 to 1350 cm^{-1} at a resolution of 3 cm^{-1}. Raman shift calibration was performed using the 521 cm^{-1} line of silicon standard. To avoid sample degradation and transformation of mineral phases, a filter (D0.3 or D0.6) was used for the thin sections. The acquisition time was set to 300 s with 2 to 4 accumulations, and x50 objective was used. The thin sections were analyzed making a cross section from the surface to bottom of each sample in order to observe the mineral transformation in detail. On the other hand, the Raman spectra of the ground samples were obtained as signal average of two spectra, during 150 s each. Due to the high probability of degradation of the ground samples, the laser was focused through a x10 objective and a D1 filter was used to reduce its power on the sample surface. The spectra were linearly baseline corrected for clarity. The bulk powder XRD was performed by using PANanalytical X'Pert PRO with Cu Kα radiation at IACT. Diffractometer settings were: 45 kV, 40 mA, and a scan range of 4–60° 2θ and 4–70° 2θ for newly-formed and ancient samples, respectively, with 0.0084° 2θ step size and 100-s counting time per step.

2.3 Results and Discussion

2.3.1 Newly-formed Fe terraces

The physicochemical characteristic and chemistry of the water samples collected in the respective sampling sites of the newly-formed terraces are presented in Table 1 exhibiting low pH and heavy contamination (e.g. Al, As, Ca, Co, Cu, Fe, Mg, Mn, Ni, Pb,Zn, as well as SO_4) derived from AMD at all of the studied mining districts. The water chemistry is reflected in the following mineralogical and geochemical description of the terrace samples. Table 2 resumes the mineralogical observations made for the ground bulk samples using Raman and XRD, highlighting the consistent results. The detailed microscopic observations combined with Raman studies on the thin sections allowed the identification of the mineral phases at a micro to millimeter scale and the characterization of their textural relationships (Figs. 2 and 3). The sample LN-1 was taken from a less consolidated terrace than LN-2 and LN-3. This sample consisted principally of schwertmannite and goethite. Figure 2a shows the branch-like, porous texture of this terrace. The Raman spectroscopy revealed that the schwertmannite precipitated on the top of the terrace and gradually transformed into goethite, which was more abundant in the deeper sections of the sample. The same trend was also observed in the XRD patterns from different depths (Figs. 4a and 4b corresponding to top and bottom layers, respectively), and both Raman and XRD results for ground samples suggested the presence of traces of jarosite. The sample LN-2 had a crusty surface and a layered texture consisting of spherical aggregates exhibiting three major phases with schwertmannite, jarosite, and goethite. The more compact surface layer was made of pure schwertmannite, and thereafter, schwertmannite had altered and appeared with jarosite and goethite. Jarosite typically appeared as yellowish green patches or bordering pore spaces (Fig. 2f). In LN-2, schwertmannite was completely transformed and disappeared at the depth of 2 cm after which jarosite and goethite were present as mixtures and/or independent monomineralic layers. Jarosite was found most abundantly in the LN-2 out of all of the solid samples. This is explained by the high sulfate concentration and the low pH in the respective water sample (Table 1) (Bigham et al., 1996). Small amounts (<2 %) of detrital particles (∅ <1 mm) consisting primarily of quartz, sulfides, hematite, and goethite were present in between the chemical sediments as a consequence of heavy rain events dragging fragments from upstream. The compact matrix of the few years old terrace sample, LN-3, consisted of goethite and

jarosite, and the abundant detrital material composed of elongated grains of shale (∅ 3-10 mm), fragments of botryoidal goethite and hematite (∅ <1 mm), and scarce sulfide grains prone to *in-situ* oxidation. The LN-3 did not present mineralogical layering. The samples TSR and PER, in turn, exhibited a crusty surface and a layered structure with alternating compact and more porous branch-like layers (Figure 2g-l). In both samples, schwertmannite was found as a monomineralic layer of 0.5 to 1 cm in thickness on the top (Fig. 4c). Below these layers schwertmannite appeared together with goethite in TSR (Fig. 4d) and with goethite and jarosite in PER as a consequence of the phase transformation over time, though schwertmannite almost faded away and was barely detected in the XRD pattern.

Sample	LN-1	LN-2	TSR	PER
pH	2.53	2.93	3.12	2.84
Eh	423	382	382	419
EC	10.9	7.47	3.24	4.77
O_2	67 / 6.08	94 / 9.42	85 / 8.05	70 /8.03
T	17	14	15	14
As	0.210	0.171	1.42	2.94
Co	5.23	1.65	0.773	1.12
Cu	92.3	7.99	12.0	21.8
Ni	0.710	0.309	0.510	0.708
Pb	0.172	0.064	bdl	0.087
Zn	248	44.2	53.1	43.9
Al	476	241	75.8	411
Ca	184	448	152	263
Fe	2281	4568	586	2714
Mg	958	934	115	371
Mn	105	107	30.8	69.6
SO_4	12141	14471	2494	8572

Table 2.1: *Physicochemical parameters of the water samples including pH, redox potential (Eh, mV), electric conductivity (EC, mS/cm²), oxygen saturation (O_2, % and ppm), and temperature (T, ºC) and the water chemistry of selected elements of interest and SO_4 (mg/L). (bdl = below detection limit).*

Figure 3 shows the Raman spectra of schwertmannite, jarosite, and goethite defined in LN-2. The well-defined bands of schwertmannite (Fig. 3A) coincide with previously reported spectra by Mazzetti and Thistlethwaite (2002) and (Burton et al., 2009). The Raman spectrum for jarosite (Fig. 3B) is in agreement with the data reported by (Courtin-Nomade et al., 2003) Courtin-Nomade et al. (2003), (Frost et al., 2005) Frost et al. (2005) and (Filippi et

al., 2007) Filippi et al. (2007). The bands appearing in the spectrum of goethite (Fig. 3C) match with the ones described by (Froment, F., Tournié, A., Colomban, 2008)Froment et al. (2008) and (Müller et al., 2010) Müller et al. (2010). Additionally, areas with mineral transition were detected with schwertmannite mixed with jarosite and goethite (Fig. 3D,E). The Raman spectra of schwertmannite, jarosite, and goethite from LN-1, LN-3, TSR, and PER were nearly identical to ones in LN-2, hence are not presented here.

Sample	XRD	Raman	**Sample**	XRD	Raman	**Sample**	XRD	Raman
LN-1-1	sw, ja	sw	**TSR-2**	sw, q	sw	**LY-2B-3**	go	go
LN-1-2	sw, go (ja)	sw, go (ja)	**TSR-3**	sw, q (go)	sw (go)	**LY-2C**	go	go
LN-1-3	go, sw	go (sw)	**TSR-4**	sw (go)	sw, go	**LY-2D**	go, hm	go, hm
LN-1-4	go, sw	go, sw	**TSR-5**	go, sw, q	go, sw	**NV-1**	hm, go	hm, go
LN-1-5	go, sw	go, sw	**TSR-6**	go	go	**NV-1A**	hm	hm
LN-1-6	go, sw, ja	go, sw	**PER-1**	sw	sw	**NV-1B**	hm, go	hm, go
LN-2-1	go, ja, sw	go, ja (sw)	**PER-2**	sw, go, ja	sw, go	**AM-1**	hm, go	hm, go
LN-2-2	go, ja	go, ja (sw)	**PER-3**	go, ja, sw	go, sw	**AM-2A**	hm, go	hm, go
LN-2-3	go, ja	go, ja	**PER-4**	go, ja, sw	go, sw	**AM-2B**	hm, go, q	hm (go)
LN-2-4	go, ja, sw	go	**PER-5**	go, ja, sw	go, sw	**AM-2C**	hm, go, q	hm
LN-3-1	go, ja	go, ja	**PER-6**	go	go	**AM-2D-1**	go, hm, q	go, hm
LN-3-2	go, ja	go, ja	**LY-2A**	go	go	**AM-2D-2**	go, hm, q	go, hm
TSR-C1	sw	sw, go	**LY-2B-1**	go	go	**AM-2D-3**	go, hm, q	go, hm
TSR-1	sw, q	sw, go	**LY-2B-2**	go	go	**AM-2D-4**	go, hm, q	go, hm

Table 2.2: *Mineralogy of ground newly-formed and ancient terrace samples according to the results of XRD and Raman spectroscopy. The samples LN-1, LN-2, LN-3, TSR, PER, LY-2B, and AM-2D were divided into subsamples where number one corresponds to the top layer and thereafter consecutive layering. Minerals are marked in relative order of abundance and in parenthesis when appeared in considerably lesser amount (sw= schwertmannite; ja = jarosite; go = goethite; hm = hematite; q = quartz).*

The SEM, EMPA analyses, and the pseudo-total digestion showed that the newly-formed terraces contain traces of As, Co, Cu, Pb, and Zn (Table 3). In the solid samples LN-1, LN-2, and PER the average concentrations of As by EMPA were generally well below 1000 mg/kg. However, the newly-formed sediments of TSR exhibited exceptionally high values of As with up to 34550 mg/kg in the schwertmannite layer (average 14290 mg/mg). Similar values for As in the Tinto Santa Rosa mine were reported by (Asta et al., 2010) Asta et al. (2010). Here, As concentrations were higher in the schwertmannite layer than in the deeper layer with goethite and/or mixture of goethite with schwertmannite. In the other samples, the distribution of As in the detected mineral phases was not so clear. The point microanalysis by EMPA showed generally higher trace concentrations in all of the samples except for PER,

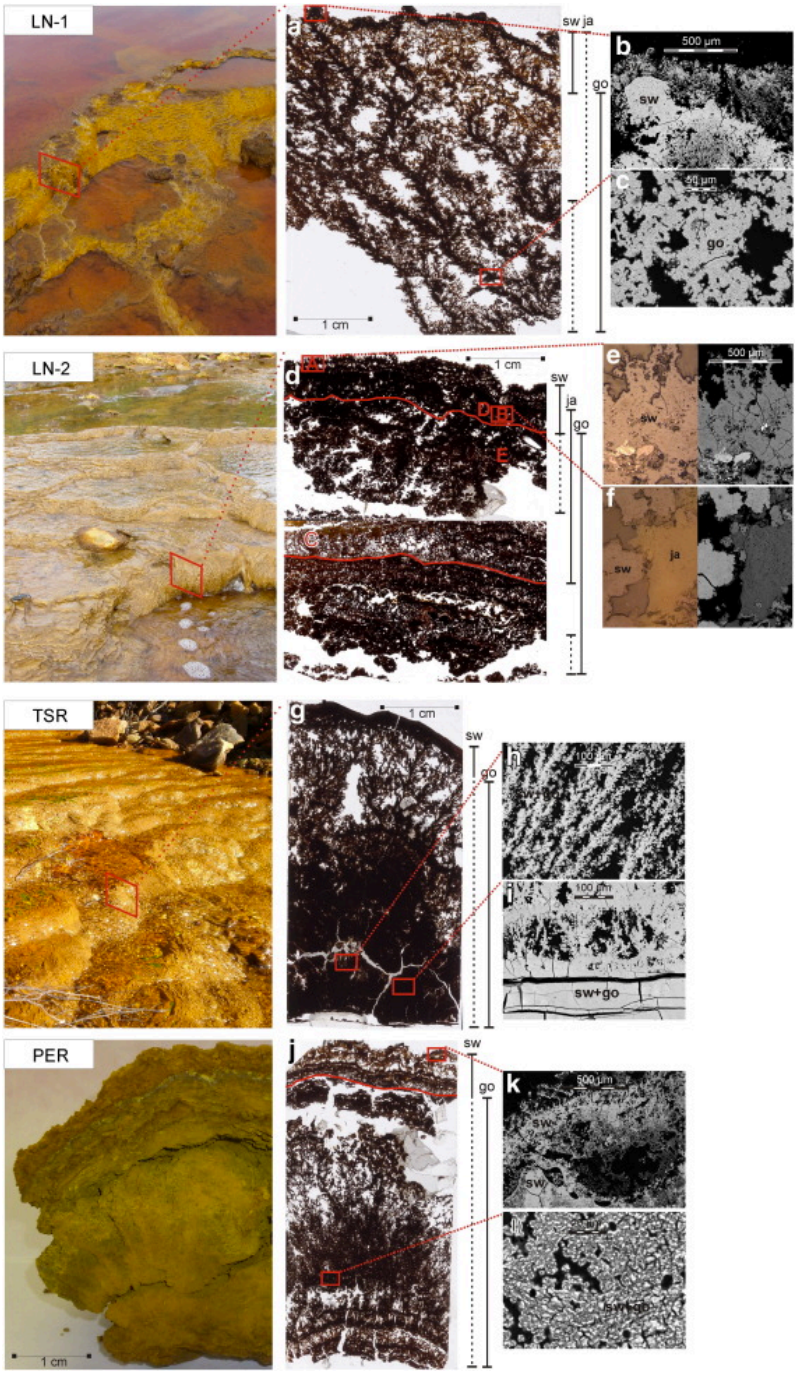

Figure 2.2: *Field, microscope, and back-scattered images of newly-formed Fe terraces. The analysis points of Raman spectra shown in the Fig. 3 (A-E) are indicated in the thin section (d), and the overall mineralogical composition identified by Raman spectroscopy is indicated next to the scanned thin sections (a, d, g, j). Minor phases are marked with dashed line. Additionally, the mineralogical description in the optical microscopy and backscattered images is based on Raman identification (sw= schwertmannite; ja = jarosite; go = goethite).*

whereas the results of the pseudo-total digestions represented the homogenized bulk sample which explains the differences in the results of each analysis method.

2.3.2 Ancient Fe terraces

All of the ancient terrace samples exhibited similar mineralogical composition with varying contents of goethite and hematite (Figs. 5 and 6). The oldest terraces of Alto de la Mesa, dated to 6 Ma (Essalhi et al., 2011) contained more hematite accompanied with goethite (AM-1, AM-2A, AM-2B, AM-2C), except for one sample (AM-2D) which contained goethite as major phase. In the AM-2C, hematite was the single phase observed during the Raman studies. However, the presence of minor amounts of goethite was suggested by XRD pattern. The sample AM-1 corresponds to a coarser and conglomeratic terrace, the samples AM-2A and AM-2B are homogeneous with medium grained matrix, and AM-2C and AM-2D exhibit fine-grained matrix with abundant detrital grains (∅ 1-25 mm) of shale and quartz. In the conglomeratic samples with fine-grained matrix at Nerva, hematite appeared as single phase (NV-1A) or coexisted with goethite (NV-1, NV-1B), whereas in the fine-grained, homogeneous samples from La Naya (LY-2A to 2D) goethite was the major phase. These minerals presented granular or botryoidal texture, appeared filling pore spaces or covering the detrital grains, mainly composed of shale and quartz, and they also appeared replacing minerals in the shale rock fragments (Fig. 5a-f). The grain size of the detrital material ranging from < 1mm to 25 mm depended on the location in the riverbed, and the grain size of the matrix composed of Fe phases varied from fine to medium. (Pérez-López et al., 2011) Pérez-López et al. (2011) observed that the crystallinity and grain size of goethite influence on the diagenetic transformation of goethite into hematite, and these authors observed the grain size-induced mineralogical variation according to layering within one sample of ancient terrace. The transformation process into hematite is promoted when goethite presents low crystallinity and small grain size, whereas precursor goethite with larger grain size tends to recrystallize without phase transformation (Langmuir, 1971). The samples AM-2C and NV-1A corroborate this observation.

The XRD pattern and Raman spectra collected for sample AM-2A are presented in Figures 4e and 6, respectively. Additionally, the XRD pattern for NV-1 is shown in Figure 4f. Both 4e and f exhibit goethite, hematite, and quartz. The Raman spectra for goethite were very similar to the ones from the recent terrace samples with nearly identical Raman shifts (Fig. 6A). Yet, goethite in AM-2A exhibited sharper Raman peaks, most probably, due to the higher

crystallinity of the ancient samples implying the recrystallization of goethite in diagenetic process. The well-defined bands of hematite (Fig. 6B) were in accordance with the data published by (Müller et al., 2010) Müller et al. (2010).

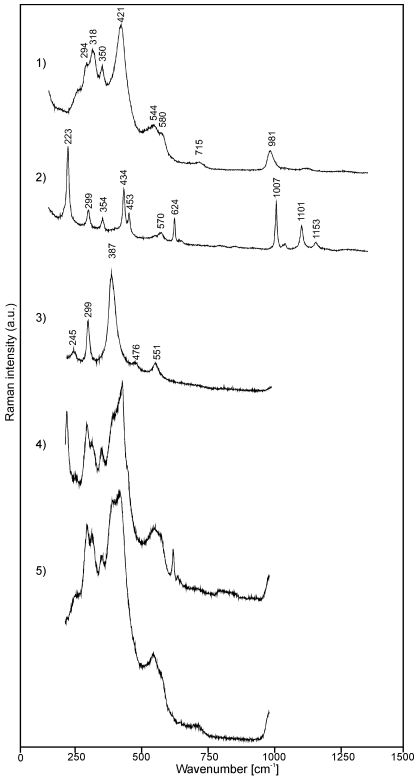

Figure 2.3: *Raman spectra of A) schwertmannite, B) jarosite, C) goethite, D) a mixture of schwertmannite and jarosite, and E) a mixture of schwertmannite and goethite in sample LN-2. The corresponding mineral distribution in the thin section is shown in Fig. 2d.*

The observations by SEM, EMPA and pseudo-total digestions exhibited traces of As, Co, Cu, Pb, and Zn in the ancient sediment samples indicating that traces of these elements remain in the ancient terraces after phase transformations (Table 3). The point analysis by EMPA showed only slightly higher average concentrations of As in goethite than in hematite in AM-2A, NV-1 and LY-2C (Table 3).

2.3.3 Arsenic mobility in the transformation process

Previous studies on natural and synthetic schwertmannite, jarosite, goethite, and hematite have demonstrated that these phases are good sorbents of As(V) at the pH range of the studied rivers affected by AMD (Acero et al., 2006; Asta et al., 2009; Fukushi et al., 2004;

Gimenez et al., 2007; Mamindy-Pajany et al., 2011). However, schwertmannite has proven the most efficient sorbent, and (Asta et al., 2010) Asta et al. (2009) suggest the net release of As(V) during the schwertmannite transformation because the sorption capacities of goethite and jarosite are considerably lower than the ones reported for schwertmannite (Fukushi et al., 2004, 2003). However, the laboratory experiments by (Acero et al., 2006) Acero et al. (2006) suggested that the As concentration in the solution slightly increased during the transformation process along the experiment, but after almost one year more than 99% of As remained in solid phase. This would explain why a clear trend in As concentrations was not observed between the phases in the newly-formed terrace samples. Pérez-López et al. (2011) concluded also that the current terraces do not involve spatial variations in arsenic total concentrations.

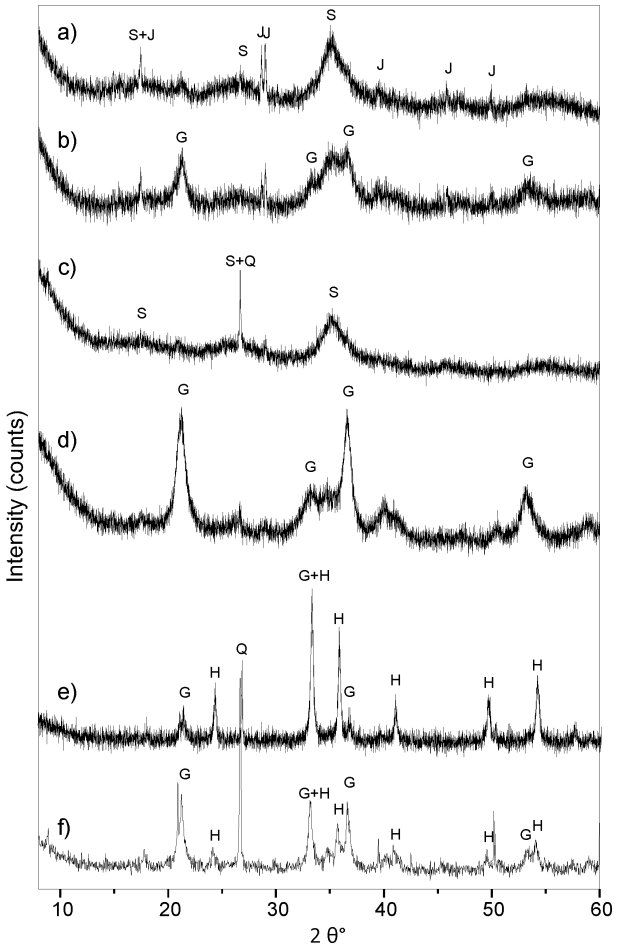

Figure 2.4: *XRD patters of a) and b) LN-1 (top and bottom layer, respectively), c) and d) TSR (top and bottom layer, respectively), e) AM-2A, and f) NV-1. Diffractograms were shifted for clarity purposes.*

Sample	[Bulk As] mg/kg	[Bulk Co] mg/kg	[Bulk Cu] mg/kg	[Bulk Pb] mg/kg	[Bulk Zn] mg/kg	[Max. As] mg/kg	Mineral Phase
LN-1	197	13.6	587	154	687	910	sw
						1570	go
						30	ja
						540	average*
LN-2	888	3.61	156	198	3.73	1520	sw
						1240	go
						950	average*
TSR	515	5.96	1046	705	290	34550	sw
						9810	go
						14290	average*
PER	1430	0.83	130	23	43.3	330	sw
						560	go
						370	average*
AM-2A	632	0.49	190	707	0.95	2530	go
						2080	hm
						2330	average*
NV-1	2338	0.88	1147	298	2.37	6030	go
						3910	hm
						5370	average*
LY-2C	N.A.	N.A.	N.A.	N.A.	N.A.	300	go
						100	Hm
						270	average*

Table 2.3: *Average bulk concentrations of As, Cu, Co, Pb, and Zn according to pseudo-total digestions and maximum As concentrations of each mineral phase measured by EMPA. (* = average concentration of all analysis points in the respective sample; N.A. = not analyzed).*

Even though not completely clear from the literature, the recrystallization of goethite or its diagenetic transformation into hematite in the long run is expected to reduce the retained As concentrations as the more crystallized phases can include less As in their structure and adsorb less on their surface upon crystal growth. Langmuir (1971) found that hematite coexisting with goethite presented lager particle size, which would imply smaller specific surface area and, therefore, reduced adsorption capacity of As. On the contrary, previous studies on both synthetic and natural samples have reported on higher As(V) sorption capacity in hematite than in goethite over a large pH range (especially at acid pH) (Gimenez et al., 2007; Mamindy-Pajany et al., 2011). Accordingly, transformation of goethite to hematite would not decrease the affinity of the sorbed phase for As(V). However, considering the influence of the particle size the lower As concentrations observed by EMPA in hematite in comparison to goethite in the ancient samples can be explained.

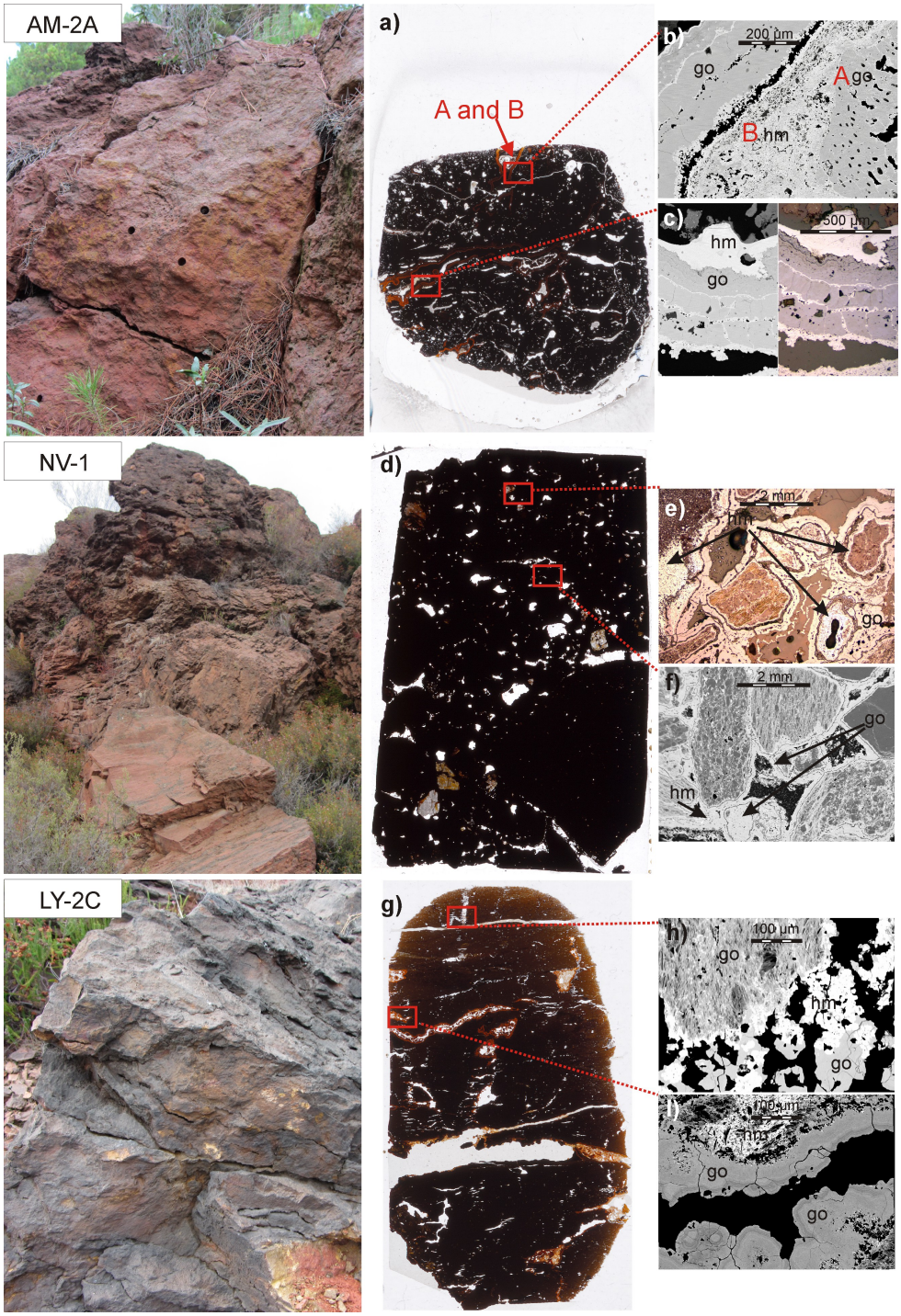

Figure 2.5: *Field, microscope, and back-scattered images of ancient Fe terraces (go = goethite; hm = hematite). The analysis points of Raman spectra shown in the Fig. 6 (A-B) are indicated in the thin section (a).*

Nonetheless, the EMPA and pseudo-total digestions of the ancient terraces of Tinto River exhibited relatively elevated concentrations of As, and in some cases they presented even higher values than in the newly-formed terraces currently under the influence of AMD. As it is impossible to speculate the water chemistry of Tinto River at the time of formation of the ancient terraces and the amount of As adsorbed in the initial schwertmannite precursor to goethite, we cannot estimate the net loss/gain of adsorbed As during the long-term mineral transformation. In addition to the As concentrations carried through the phase transformations, the goethite and hematite may have incorporated As by surface adsorption after the transformation process. Even though, it is clear from the previous laboratory studies that As is liberated during the phase transformations, this study demonstrates that the ancient terraces still retain a good portion of the As. This is an implication that, in the close proximity to sulfide oxidation profiles, ARD severely lowered the water quality long before anthropogenic influence of mining activity on the Tinto River area.

The liberation of As should be taken into account when designing models describing the long-term fate, transport, and bioavailability of As in environmental systems. However, more laboratory studies are required specifically to study and quantify the As loss during the long-term transformation process from initial schwertmannite to hematite. Additionally, more detailed studies on the structure of As are required to better describe how As is retained in the mineral phases: incorporated in the mineral structure or surface adsorption. For instance, this will help the discussion of the retention of As whether it is carried along the phase transformation or is it surface adsorbed afterwards onto the end-phase hematite, which generally shows good adsorption capacity (Gimenez et al., 2007; Mamindy-Pajany et al., 2011).

2.3.4 Raman identification in As-bearing Fe phases

The identification of Fe oxyhydroxides and oxyhydroxysulfates, with hydrous and poorly crystalline or pseudo-amorphous character, is challenging at best by conventional techniques such as XRD, SEM-EDX, and EMPA. When present in multimineral assemblages, the weak diffraction peaks of schwertmannite are often masked by the peaks of the other more crystalline phases. Additionally, the bulk powder XRD analysis cannot distinguish between *in situ* precipitated phases and detrital material dragged by the river flow. Furthermore, the unequivocal identification of these phases by microanalysis is effortful.

Raman spectroscopy proved as an efficient technique in the identification of the Fe phases at micro to millimeter scale allowing deduce the transformation tendencies and the mineralogical relationships of the different Fe phases in the layered structure of the newly-formed Fe terraces and also in the ancient sediments. The Raman allowed identifying monomineralic phases and also mixtures of minerals that was not possible to detect by XRD or microanalysis, also reported by (Murad, 1997) Murad (1997). The variation in crystallinity was also identified using Raman spectroscopy with sharper bands corresponding to the well-crystalline goethite in ancient terrace samples in comparison to goethite in the newly-formed samples (Figs. 3C and 6A). The full width of half maximum of the Raman shift at 300 cm^{-1} is smaller in the Fig. 6A (5.10) than in 3C (5.95). Furthermore, (Courtin-Nomade et al., 2009) Courtin-Nomade et al. (2009) found the same trend between poorly or microcrystalline and well-crystallized goethite. The well-defined XRD diffractograms of goethite with less background noise in the ancient terrace samples in comparison to newly-formed goethite also corroborate the better crystallinity of goethite in the ancient samples (Figs. 4b and f).

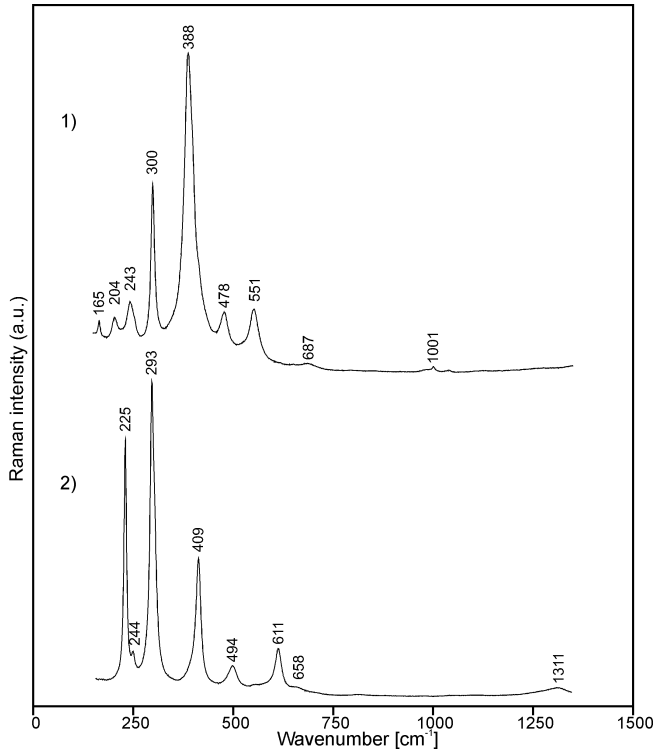

Figure 2.6: *Raman spectra of A) goethite and B) hematite in sample AM-2A (See Figs. 5a and b).*

However, the Raman identification of these phases requires finding the optimum conditions for analysis to avoid fluorescence and sample degradation, which occur frequently in hydrous mineral phases rich in Fe. Various attempts were made until obtaining good spectra, and the optimum conditions varied depending on the sample type (i.e. polished thin section vs. ground sample). The ground samples were more sensitive to the laser beam than polished thin sections.

Previous studies have shown that adsorption of As(V) on Fe phases can be detected by Raman as a spectral change in the As(V)-O stretching band (Burton et al., 2009; Müller et al., 2010). Burton et al. (2009) reported that Raman spectra could distinguish pure schwertmannite from the phases with adsorbed As. The Raman spectrum for As(V)-adsorbed schwertmannite shows a distinct As(V)-O stretching band at approx. 850 cm^{-1}. These authors attributed the As(V) adsorption to a significant SO_4^{2-} release, which was also detected by the diminishing intensity of S-O band at 981 cm^{-1}, and they interpreted it as As(V) sorption via incorporation into the mineral structure. This band corresponds to $\nu 1$ (SO_4^{2-}) (Mazetti and Thistletwaite, 2002).

On the contrary, pure goethite has nearly identical spectral data in comparison to the respective As(V)-loaded samples (Courtin-Nomade et al., 2003; Müller et al., 2010). According to Müller et al. (2010), the As(V)-loaded hematite exhibited merely a slight difference at about 866 cm^{1-}, which may be a result of the small amount of adsorbed As and consequently low resolution of the As related bands in the spectra.

In the newly-formed samples of Tinto and Odiel River Basins, As concentrations ranged from 330 to 34550 mg/kg in schwertmannite and from 30 to 1200 mg/kg in jarosite. However, the As(V)-O stretching band could not be detected possibly due to low resolution of the peak because of the low As concentration in comparison to the amount of adsorbed As (from 221 to 328 mmol As mol Fe^{-1}) in the experiments reported by Burton et al. (2009). Furthermore, the diminishing intensity of the S-O band due to SO_4^{2-} loss was not evident. The goethite and hematite spectra collected from the ancient sediment samples (with average 2600 mg/kg of As) did not show any changes either. Nevertheless, the Raman is recommended in the study of Fe(III) oxides, oxyhydroxides and oxyhydroxysulfates because it is easy and quick to run and because of the simplicity of the sample preparation.

REFERENCES

Acero, P., Ayora, C., Torrentó, C., Nieto, J.M., 2006. The behavior of trace elements during schwertmannite precipitation and subsequent transformation into goethite and jarosite. Geochim. Cosmochim. Acta 70, 4130–4139. doi:10.1016/j.gca.2006.06.1367

Asta, M.P., Ayora, C., Román-Ross, G., Cama, J., Acero, P., Gault, A.G., Charnock, J.M., Bardelli, F., 2010. Natural attenuation of arsenic in the Tinto Santa Rosa acid stream (Iberian Pyritic Belt, SW Spain): The role of iron precipitates. Chem. Geol. 271, 1–12. doi:10.1016/j.chemgeo.2009.12.005

Asta, M.P., Cama, J., Martínez, M., Giménez, J., 2009. Arsenic removal by goethite and jarosite in acidic conditions and its environmental implications. J. Hazard. Mater. 171, 965–972. doi:10.1016/j.jhazmat.2009.06.097

Bigham, J.M., Schwertmann, U., Traina, S.J., Winland, R.L., Wolf, M., 1996. Schwertmannite and the chemical modeling of iron in acid sulfate waters. Geochim. Cosmochim. Acta 60, 2111–2121. doi:10.1016/0016-7037(96)00091-9

Burton, E.D., Bush, R.T., Johnston, S.G., Watling, K.M., Hocking, R.K., Sullivan, L. a., Parker, G.K., 2009. Sorption of Arsenic(V) and Arsenic(III) to schwertmannite. Environ. Sci. Technol. 43, 9202–9207. doi:10.1021/es902461x

Courtin-Nomade, A., Bril, H., Neel, C., Lenain, J.-F., 2003. Arsenic in iron cements developed within tailings of a former metalliferous mine—Enguialès, Aveyron, France. Appl. Geochemistry 18, 395–408. doi:10.1016/S0883-2927(02)00098-7

Courtin-Nomade, A., Grosbois, C., Marcus, M.A., Fakra, S.C., Beny, J.-M., Foster, A.L., 2009. The weathering of a sulfide orebody: Speciation and fate of some potential contaminants. Can. Mineral. 47, 493–508. doi:10.3749/canmin.47.3.493

Das, R.S., Agrawal, Y.K., 2011. Raman spectroscopy: Recent advancements, techniques and applications. Vib. Spectrosc. 57, 163–176. doi:10.1016/j.vibspec.2011.08.003

Das, S., Hendry, M.J., 2011. Application of Raman spectroscopy to identify iron minerals commonly found in mine wastes. Chem. Geol. 290, 101–108. doi:10.1016/j.chemgeo.2011.09.001

Egal, M., Elbaz-Poulichet, F., Casiot, C., Motelica-Heino, M., Négrel, P., Bruneel, O., Sarmiento,

A.M., Nieto, J.M., 2008. Iron isotopes in acid mine waters and iron-rich solids from the Tinto-Odiel Basin (Iberian Pyrite Belt, Southwest Spain). Chem. Geol. 253, 162–171. doi:10.1016/j.chemgeo.2008.05.006

Essalhi, M., Sizaret, S., Barbanson, L., Chen, Y., Lagroix, F., Demory, F., Nieto, J.M., Sáez, R., Capitán, M.Á., 2011. A case study of the internal structures of gossans and weathering processes in the Iberian Pyrite Belt using magnetic fabrics and paleomagnetic dating. Miner. Depos. 46, 981–999. doi:10.1007/s00126-011-0361-8

Fernández-Remolar, D.C., Morris, R. V., Gruener, J.E., Amils, R., Knoll, A.H., 2005. The Río Tinto Basin, Spain: Mineralogy, sedimentary geobiology, and implications for interpretation of outcrop rocks at Meridiani Planum, Mars. Earth Planet. Sci. Lett. 240, 149–167. doi:10.1016/j.epsl.2005.09.043

Filippi, M., Doušová, B., Machovič, V., 2007. Mineralogical speciation of arsenic in soils above the Mokrsko-west gold deposit, Czech Republic. Geoderma 139, 154–170. doi:10.1016/j.geoderma.2007.01.015

Froment, F., Tournié, A., Colomban, P., 2008. Raman identification of natural red to yellow pigments: ochre and iron-containing ores. J. Raman Spectrosc. 39, 560–568.

Frost, R.L., Wills, R.A., Weier, M.L., Martens, W., 2005. Comparison of the Raman spectra of natural and synthetic K- and Na-jarosites at 298 and 77 K. J. Raman Spectrosc. 36, 435–444. doi:10.1002/jrs.1317

Fukushi, K., Sato, T., Yanase, N., 2003. Solid-solution reactions in As(V) sorption by schwertmannite. Environ. Sci. Technol. 37, 3581–3586. doi:10.1021/es026427i

Fukushi, K., Sato, T., Yanase, N., Minato, J., Yamada, H., 2004. Arsenate sorption on schwertmannite. Am. Mineral. 89, 1728–1734.

Gimenez, J., Martinez, M., de Pablo, J., Rovira, M., Duro, L., 2007. Arsenic sorption onto natural hematite, magnetite, and goethite. J. Hazard. Mater. 141, 575–580. doi:10.1016/j.jhazmat.2006.07.020

Hubbard, C.G., Black, S., Coleman, M.L., 2009. Aqueous geochemistry and oxygen isotope compositions of acid mine drainage from the Río Tinto, SW Spain, highlight inconsistencies in current models. Chem. Geol. 265, 321–334. doi:10.1016/j.chemgeo.2009.04.009

Langmuir, D., 1971. Particle size effect on the reaction goethite = hematite + water.pdf. Am. J. Sci.

Leistel, J.M., Marcoux, E., Thiéblemont, D., Quesada, C., Sânchez, A., Almódovar, G.R., Pascual, E., Sáez, R., 1998. The volcanic-hosted massive sulphide deposits of the Iberian Pyrite Belt: Review and preface to the Thematic Issue. Miner. Depos. 33, 2–30.

Mamindy-Pajany, Y., Hurel, C., Marmier, N., Roméo, M., 2011. Arsenic (V) adsorption from aqueous solution onto goethite, hematite, magnetite and zero-valent iron: Effects of pH, concentration and reversibility. Desalination 281, 93–99. doi:10.1016/j.desal.2011.07.046

Mazzetti, L., Thistlethwaite, P.J., 2002. Raman spectra and thermal transformations of ferrihydrite and schwertmannite. J. Raman Spectrosc. 33, 104–111. doi:10.1002/jrs.830

Müller, K., Ciminelli, V.S.T., Dantas, M.S.S., Willscher, S., 2010. A comparative study of As(III) and As(V) in aqueous solutions and adsorbed on iron oxy-hydroxides by Raman spectroscopy. Water Res. 44, 5660–5672. doi:10.1016/j.watres.2010.05.053

Murad, E., 1997. Identification of minor amounts of anatase in kaolins by Raman spectroscopy. Am. Mineral. 82, 203–206.

Nieto, J.-M., Sarmiento, A.M., Cánovas, C.R., Olías, M., Ayora, C., 2013. Acid mine drainage in the Iberian Pyrite Belt: 1. Hydrochemical characteristics and pollutant load of the Tinto and Odiel Rivers. Environ. Sci. Pollut. Res. Int. 20, 7509–7519. doi:10.1007/s11356-013-1634-9

Nieto, J.M., Sarmiento, A.M., Canovas, C.R., Olias, M., Ayora, C., 2013. Acid mine drainage in the Iberian Pyrite Belt: 1. Hydrochemical characteristics and pollutant load of the Tinto and Odiel rivers. Environ. Sci. Pollut. Res. 20, 7509–7519. doi:10.1007/s11356-013-1634-9

Nieto, J.M., Sarmiento, A.M., Olúas, M., Canovas, C.R., Riba, I., Kalman, J., Delvalls, T.A., 2007. Acid mine drainage pollution in the Tinto and Odiel rivers (Iberian Pyrite Belt, SW Spain) and bioavailability of the transported metals to the Huelva Estuary. Environ. Int. 33, 445–455. doi:10.1016/j.envint.2006.11.010

Nocete, F., Sáez, R., Bayona, M.R., Nieto, J.M., Peramo, A., López, P., Gil-Ibarguchi, J.I., Inácio, N., García, S., Rodríguez, J., 2014. Gold in the Southwest of the Iberian Peninsula during the 3rd Millennium BC. J. Archaeol. Sci. 41, 691–704. doi:10.1016/j.jas.2013.10.006

Pérez-López, R., Asta, M.P., Román-Ross, G., Nieto, J.M., Ayora, C., Tucoulou, R., 2011. Synchrotron-based X-ray study of iron oxide transformations in terraces from the Tinto-Odiel river system: Influence on arsenic mobility. Chem. Geol. 280, 336–343. doi:10.1016/j.chemgeo.2010.11.021

Sáez, R., Pascual, E., Toscano, M., Almodóvar, G.R., 1999. The Iberian type of volcano-sedimentary massive sulphide deposits. Miner. Depos. 34, 549–570. doi:10.1007/s001260050220

Sarmiento, A.M., Nieto, J.-M., Casiot, C., Elbaz-Poulichet, F., Egal, M., 2009. Inorganic arsenic speciation at river basin scales: The Tinto and Odiel Rivers in the Iberian Pyrite Belt, SW Spain. Environ. Pollut. 157, 1202–1209. doi:10.1016/j.envpol.2008.12.002

Tornos, F., 2006. Environment of formation and styles of volcanogenic massive sulfides: The Iberian Pyrite Belt. Ore Geol. Rev. 28, 259–307. doi:10.1016/j.oregeorev.2004.12.005

CHAPTER III

TRACE ELEMENT-MINERAL ASSOCIATIONS IN MODERN AND ANCIENT IRON TERRACES IN ACID DRAINAGE ENVIRONMENT

BASED ON:

CRUZ-HERNÁNDEZ, P., PÉREZ-LÓPEZ, R., PARVIAINEN, A., LINDSAY, M.B.J., NIETO, J.M., 2016. TRACE ELEMENT-MINERAL ASSOCIATIONS IN MODERN AND ANCIENT IRON TERRACES IN ACID DRAINAGE ENVIRONMENTS. **CATENA** 147, 386–393. DOI:10.1016/J.CATENA.2016.07.049

TRACE ELEMENT-MINERAL ASSOCIATIONS IN MODERN AND ANCIENT IRON TERRACES IN ACID DRAINAGE ENVIRONMENT

Iron-rich sediments commonly cover riverbeds that have been affected by acid drainage associated with sulfide-mineral oxidation. Freshly-formed precipitates correspond to poorly-crystalline oxyhydroxysulfates that recrystallizes over time. This study examined the distribution and mineral association of trace elements (e.g., As, Cu, Zn) in modern and ancient (~6 Ma) Fe terraces in the Tinto river basin, Spain. The mineral composition of the terraces was determined by Raman μ-spectroscopy. Chemical digestions, electron probe microanalyses, and synchrotron-based μ-X-ray fluorescence mapping were used to examine As, Cu, and Zn distribution and corresponding mineral associations. Fresh precipitates at modern terrace surfaces were dominated by schwertmannite, which contained high As, Cu, Mn, and Zn concentrations. However, schwertmannite transforms into goethite at short-time in the deeper part of the current terraces and into hematite at century-time scale. This mineral transformation involves a statistically significant loss of Fe phases affinity by previously-removed trace elements that progressively increases with the phase crystallinity. Hence, schwertmannite acts as temporary sink for contaminants, which are again released at long-term during the maturation. These findings should be considered for management and treatment of possible water resources affected by acid mine drainage.

3.1 Introduction

The natural weathering of outcropping sulfide ore bodies under meteoric conditions often produces acid rock drainage (ARD). Oxidative dissolution of sulfide minerals can lead to widespread acidification and contamination of water resources. Acid mine drainage (AMD) is generated where sulfide-mineral oxidation is accelerated, such as in mining operations that include excavations, earth works, and waste deposits. The consequences of AMD are generally more severe than ARD because mining activities increase exposed surface area of sulfide-bearing rocks (Amos et al., 2015; Lindsay et al., 2015; Olías et al., 2004; Webster et al., 1998). Dissolution of pyrite [FeS_2] and other sulfides in the presence of oxygen and water releases Fe(II) and SO_4, and generates protons causing acidification of waters. Potentially hazardous trace elements (e.g., As, Cu, Zn) associated to sulfides are also liberated during oxidative dissolution. Subsequent oxidation of Fe(II) can promote spontaneous precipitation of Fe(III) oxyhydroxides and oxyhydroxysulfates from acid-sulfate waters. These waters host extremophile bacterial species such as *Thiobacillus ferrooxidans* and *Leptospirillum ferrooxidans* that catalyze Fe(II) oxidation and accelerate subsequent precipitation reactions (Boon and Heijnen, 1998; Leduc et al., 2002).

Schwertmannite [$Fe_{16}O_{16}(OH)_{12}(SO_4)_2$] is thought to initially be the most thermodynamically stable phase in AMD impacted waters (Bigham et al., 1996). This poorly-crystalline oxyhydroxysulfate phase has a high capacity to sequester As and other potentially hazardous trace elements (Fernandez-Martinez et al., 2010; Fukushi et al., 2003, 2004). However, schwertmannite is metastable and tends to transform into more crystalline phases such as goethite [$FeO(OH)$] and jarosite [$KFe_3(SO_4)_2(OH)_6$] within weeks (Acero et al., 2006; Davidson et al., 2008). Goethite can subsequently transform into hematite [Fe_2O_3] over the long term through diagenetic processes (Davidson et al., 2008; Langmuir, 1971).

Formation of Fe terraces within AMD impacted rivers begins with accumulation and consolidation of schwertmannite on riverbeds (Cáceres et al., 2013). Transformation of schwertmannite into goethite, jarosite, and hematite has previously been observed in Fe terraces within AMD-impacted rivers (Asta et al., 2010; Parviainen et al., 2015; Pérez-López et al., 2011). Several laboratory studies have also examined the behavior of As and other trace elements during these transformations; however, the potential for trace element removal or release during these transformations remains unclear. Whereas some studies claim that As sorption capacity increases with crystallinity, particularly at low pH (Gimenez et al., 2007;

Mamindy-Pajany et al., 2011a), others indicate that As is preferentially retained in less crystalline phases (Bowell, 1994). In addition, relatively few studies have examined trace element behavior during mineral transformations in Fe terraces in field settings (Acero et al., 2006; Pérez-López et al., 2011). Moreover, the research reported shows new insights in different trace elements behavior and uses more precise techniques. Such conflicting results or simple lack of information is also the case for other trace elements. Thus, the main objective of this study was to examine the distribution of trace elements in Fe terraces to assess their potential long-term fate during schwertmannite transformation under natural conditions. Samples from two distinct terraces in the Tinto River basin in SW Spain were collected: one from a newly-formed modern terrace in an AMD-impacted river and one from an ancient Fe terrace away from the modern river channel. These ancient terraces were formed under similar conditions as the currently-formed terraces and were isolated due to the river migration over time (Amils et al., 2007; Fernández-Remolar, 2003).

3.2 Materials and Methods

3.2.1 Site description

The Iberian Pyrite Belt (IPB) is one of the largest massive sulfide provinces in the world, with original massive sulfide reserves estimated at more than 1,700 Mt (Sáez et al., 1999). The IPB spans approximately 20,000 km^2 and hosts more than 100 mines, the majority of which are currently inactive. Mining activity on the IPB began approximately 4,500 years ago (Nocete et al., 2014). Consequently, vast amounts of tailings and waste rock, and numerous open pits and underground workings, have exposed sulfide minerals to oxidative weathering and produced intense AMD. The legacy of the mining operations has severely degraded water quality in local catchments, which ultimately discharge from the Tinto and Odiel Rivers into the Atlantic Ocean. Consequently, these rivers account for a significant percentage of the total toxic element input to oceans worldwide (J.-M. Nieto et al., 2013; Olías et al., 2016). Ore deposits are mainly comprised of Fe-rich sulfides such as pyrite [FeS_2], pyrrhotite [$Fe_{(1-x)}S$], chalcopyrite [$CuFeS_2$], and arsenopyrite [$FeAsS$], plus other metalliferous minerals including sphalerite [ZnS] and galena [PbS]. The most intensive mining in the area left several abandoned open pits, including Cerro Colorado, Peña del Hierro, and Corta Atalaya (Fig. 1a).

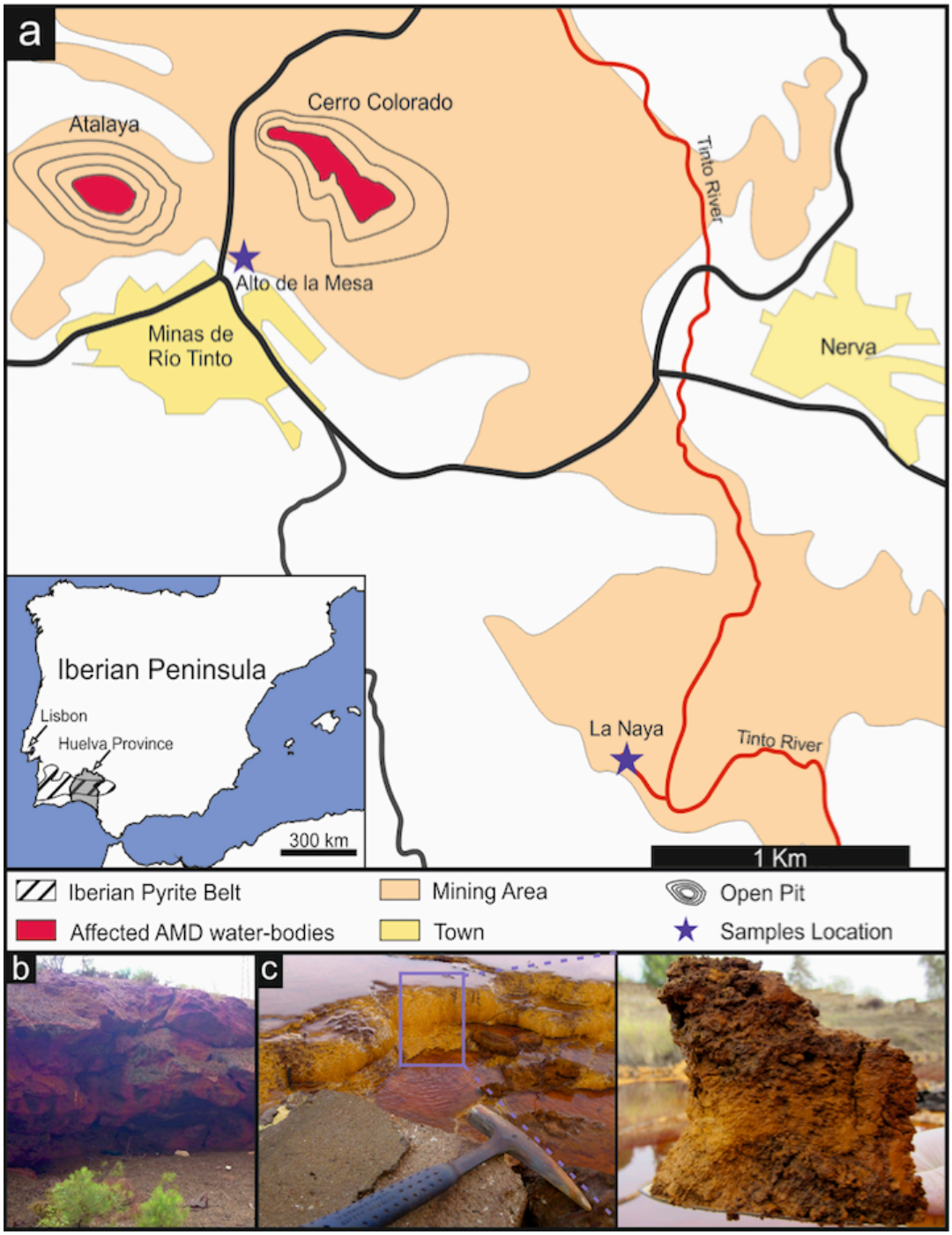

***Fig. 3.1**: Detailed map of the study area showing: (a) sampling locations, (b) an image of the Alto de la Mesa ancient terrace outcrop, and (c) images of the newly-formed La Naya terrace.*

3.2.2 Sample collection and preparation

The river basins in the study area feature actively-forming modern terraces in AMD-affected rivers and ancient terraces that formed under similar conditions as the modern terraces but were isolated due to river migration over time (Amils et al., 2007; Fernández-Remolar, 2003). The age of the terraces denotes the maturation degree of the Fe phases. Thus, representative samples of the different stages of maturation were collected at El Alto de la Mesa (ancient terrace) and La Naya (modern terrace). The El Alto de la Mesa sample was collected from an ancient terrace consisting of an accumulation of Fe-oxides approximately 60 m above the modern riverbed (Fig. 1a,b). Stratigraphically, this terrace is defined as a fluvial point-bar sequence of around 6 Ma (Messinian age) (Essalhi et al., 2011). The modern terrace sample was collected from a freshly-formed terrace in a tributary of the Tinto River in the inactive Zarandas-La Naya mining area (Fig. 1a,c). The sample thickness was approximately 10 cm, which represented the most recent sedimentation sequence.

In the laboratory, the fresh terrace sample was dried at room temperature in the presence of a desiccant to avoid any mineralogical transformations. Subsamples of interest from both terraces were selected, ground using an agate mortar and pestle, and subjected to conventional geochemical and mineralogical analysis. In addition, undisturbed samples from both terraces were prepared as polished thin sections; these were embedded in polyester epoxy, mounted on quartz glass slides using polyester resin, and polished to a final thickness of approximately 50 μm. All polishing was performed without water to avoid dissolution of water-soluble phases.

3.2.3 Geochemical and mineralogical analyses

The modern terraces are earthy and porous in nature, which limits the use of point techniques for quantitative chemical microanalysis (Cáceres et al., 2013). Thus, subsamples for detailed geochemical analyses were taken corresponding to color changes with depth. In contrast, bulk chemical analyses of the ancient terrace were conducted because separation was not possible. Subsamples of the modern terrace along with bulk ancient terrace samples (2 replicates per sample) were digested in aqua regia prepared using a 1:3 molar ratio of HNO_3 to HCl and heated at 90 °C to pseudo-dry the solution. These samples were then re-dissolved in 50 mL of a 10% HNO_3 solution and analyzed for major and trace elements by inductively coupled plasma-optical emission spectrometry (ICP-OES, Thermo Jarrel-Ash) and inductively coupled plasma-mass spectrometry (ICP-MS, X-series II Thermo), respectively.

An optical microscope (Nikon Eclipse LV100POL) operating in reflected light mode was used to examine mineralogical and textural characteristics of the samples in thin sections. Raman μ-spectroscopy can be used to identify Fe phases of varied crystallinity (e.g. Das and Hendry, 2011). Thus, Raman spectra were collected at the Instituto Andaluz de Ciencias de la Tierra (Granada, Spain) according to methods described in detail by (Parviainen et al., 2015). Briefly, the Raman microscope (LabRAM HR, Jobin-Yvon Horiba, Japan) was operated in backscattering geometry with a 784 nm excitation beam focused using a confocal microscope (Olympus). Two to four replicate Raman spectra were collected using a Peltier-cooled charge coupled device (CCD) detector and 300 s acquisition time. Mineral transformations and sample degradation were minimized by using D0.3 and D0.6 filters. A resolution of 3 cm^{-1} and spectral range of 150 to 1,350 cm^{-1} were used.

Thin sections were also graphite coated and examined using an electron probe microanalyzer (EPMA) at the University of Huelva (Huelva, Spain). Unlike the modern terrace, the ancient sample is a hard mass of consolidated Fe phases that permits the use of point techniques for quantitative chemical microanalysis. Thus, imaging of both terraces and quantitative geochemical analysis of the ancient terrace sample were carried out with a four-spectrometer EPMA (JXA-8200 Superprobe, JEOL Ltd., Japan) using a 5 μm beam and 15 KeV acceleration voltage. Metallic oxides, sulfides, and silicates were used as standards. Numerous analyses (n = 100) were performed on areas identified by optical microscopy and Raman μ-spectroscopy.

3.2.4 Micro-X-ray fluorescence mapping

Synchrotron-based μ-X-ray fluorescence (μ-XRF) mapping of sample thin sections was performed to examine the distribution of the main AMD-related elements (e.g., As, Cu, Zn) and to identify the association of these elements with the Fe mineral phases. Target areas were selected based on the mineralogical examination, and graphite coatings were removed prior to analysis. The μ-XRF maps were obtained on the GeoSoilEnviroCARS beamline 13-ID-E at the Advanced Photon Source (Chicago, USA). The storage ring was operated in continuous top-up mode at a current of approximately 102 mA during mapping. The cryo-cooled monochrometer setup used two Si(111) crystals to select an incident X-ray energy of 30 keV. The micro-focused X-ray beam had a spot size of 2 × 2 μm and the samples were rastered using a 2-μm step size and a 50-ms dwell time. A four-element silicon drift detector (Vortex®-ME4, Hitatchi High Technologies America, Inc.) was used to obtain fluorescence spectra; three layers of Al

foil were placed over the detector to filter a portion of the Fe signal and avoid detector saturation. Processing and analysis of μ-XRF data were done using Larch (Newville, 2001) and PyMCA (Solé et al., 2007) software packages. Moreover, principal component analysis (PCA) was performed with XLSTAT-Pro v7.5.2 to reduce the μ-XRF data in the different mineralogical zones of each terrace. Pearson correlation was used as an index of similarity and *p*-values were fixed at 0.05. The two first principal components (PC1 and PC2) were considered the most informative and simplest way to display the PCA results.

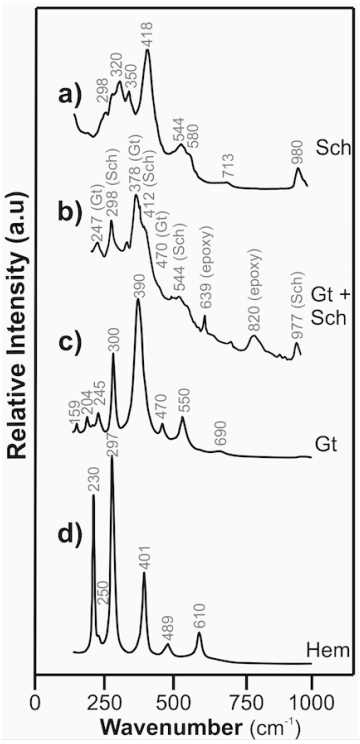

***Fig. 3.2**: Representative micro-Raman spectra of (a) schwertmannite and (b) a mixture of schwertmannite and goethite in the newly-formed terrace sample, and (c) goethite and (d) hematite in the ancient terrace sample.*

3.3 Results

3.3.1 Modern terraces

The upper part of the newly-formed modern terrace was exclusively dominated by schwertmannite from surface to a depth of 0.5 to 1 cm. The relative proportion of goethite then progressively increased with depth. Raman spectra obtained from the upper part of this sample exhibit characteristic schwertmannite bands at 298, 320, 350, 418, 544, 580, 713, and 980 cm^{-1} (Fig. 2a; Burton et al., 2009; Mazzetti and Thistlethwaite, 2002; Parviainen et al., 2015). Characteristic bands for goethite at 247, 378, and 470 cm^{-1} appear with increasing depth, while other bands at 298 and 544 cm^{-1} overlap with those of schwertmannite (Fig. 2b; Müller et al., 2010; Parviainen et al., 2015).

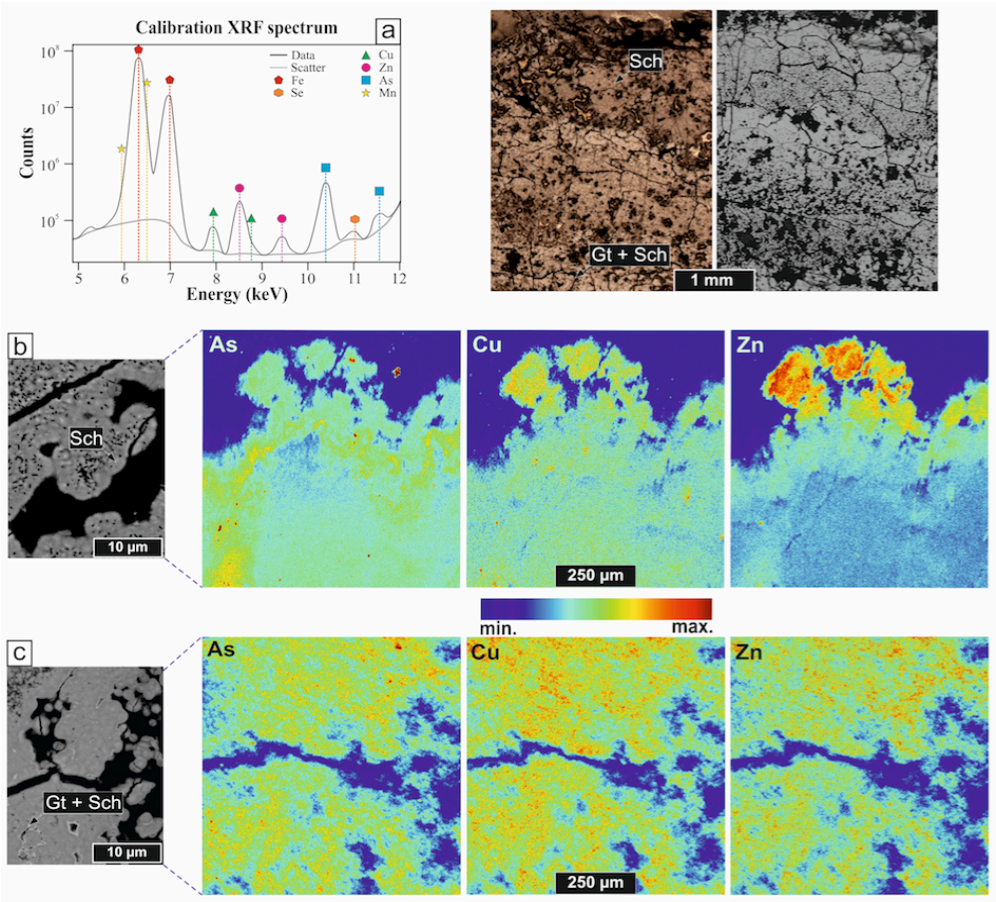

***Fig. 3.3**: Optical and EPMA images of the newly-formed terrace sample with the micro cross-sections analyzed by synchrotron-µ-XRF: (a) calibration spectrum fitted with PyMCA software and (b,c) elemental distribution maps. Two detailed EPMA images are shown for each micro-section. For interpretation of colors, the reader is*

referred to the web version of this paper.

A typical X-ray fluorescence spectrum is also shown in Figure 3a. Although schwertmannite and goethite cannot be clearly and individually recognized in the EPMA images, some textural differences along the samples are evident. Schwertmannite in the surface part occurs as porous spherical microaggregates (Fig. 3b), whereas the schwertmannite and goethite mixture observed in deeper layers appear less porous and exhibit a botryoidal texture typical of goethite (Fig. 3c). Jarosite is present as a minor phase in deeper layers of the newly-formed terrace.

	LN depth (cm)					
Sample	**0-1**	**1-2**	**2-4**	**4-7**	**7-11**	**AM**
	Major elements (%)					
Al_2O_3	0.30	0.28	0.17	0.15	0.19	0.41
CaO	0.120	0.096	0.066	0.058	0.061	0.017
Fe_2O_3	43.9	45.0	49.1	58.1	56.8	78.3
K_2O	0.29	0.52	0.57	1.63	2.10	bdl
MgO	0.47	0.44	0.22	0.16	0.22	0.004
MnO	0.036	0.035	0.019	0.015	0.019	0.001
Na_2O	0.013	0.019	0.014	0.026	0.18	0.19
SO_3	12.9	12.3	11.5	11.5	10.2	0.56
	Trace elements (mg kg^{-1})					
As	258	213	197	222	224	632
Co	4.31	3.26	2.75	4.10	3.32	0.49
Cu	7940	5270	4130	6560	6540	191
Ni	4.73	11.1	6.50	1.85	7.27	0.40
Pb	53.1	114	92.1	282	412	708
Se	3.09	1.79	3.78	2.73	3.08	4.69
Ti	2.37	5.02	7.60	8.12	14.7	66.6
V	16.6	7.16	16.7	17.8	15.5	201
Zn	1121	1031	598	537	631	2.37

bdl = below detection limit*

***Table 3.1**: Bulk concentrations in the terrace samples according to the pseudo-total digestions. Subsamples of the newly-formed terrace were taken from depth increments from the top (0-1 cm). LN = modern terrace sample and AM = ancient terrace sample.*

Mineralogical observations appear congruent with the chemical composition changes with depth based on the pseudo-total digestion results (Table 1). The progressive transformation of schwertmannite into goethite is reflected by a decrease in S (from 13 to 10

wt.% as SO_3) and an increase in Fe (from 44 to 57 wt.% as Fe_2O_3) concentrations in the solid. An increase in the K content with depth (from 0.3 to 2 wt.% as K_2O) can be attributed to the minor occurrence of jarosite. Concentrations of metals typical of AMD (e.g., As, Cu, Zn) are slightly elevated in the upmost part but do not show a specific trend with depth (Table 1). These findings are also in agreement with two µ-XRF maps performed on the newly-formed modern terrace, one for the upper schwertmannite section (Fig. 3b) and the other for the deeper schwertmannite and goethite section (Fig. 3c). The maps confirm that fluorescence intensities for As, Cu, and Zn are slightly higher in the first few micrometers of the uppermost micro-section that features fresher schwertmannite. However, spatial distribution of these elements in the remainder of the terrace sample is generally homogeneous across the micro-sections analyzed. Therefore, chemical composition does not appear to be substantially controlled by the mineralogical variation in these samples.

3.3.2 Ancient terraces

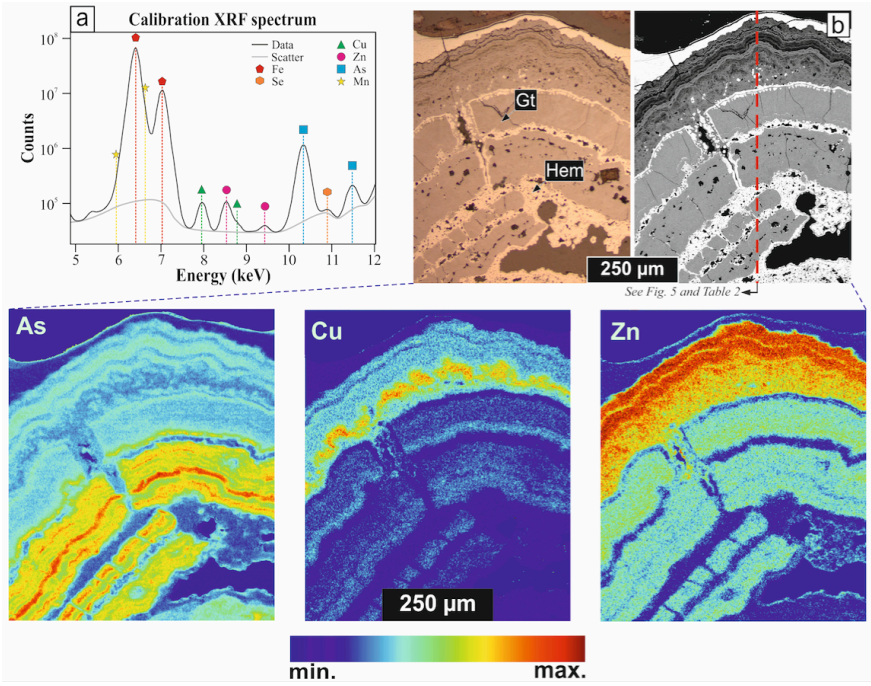

***Fig. 3.4**: Variation of the relative fluorescence intensity of As, Cu, and Zn along the ancient terrace. Hematite and goethite levels are differentiated (light grey = hematite; dark grey = goethite).*

The ancient terrace sample exhibits well-defined bands of individual hematite and goethite, but hematite is the main phase comprising the sample matrix. Raman micro-spectra

of the goethite bands exhibit peaks at 159, 204, 245, 300, 390, 470, 550, and 690 cm^{-1} (Fig. 2c). These peaks are much better defined than those for the ancient terrace sample, which is indicative of higher crystallinity of the goethite in the older terrace. Hematite peaks appear at 230, 250 (minor), 297, 401, 489, and 610 cm^{-1} (Fig. 2d; Das and Hendry, 2011; Müller et al., 2010; Parviainen et al., 2015). An X-ray fluorescence spectrum of a modern terrace sample is provided in Figure 4a. EPMA images reveal the presence of botryoidal and colloform textures where hematite appears to have largely replaced goethite as the dominant phase (Fig. 4b). Some detrital quartz grains are also evident.

The bulk chemical composition of the ancient terrace sample is dominated by Fe (78 wt.% as Fe_2O_3), as expected; S is a minor component (0.6 wt.% as SO_3; Table 1). The remainder is composed of Al, Na, As, Pb, and Cu, while Zn is almost undetectable (Table 1). Unlike the modern terrace, µ-XRF mapping reveals that elemental distribution within the ancient terrace sample is strongly linked to mineralogy. As, Cu, and Zn generally exhibit higher fluorescence intensities in areas featuring goethite bands than in those featuring hematite bands (Fig. 4b). Fluorescence intensity profiles for As, Cu, and Zn across the ancient terrace sample further illustrate the greater affinity of these elements for goethite vs. hematite (Fig. 5).

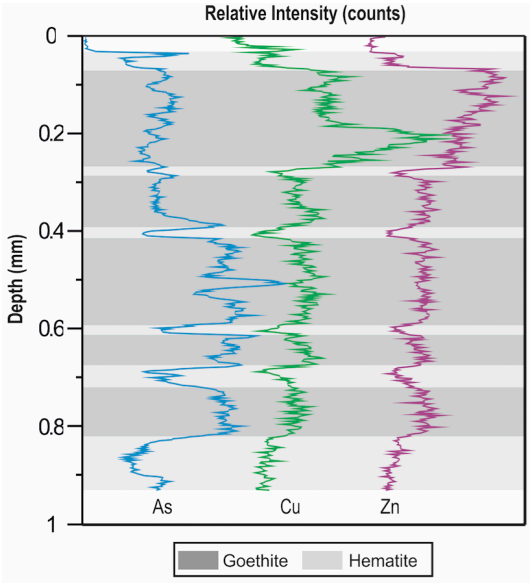

***Fig. 3.5**: Variation of the relative fluorescence intensity of As, Cu, and Zn along the ancient terrace. Hematite and goethite levels are differentiated (light grey = hematite; dark grey = goethite).*

In addition, EPMA analysis results throughout this micro-section are generally consistent with the trace element information from the μ-XRF map. Iron concentrations are slightly higher in areas featuring hematite (83 ± 0.75 wt.%; mean ± standard deviation) than those featuring goethite (73 ± 0.84 wt.%). However, S and trace elements concentrations are higher in the goethite bands (e.g., 1.2 ± 0.11 wt.% for S as SO_3; 3394 ± 1006 mg/kg for As; 1305 ± 414 mg/kg for Cu; 746 ± 237 mg/kg for Zn on average) than in the hematite bands (e.g., 0.58 ± 0.08 wt.% for S as SO_3; 2084 ± 393 mg/kg for As; values below or close to the detection limit for Cu and Zn) (Table 2). Although no fluorescence data for Pb are available, EPMA analyses show that Pb is the only trace element with consistently higher concentrations in hematite (2254 ± 315 mg/kg) than in goethite (1704 ± 569 mg/kg; Table 2). Notably, the As distribution is discordant with that of Cu and Zn within the goethite bands, i.e., higher As and lower Cu and Zn intensities, or vice versa (Fig. 5). The distribution of these heterogeneities, parallel to the formation of the different bands in the ancient sample, can be attributed to temporal changes in the initial composition.

depth (µm)	31-82	82-270	270-285	285-390	390-410	410-590	590-620	620-680	680-715	715-820	820-940
Mineralogy	***Hem***	***Gt***	***Hem***	***Gt***	***Hem***	***Gt***	***Hem***	***Gt***	***Hem***	***Gt***	***Hem***
	Major elements (%)										
SiO_2	0.91	1.00	1.02	1.07	0.93	1.03	1.00	0.85	0.93	0.80	0.94
Al_2O_3	0.39	2.15	0.22	0.47	0.16	0.84	0.35	0.95	0.10	0.83	0.17
Fe_2O_3	83.7	73.8	82.7	72.7	83.8	73.5	81.9	75.2	83.3	73.5	84.0
CaO	0.02	0.03	0.04	bdl	0.01	bdl	0.01	0.03	0.03	0.02	0.05
K_2O	0.03	0.02	0.01	0.02	0.01	0.02	0.01	0.02	0.01	0.02	0.01
SO_3	0.57	1.18	0.57	1.28	0.64	1.29	0.66	1.01	0.65	1.31	0.41
	Trace elements (mg kg^{-1})										
As	1692	2086	1884	2284	1917	4498	2653	4194	1754	3907	2608
Cu	bdl	1678	bdl	987	bdl	1039	bdl	1923	bdl	899	959
Pb	2409	928	2107	1105	2831	2228	2315	2234	1866	2027	2001
Zn	bdl	964	152	550	bdl	402	bdl	801	bdl	1015	bdl

bdl = below detection limit*

Table 3.2*: Electron microprobe analyses (n=100) of goethite (gt) and hematite (hm) levels in the ancient terrace. Depth intervals match those shown in Figure 5.*

3.4 Discussion

The geochemical and mineralogical composition of the terrace samples reflects the gradual maturation of poorly-crystalline early precipitates into more crystalline and stable phases, which aligns with previous studies (e.g., Acero et al., 2006; Pérez-López et al., 2011). The fresh AMD-precipitates are comprised of schwertmannite; however, analysis of still-unconsolidated sediments reveals that this poorly-crystalline Fe phase is transformed over the short term into goethite and occasionally jarosite. Over the long term, goethite recrystallizes and is replaced by hematite following textural evidences of replacement in the bands (Fig. 5). In Raman spectra, fresher goethite associated with modern terraces has less well-defined bands than the more crystalline goethite present in ancient terraces. Consistent with the mineralogical transformation, the bulk concentrations of Fe and S increase and decrease, respectively, with increasing crystallinity, i.e., from the schwertmannite-dominated newly-formed terrace to the hematite-dominated ancient terrace. Obviously, sulfate release occurs during the transformation from iron oxyhydroxysulfates to oxyhydroxides and oxides (Bigham et al., 1996).

Comparing absolute concentrations of trace elements in the ancient and modern terraces is meaningless because the chemistry of these elements in the AMD and, hence, in the precipitates varies strongly depending on the type of ore deposit, degree of exposure, distance to the source, etc. (Aguasanta M. Sarmiento et al., 2009). The microenvironments in which ancient terraces formed 6 Ma ago are completely unknown. Nevertheless, it is possible to compare the behavior of the trace elements during transformation from schwertmannite to fresh goethite over the short term in the modern terrace and from more crystalline goethite to hematite over the long term in the ancient terrace. Conventional geochemical characterization (i.e., pseudo-total digestion and EPMA) provides results consistent with synchrotron radiation μ-XRF; however, the large database of intensities obtained in each μ-XRF map (~500,000 point spectra) allows PCA to be performed to statistically compare the affinity of contaminants for each phase (i.e., between mineralogical layers) and to determine element behavior during the aging process.

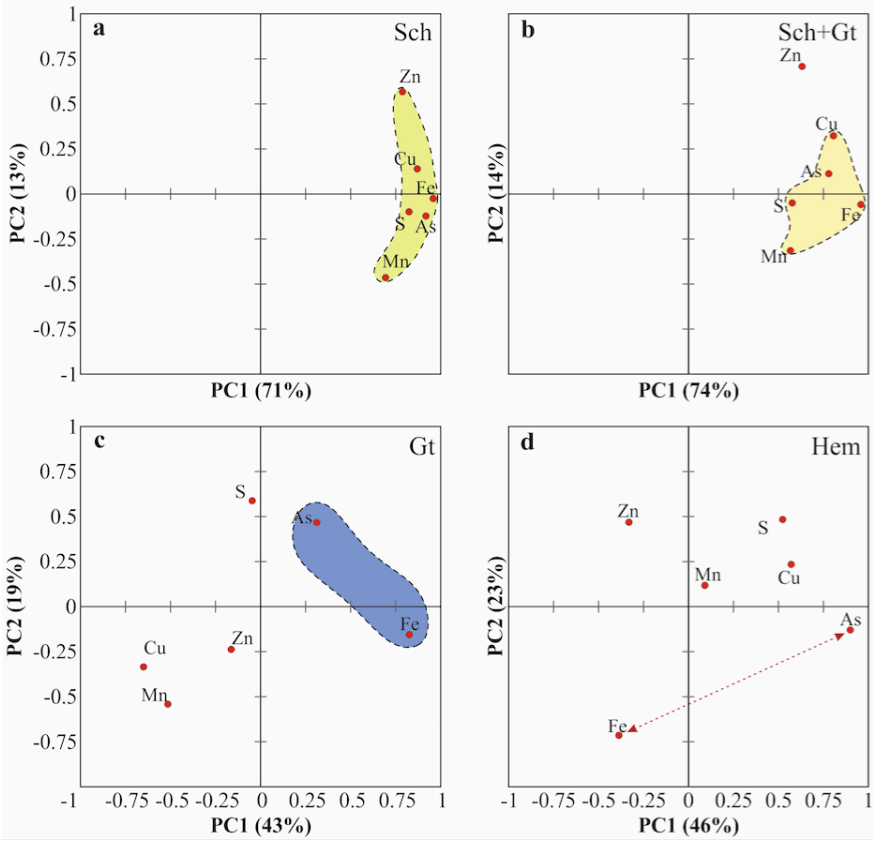

***Fig. 3.6**: Projections of the element intensities obtained by μ-XRF mapping on a plot of the two first principal components from the PCA results for the: (a) upper part of the newly-formed terrace with schwertmannite (sch), (b) deeper part of the newly-formed terrace with a mixture of schwertmannite and goethite (gt), (c) goethite levels of the ancient terrace, and (d) hematite (hem) levels of the ancient terrace.*

In the newly-formed terrace, trace element concentrations exhibit little spatial variation during the aging of schwertmannite to goethite. In the upper part of the sample (first 1 mm) where schwertmannite is the only phase detected, the two first principal components account for 84% of the total variance in the data. Iron is the predominant element and its spatial distribution in the μ-XRF is highly correlated with S (R^2 = 0.81), in agreement with the occurrence of schwertmannite, and with metals, mainly As (R^2 = 0.92) along with Cu (R^2 = 0.78), Mn (R^2 = 0.74), and Zn (R^2 = 0.65). These elements are strongly grouped with positive loading on the first principal component axis (Fig. 6a). Hence, schwertmannite exhibits a high affinity for most of the contaminants in solution.

Analysis of the lower part of the modern terrace, where a mixture of schwertmannite and goethite is detected, revealed that the two first principal components account for 88% of

the total variance in the data. In this zone, Fe is still positively correlated with As (R^2 = 0.88), Cu (R^2 = 0.76), Mn (R^2 = 0.70), S (R^2 = 0.71), and, to a lesser extent, Zn (R^2 = 0.60) along the first component axis (Fig. 6b). However, comparison of both areas demonstrates that the aging from schwertmannite to goethite with depth in the newly-formed terraces is accompanied by a slight decrease in affinity for contaminants and, hence, partial release to the environment. In fact, the grouping of elements in the modern terrace is slightly more dispersed than in the ancient terrace. Nevertheless, the loss of correlation is not substantial and the elevated affinity of the solid phase by trace elements remains throughout the transformation during the early maturation stages of schwertmannite to goethite, which is in agreement with previous observations (Acero et al., 2006).

In contrast, trace element content within the ancient terrace is highly dependent on the mineralogy. Plots of the two first principal components for the goethite and hematite mineralogical zones show they account for 62 and 69% of the total variance in the data, respectively. Analysis of the goethite layers confirms that complete transformation of schwertmannite to goethite is accompanied by a loss of affinity for contaminants. The spatial distribution of Fe is more weakly correlated to As (R^2 = 0.21) and negatively correlated to Cu (R^2 = -0.62), Mn (R^2 = -0.51), S (R^2 = -0.46), and Zn (R^2 = -0.21) (Fig. 6c). This dispersion of elements in the plot is more significant in the hematite layers, where Fe distribution shows a strong negative correlation with all elements of the system: As (R^2 = -0.51), Cu (R^2 = -0.69), Mn (R^2 = -0.70), S (R^2 = -0.82), and Zn (R^2 = -0.12) (Fig. 6d). Therefore, the aging of schwertmannite to goethite and goethite to hematite over time is accompanied by the release of trace elements previously retained by the freshly-formed phases. Although no fluorescence data are available for Pb, EMPA analyses indicate this metal is particularly concentrated in more crystalline phases with aging, a tendency contrary to the other trace elements studied. These results provide clarity with respect to questions raised in the introduction about As behavior and are consistent with previous studies (Bowell, 1994; Pérez-López et al., 2011); they also provide new information with respect to other potentially hazardous trace elements.

Hydrogeochemical modeling at the regional scale could serve as a management tool to predict water quality in AMD-affected river basins under different scenarios. Models must carefully integrate processes of AMD generation, contaminant transport, and natural attenuation by precipitation of schwertmannite. According to our results, the metastability of these precipitates may determine pollutant fluxes over time in these environmental systems: Fe precipitates could initially act as a sink for trace elements, but later become a long-term

source of pollution. This increase in contaminant mobility with aging should be considered in the development of conceptual models. Moreover, these models must serve to optimize the design and location of treatment systems that decrease pollution in the fluvial environment. Dispered Alkaline Substrate-type treatment systems for highly-polluted AMD use a reactive mixture of wood chips and an alkaline additive to neutralize acidity and remove contaminants by induced precipitation of schwertmannite (Macías et al., 2012). Due to the large amount of wood, calcination is one option being considered to decrease the volume and ease the handling of wastes from AMD treatment. Based on the current study, waste burning would cause a forced aging of schwertmannite and, hence, an increase in the potential release of contaminants by leaching that must be taken into account for proper management of these wastes.

REFERENCES

Acero, P., Ayora, C., Torrentó, C., Nieto, J.M., 2006. The behavior of trace elements during schwertmannite precipitation and subsequent transformation into goethite and jarosite. Geochim. Cosmochim. Acta 70, 4130–4139. doi:10.1016/j.gca.2006.06.1367

Amils, R., González-Toril, E., Fernández-Remolar, D., Gómez, F., Aguilera, Á., Rodríguez, N., Malki, M., García-Moyano, A., Fairén, A.G., de la Fuente, V., Luis Sanz, J., 2007. Extreme environments as Mars terrestrial analogs: The Rio Tinto case. Planet. Space Sci. 55, 370–381. doi:10.1016/j.pss.2006.02.006

Amos, R.T., Blowes, D.W., Bailey, B.L., Sego, D.C., Smith, L., Ritchie, a. I.M., 2015. Waste-rock hydrogeology and geochemistry. Appl. Geochemistry 57, 140–156. doi:10.1016/j.apgeochem.2014.06.020

Asta, M.P., Ayora, C., Román-Ross, G., Cama, J., Acero, P., Gault, A.G., Charnock, J.M., Bardelli, F., 2010. Natural attenuation of arsenic in the Tinto Santa Rosa acid stream (Iberian Pyritic Belt, SW Spain): The role of iron precipitates. Chem. Geol. 271, 1–12. doi:10.1016/j.chemgeo.2009.12.005

Asta, M.P., Cama, J., Martínez, M., Giménez, J., 2009. Arsenic removal by goethite and jarosite in acidic conditions and its environmental implications. J. Hazard. Mater. 171, 965–972. doi:10.1016/j.jhazmat.2009.06.097

Bigham, J.M., Schwertmann, U., Traina, S.J., Winland, R.L., Wolf, M., 1996. Schwertmannite and the chemical modeling of iron in acid sulfate waters. Geochim. Cosmochim. Acta 60, 2111–2121. doi:10.1016/0016-7037(96)00091-9

Boon, M., Heijnen, J.., 1998. Chemical oxidation kinetics of pyrite in bioleaching processes. Hydrometallurgy 48, 27–41. doi:10.1016/S0304-386X(97)00072-8

Bowell, R.J., 1994. Sorption of arsenic by iron-oxides and oxyhydroxides in soils. Appl. Geochemistry 9, 279–286.

Burton, E.D., Bush, R.T., Johnston, S.G., Watling, K.M., Hocking, R.K., Sullivan, L. a., Parker, G.K., 2009. Sorption of Arsenic(V) and Arsenic(III) to schwertmannite. Environ. Sci. Technol. 43, 9202–9207. doi:10.1021/es902461x

Cáceres, L.M., Olías, M., De Andrés, J.R., Rodríguez-Vidal, J., Clemente, L., Galván, L., Medina, B., 2013. Geochemistry of Quaternary sediments in terraces of the Tinto River (SW Spain): Paleoenvironmental implications. Catena 101, 1–10. doi:10.1016/j.catena.2012.09.011

Courtin-Nomade, A., Bril, H., Neel, C., Lenain, J.-F., 2003. Arsenic in iron cements developed

within tailings of a former metalliferous mine—Enguialès, Aveyron, France. Appl. Geochemistry 18, 395–408. doi:10.1016/S0883-2927(02)00098-7

Courtin-Nomade, A., Grosbois, C., Marcus, M.A., Fakra, S.C., Beny, J.-M., Foster, A.L., 2009. The weathering of a sulfide orebody: Speciation and fate of some potential contaminants. Can. Mineral. 47, 493–508. doi:10.3749/canmin.47.3.493

Das, R.S., Agrawal, Y.K., 2011. Raman spectroscopy: Recent advancements, techniques and applications. Vib. Spectrosc. 57, 163–176. doi:10.1016/j.vibspec.2011.08.003

Das, S., Hendry, M.J., 2011. Application of Raman spectroscopy to identify iron minerals commonly found in mine wastes. Chem. Geol. 290, 101–108. doi:10.1016/j.chemgeo.2011.09.001

Davidson, L.E., Shaw, S., Benning, L.G., 2008. The kinetics and mechanisms of schwertmannite transformation to goethite and hematite under alkaline conditions. Am. Mineral. 93, 1326–1337. doi:10.2138/am.2008.2761

Egal, M., Elbaz-Poulichet, F., Casiot, C., Motelica-Heino, M., Négrel, P., Bruneel, O., Sarmiento, A.M., Nieto, J.M., 2008. Iron isotopes in acid mine waters and iron-rich solids from the Tinto-Odiel Basin (Iberian Pyrite Belt, Southwest Spain). Chem. Geol. 253, 162–171. doi:10.1016/j.chemgeo.2008.05.006

Essalhi, M., Sizaret, S., Barbanson, L., Chen, Y., Lagroix, F., Demory, F., Nieto, J.M., Sáez, R., Capitán, M.Á., 2011. A case study of the internal structures of gossans and weathering processes in the Iberian Pyrite Belt using magnetic fabrics and paleomagnetic dating. Miner. Depos. 46, 981–999. doi:10.1007/s00126-011-0361-8

Fernandez-Martinez, a., Timon, V., Romaman-Ross, G., Cuello, G.J., Daniels, J.E., Ayora, C., 2010. The structure of schwertmannite, a nanocrystalline iron oxyhydroxysulfate. Am. Mineral. 95, 1312–1322. doi:10.2138/am.2010.3446

Fernández-Remolar, D.C., 2003. Geological record of an acidic environment driven by iron hydrochemistry: The Tinto River system. J. Geophys. Res. 108, 1–15. doi:10.1029/2002JE001918

Fernández-Remolar, D.C., Morris, R. V., Gruener, J.E., Amils, R., Knoll, A.H., 2005. The Río Tinto Basin, Spain: Mineralogy, sedimentary geobiology, and implications for interpretation of outcrop rocks at Meridiani Planum, Mars. Earth Planet. Sci. Lett. 240, 149–167. doi:10.1016/j.epsl.2005.09.043

Filippi, M., Doušová, B., Machovič, V., 2007. Mineralogical speciation of arsenic in soils above the Mokrsko-west gold deposit, Czech Republic. Geoderma 139, 154–170.

doi:10.1016/j.geoderma.2007.01.015

Froment, F., Tournié, A., Colomban, P., 2008. Raman identification of natural red to yellow pigments: ochre and iron-containing ores. J. Raman Spectrosc. 39, 560–568.

Frost, R.L., Wills, R.A., Weier, M.L., Martens, W., 2005. Comparison of the Raman spectra of natural and synthetic K- and Na-jarosites at 298 and 77 K. J. Raman Spectrosc. 36, 435–444. doi:10.1002/jrs.1317

Fukushi, K., Sato, T., Yanase, N., 2003. Solid-solution reactions in As(V) sorption by schwertmannite. Environ. Sci. Technol. 37, 3581–3586. doi:10.1021/es026427i

Fukushi, K., Sato, T., Yanase, N., Minato, J., Yamada, H., 2004. Arsenate sorption on schwertmannite. Am. Mineral. 89, 1728–1734.

Gimenez, J., Martinez, M., de Pablo, J., Rovira, M., Duro, L., 2007. Arsenic sorption onto natural hematite, magnetite, and goethite. J. Hazard. Mater. 141, 575–580. doi:10.1016/j.jhazmat.2006.07.020

Hubbard, C.G., Black, S., Coleman, M.L., 2009. Aqueous geochemistry and oxygen isotope compositions of acid mine drainage from the Río Tinto, SW Spain, highlight inconsistencies in current models. Chem. Geol. 265, 321–334. doi:10.1016/j.chemgeo.2009.04.009

Langmuir, D., 1971. Particle size effect on the reaction goethite = hematite + water.pdf. Am. J. Sci.

Leduc, D., Leduc, L.G., Ferroni, G.D., 2002. Quantification of bacterial populations indigenous to acidic drainage streams. Water. Air. Soil Pollut. 135, 1–21. doi:10.1023/A:1014778301817

Leistel, J.M., Marcoux, E., Thiéblemont, D., Quesada, C., Sânchez, A., Almódovar, G.R., Pascual, E., Sáez, R., 1998. The volcanic-hosted massive sulphide deposits of the Iberian Pyrite Belt: Review and preface to the Thematic Issue. Miner. Depos. 33, 2–30.

Lindsay, M.B.J., Moncur, M.C., Bain, J.G., Jambor, J.L., Ptacek, C.J., Blowes, D.W., 2015. Geochemical and mineralogical aspects of sulfide mine tailings. Appl. Geochemistry 57, 157–177. doi:10.1016/j.apgeochem.2015.01.009

Macías, F., Caraballo, M.A., Rotting, T.S., Perez-Lopez, R., Nieto, J.M., Ayora, C., 2012. From highly polluted Zn-rich acid mine drainage to non-metallic waters: Implementation of a multi-step alkaline passive treatment system to remediate metal pollution. Sci. Total Environ. 433, 323–330. doi:10.1016/j.scitotenv.2012.06.084

Mamindy-Pajany, Y., Hurel, C., Marmier, N., Roméo, M., 2011a. Arsenic (V) adsorption from

aqueous solution onto goethite, hematite, magnetite and zero-valent iron: Effects of pH, concentration and reversibility. Desalination 281, 93–99. doi:10.1016/j.desal.2011.07.046

Mamindy-Pajany, Y., Hurel, C., Marmier, N., Roméo, M., 2011b. Arsenic (V) adsorption from aqueous solution onto goethite, hematite, magnetite and zero-valent iron: Effects of pH, concentration and reversibility. Desalination 281, 93–99. doi:10.1016/j.desal.2011.07.046

Mazzetti, L., Thistlethwaite, P.J., 2002. Raman spectra and thermal transformations of ferrihydrite and schwertmannite. J. Raman Spectrosc. 33, 104–111. doi:10.1002/jrs.830

Müller, K., Ciminelli, V.S.T., Dantas, M.S.S., Willscher, S., 2010. A comparative study of As(III) and As(V) in aqueous solutions and adsorbed on iron oxy-hydroxides by Raman spectroscopy. Water Res. 44, 5660–5672. doi:10.1016/j.watres.2010.05.053

Murad, E., 1997. Identification of minor amounts of anatase in kaolins by Raman spectroscopy. Am. Mineral. 82, 203–206.

Newville, M.G., 2001. IFEFFIT: Interactive XAFS analysis and FEFF fitting. J. Synchrotron Radiat. 8, 322–324. doi:10.4135/9781412983846

Nieto, J.-M., Sarmiento, A.M., Cánovas, C.R., Olías, M., Ayora, C., 2013. Acid mine drainage in the Iberian Pyrite Belt: 1. Hydrochemical characteristics and pollutant load of the Tinto and Odiel Rivers. Environ. Sci. Pollut. Res. Int. 20, 7509–7519. doi:10.1007/s11356-013-1634-9

Nieto, J.M., Sarmiento, A.M., Canovas, C.R., Olias, M., Ayora, C., 2013. Acid mine drainage in the Iberian Pyrite Belt: 1. Hydrochemical characteristics and pollutant load of the Tinto and Odiel rivers. Environ. Sci. Pollut. Res. 20, 7509–7519. doi:10.1007/s11356-013-1634-9

Nieto, J.M., Sarmiento, A.M., Olúas, M., Canovas, C.R., Riba, I., Kalman, J., Delvalls, T.A., 2007. Acid mine drainage pollution in the Tinto and Odiel rivers (Iberian Pyrite Belt, SW Spain) and bioavailability of the transported metals to the Huelva Estuary. Environ. Int. 33, 445–455. doi:10.1016/j.envint.2006.11.010

Nocete, F., Sáez, R., Bayona, M.R., Nieto, J.M., Peramo, A., López, P., Gil-Ibarguchi, J.I., Inácio, N., García, S., Rodríguez, J., 2014. Gold in the Southwest of the Iberian Peninsula during the 3rd Millennium BC. J. Archaeol. Sci. 41, 691–704. doi:10.1016/j.jas.2013.10.006

Olías, M., Nieto, J.M., Pérez-Lépez, R., Cánovas, C.R., Macías, F., Sarmiento, A.M., Galván, L., 2016. Controls on acid mine water composition from the Iberian Pyrite Belt (SW Spain). Catena 137, 12–23. doi:10.1016/j.catena.2015.08.018

Olías, M., Nieto, J.M., Sarmiento, a. M., Cerón, J.C., Cánovas, C.R., 2004. Seasonal water quality variations in a river affected by acid mine drainage: The Odiel River (South West Spain). Sci. Total Environ. 333, 267–281. doi:10.1016/j.scitotenv.2004.05.012

Parviainen, A., Cruz-Hernández, P., Pérez-López, R., Nieto, J.M., Delgado-López, J.M., 2015. Raman identification of Fe precipitates and evaluation of As fate during phase transformation in Tinto and Odiel River Basins. Chem. Geol. 398, 22–31. doi:10.1016/j.chemgeo.2015.01.022

Pérez-López, R., Asta, M.P., Román-Ross, G., Nieto, J.M., Ayora, C., Tucoulou, R., 2011. Synchrotron-based X-ray study of iron oxide transformations in terraces from the Tinto-Odiel river system: Influence on arsenic mobility. Chem. Geol. 280, 336–343. doi:10.1016/j.chemgeo.2010.11.021

Sáez, R., Pascual, E., Toscano, M., Almodóvar, G.R., 1999. The Iberian type of volcano-sedimentary massive sulphide deposits. Miner. Depos. 34, 549–570. doi:10.1007/s001260050220

Sarmiento, A.M., Nieto, J.-M., Casiot, C., Elbaz-Poulichet, F., Egal, M., 2009. Inorganic arsenic speciation at river basin scales: The Tinto and Odiel Rivers in the Iberian Pyrite Belt, SW Spain. Environ. Pollut. 157, 1202–1209. doi:10.1016/j.envpol.2008.12.002

Sarmiento, A.M., Olías, M., Nieto, J.M., Cánovas, C.R., Delgado, J., 2009. Natural attenuation processes in two water reservoirs receiving acid mine drainage. Sci. Total Environ. 407, 2051–2062. doi:10.1016/j.scitotenv.2008.11.011

Solé, V. a., Papillon, E., Cotte, M., Walter, P., Susini, J., 2007. A multiplatform code for the analysis of energy-dispersive X-ray fluorescence spectra. Spectrochim. Acta - Part B At. Spectrosc. 62, 63–68. doi:10.1016/j.sab.2006.12.002

Tornos, F., 2006. Environment of formation and styles of volcanogenic massive sulfides: The Iberian Pyrite Belt. Ore Geol. Rev. 28, 259–307. doi:10.1016/j.oregeorev.2004.12.005

Webster, J.G., Swedlund, P.J., Webster, K.S., 1998. Trace Metal Adsorption onto an Acid Mine Drainage Iron (III) Oxy Hydroxy Sulfate. Environ. Sci ence Technol. 32, 1361–1368. doi:DOI: 10.1021/es9704390

CHAPTER IV

THE ROLE OF AS(V) IN THE PRECIPITATION AND AGEING RATES OF IRON OXIDES OF ACID MINE DRAINAGE

BASED ON:

CRUZ-HERNÁNDEZ, P., PÉREZ-LÓPEZ, R., NIETO, J.M., 2017. ROLE OF ARSENIC DURING THE AGING OF ACID MINE DRAINAGE PRECIPITATES. PROCEDIA EARTH AND PLANETARY SCIENCES IN PRESS.

THE ROLE OF AS(V) IN THE PRECIPITATION AND AGEING RATES OF IRON OXIDES OF ACID MINE DRAINAGE

Iron-rich sediments cover the riverbeds of water streams affected by acid mine drainage (AMD) resulting from sulfide oxidation. The precipitates are mainly composed by schwertmannite, which is a poorly crystalline Fe oxyhydroxysulfate that recrystallizes over relatively short time to goethite. Schwertmannite has an extraordinary capacity to remove some toxic elements. This study examines the influence of the As(V) concentration on the kinetics of precipitation and transformation of schwertmannite by means of batch experiments. A set of samples were synthetized with different As concentrations $[As]_0$, and solid-solution interactions were allowed aging at 40, 60 and 85ºC during different time periods (1h - 300d). The increase of the initial $[As]_0$ concentration notably restrains the precipitation of schwertmannite and its transformation to goethite. Moreover, the transformation of schwertmannite into goethite entails the release of sulfate and, at a longer time scale, of part of the previously retained As. Thus, As acts as a retardant for schwertmannite transformation. Additionally, this toxic element is released from the precipitates once the schwertmannite is transformed, which is per se an environmental paradox. In this study some new evidences of structural defects accumulation provoked by the incorporation of As into the structure decreasing the Fe inclusion. Furthermore, schwertmannite precipitation also plays an important role in the AMD treatment systems; hence, the long-term behavior of these precipitates should be considered for the solid waste management.

4.1 Introduction

Arsenic is one of the elements considered as more harmful for the environment and the human beings (Mandal and Suzuki, 2002). It is commonly associated with metallic sulfide orebodies. These minerals, under meteoric conditions, acidify the water and release high concentrations of sulfates and metal(oid)s such as Fe, As, Cd, Cu, Zn, Pb among others. The leachate resulting from oxidation of sulfide-rich wastes derived from the mining activity is known as acid mine drainage (AMD) (Nieto et al., 2013).

As a consequence of the high concentration of Fe and sulfates, and the acidification of the water, the precipitation of some poorly-crystalline phases occurs. These phases are oxy-hydroxides and oxy-hydroxysulfates, such as schwertmannite [$Fe_8O_8(OH)_x(SO_4)_y \cdot nH_2O$, *(x=8-2y, 1<y<1.75)*], (Bigham et al., 1990; Fernandez-Martinez et al., 2010; Yu et al., 1999). Schwertmannite is commonly accumulated on the riverbeds forming sedimentary terrace-like estructures (Cruz-Hernández et al., 2016; Essalhi et al., 2011). It is considered as a good scavenger of trace elements, mainly oxyanions, on its surface (Acero et al., 2006; Burton et al., 2009; Maillot et al., 2013; Regenspurg and Peiffer, 2005; Schwertmann and Fitzpatrick, 1992), showing predilection for As (Adra et al., 2013; Burton et al., 2009; Carrero et al., 2015; Fukushi et al., 2003a; Regenspurg and Peiffer, 2005). However, the metastability of this phase makes it to transform in natural conditions to goethite [$FeOOH$] in some weeks (Acero et al., 2006), and into hematite over centuries (Parviainen et al., 2015; Pérez-López et al., 2011) or under hydrothermal conditions (Barham, 1997; Davidson et al., 2008). However, the final fate of the As during the transformation of the phases is not completely clarified. Acero et al. (2006) suggests that As remains partitioned to the surface of the goethite while other studies add that is desorb from the structure during the transformation to hematite due to the decrease of surface site density (Cruz-Hernández et al., 2016; Pérez-López et al., 2011). Bolanz et al. (2013) proposed an epitaxial intergrowth of another phase (angelelite, $Fe_4(AsO_4)O_3$) together with hematite, which would retain the most part of the As retained by the ageing product of poorly crystalline Fe oxy-hydroxides.

Throughout this study reaction-rates of precipitation and transformation of schwertmannite have been calculated. The main aim is to discern and quantify differences inducted by the initial As(V) concentration in solution in the kinetics of precipitation and transformation and the final fate of As during the maturation of the precipitates. In addition,

some structural defects provoked by the incorporation of As have been characterized using pair distribution function (PDF). This technique has been successfully implemented on structural studies in poorly-crystalline phases (Fernandez-Martinez et al., 2010; Wang et al., 2015). Furthermore, PDF analysis has also helped to solve the incorporation of traces in the structure of similar phases (Harrington et al., 2010; Li et al., 2011). The precursor phase, schwertmannite, has been synthesized (Eskandarpour et al., 2008; Loan et al., 2004) coprecipitating in presence of different As(V) concentrations at 85, 60 and 40°C during different time periods. In addition, this study was performed with the purpose of optimize the environmental management of mining wastes derived from the mining activity. It is important to quantify the reaction kinetics to make a better prediction of contaminants behavior at long-term.

4.2 Materials and methods

4.2.1 Sample synthesis

Batch experiments were designed and sequentially distributed over time in order to evaluate the role of the initial As(V) concentration in solution on the main mineralogical changes taking place during the diagenesis. Schwertmannite was synthetized by adding previously dehydrated $Fe_2(SO_4)_3 \cdot xH_2O$ in pre-cleansed polyethylene bottles (0.5 L provided with double sealing plug) according to the method proposed by Loan et al. (2004) and Eskandarpour et al. (2008). Both precipitation and transformation of schwertmannite were study using different As(V) concentrations in solution and heat to accelerate the transformation process. Three sets of ageing experiments were carried out as a function of temperature: (1) at 40ºC, in order to calculate the schwertmannite precipitation rates, (2) at 60ºC, in order to study the transformation from schwertmannite to goethite; and (3) a 85ºC to elucidate possible sorption or desorption processes of As during goethite recrystallization at long term. In each set of experiment, the deionized (DI) water was preheated during 24 h before the beginning in order to ensure the temperature stability.

Seven initial As(V) concentrations were used by adding different contents of $Na_2HAsO_4{\cdot}7H_2O$ (0, 0.05, 0.125, 0.25, 0.5, 1 and 2 mM). Given that schwertmannite precipitation spontaneously occurs during the synthesis $Na_2HAsO_4{\cdot}7H_2O$ was firstly added to the preheated DI water before the precipitation. The solutions remained in the oven for variable time periods, ranging from 1 h to 300 days. After experiments, solutions were immediately filtered through 0.45 µm nylon syringe filters, acidified with supra-pure HNO_3 and stored at 4°C until analysis. The pH, redox potential, electric conductivity (EC) and temperature were measured with a portable multi-parameter Crison Mm40+ instrument, calibrated with different buffers for pH (4.01, 7 and 9.2), standard solutions for redox potential (220 and 468 mV) and conductivity (142 and 1471 µS cm^{-1} and 12.8 mS cm^{-1}). Measured redox potentials were corrected in order to obtain the Eh with respect to the standard hydrogen electrode (Nordstrom and Wilde, 1998). Solid samples were recovered by filtering solutions using cellulose nitrate membrane filters in a vacuum system coupled to a Büncher flask. These solids were rinsed twice with DI water and dried at room temperature in presence of silica gel in order to avoid further mineral transformation.

Standards of schwertmannite, goethite and hematite were synthetized. Schwertmannite synthesis was performed following the same methodology that for the ageing experiments. Goethite was synthetized by mixing 180 mL of 5 M KOH and 100 mL of 1 M $Fe(NO_3)_2$ diluted to 2 L with DI water (Schwertmann and Cornell, 1991). The solution was heated at 70°C during 60 h. The precipitates were recovered and rinsed several times with DI water. Standards of hematite were synthetized preheating 2 L of DI water to 98°C with a concentration of 2 mM of HNO_3. Thereafter, 16.06 g of $Fe(NO_3)_2 \cdot 9H_2O$ were added and aged at 98°C during 7 days (Schwertmann and Cornell, 1991). The suspension was collected and washed with DI water.

4.2.2 Analytical methods

Concentrations of dissolved As, Fe, S, and Na in the solutions were analyzed by inductively coupled plasma atomic emission spectrometry (ICP-AES; Jobin-Ybon Ultima2). The analytical errors were estimated to be below 5%. Detection limits were: 0.10 mg/L for Fe, 0.08 mg/L for S, 0.02 mg/L for Na and 0.01 mg/L for As. To check the accuracy of the results, the analysis sequence consisted of laboratory standards, quality control solutions analyzed as blind samples, blanks and duplicates. For solid characterization, bulk powder x-Ray diffraction (XRD) was performed to all the samples by using a Bruker D8 advance diffractometeter with CuKα radiation. Diffractometer was fitted at 40 kV, 30 mA, and with a scan range of 2-65° 2θ, 0.05 °2θ step size, and 20 s time per step. It was also used a transmission electronic microscope (TEM), JEOL JEM-1011 coupled with MEGAVIEW III. The voltage was fixed at 100 kv. Solid samples were firstly suspended in acetone by ultrasonic vibration and an aliquot was dropped on a 2 mm carbon support film grid. All analyses were performed in the laboratories of the University of Huelva.

High energy X-ray diffraction (HEXD) measurements were conducted in beamline ID31 at the European Synchrotron Radiation Facility (ESRF, Grenoble, France). Series of same concentration (0.125 mM), time (8 hours, and 10 and 300 days) and temperature (40, 60 and 85 °C), and three standards were disposed in polyamide (kapton) capillaries. The analysis was performed at room temperature in a Q-range of 0-25 $Å^{-1}$. Incident monochromatic X-ray beam had energy of approximately 69.5 keV (λ = 0.1784 Å) in transmission mode that was calibrated using a CeO_2 standard (NIST 679b). The 2D-imagen collected by the flat panel Perkin Elmer 2D detector were corrected and integrated using Fit2D software (Hammersley et al., 1996). PDFs were obtained by Fourier transformation of the structure factor, S(Q), with

the background scattering corrected using PDFgetX3 (Juhás et al., 2013). Additionally, differential pair distribution function (d-PDF) were obtained by subtracting a PDF of reference sample (As-free Fe-precipitate in concentration sequence) from the PDFs of samples with different $[As]_0$ concentration. The lineal combination fit from PDF results were calculated using the PDFGui software (Farrow et al., 2009) in order to ascertain the proportion of each phase (schwertmannite, goethite and hematite) in the different samples.

4.3 Results and discussion

4.3.1 Mineralogical composition

Powder CuKα and synchrotron XRD data showed that schwertmannite was the only phase precipitated initially in most of the experiments (see HEDX pattern in Fig. 1a). Only in experiments with the highest As concentrations (1 mM for 40º and 60°C, and 1 and 2 mM for 85°C), a phase with less crystallinity than schwertmannite was initially formed instead (Fig. 1b). Secondly, schwertmannite was transformed into goethite, which progressively appeared in all the ageing experiments (Fig. 1c).

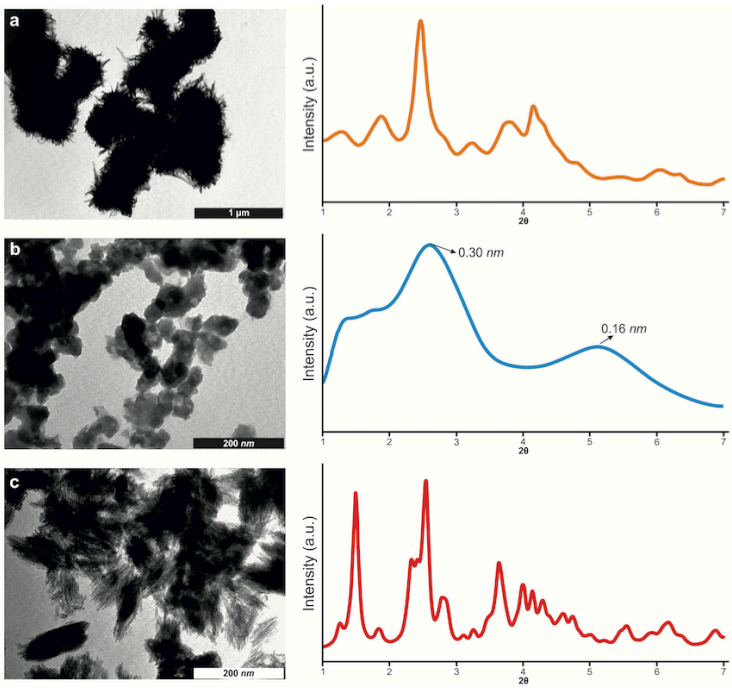

***Fig. 4.1**: TEM pictures and HEXD patterns of the (a) schwertmannite, (b) pseudpamorphpus FeOHAs, (c) goethite.*

TEM observations revealed that synthetic schwertmannite formed aggregates of 300 nm to 1 µm in diameter with pin-cushion morphology (Fig. 1a). The nanocrystals were elongated needles of 5nm width and 30nm long. Goethite crystals are elongated (between 300 nm and 1 µm and 10 and 25 nm) and compound by Fe (≈65% ±4%) and O (34%±4%) (Fig. 1c). On the other hand, the poorly crystalline phase occurring at high concentrations of As in solution contains, as expected, a high concentration of As (≈ 25 ± 5 wt.%), in addition to Fe (≈33 ± 2 wt.%), O (≈38 ± 10 wt.%) and traces of S (<4 wt.%). The phase forms granular

aggregates of 10 to 50 nm of size (Fig. 1b). The HEDX pattern of this As-rich phase exhibits two broad diffraction peaks at 0.30 and 0.16 nm (Fig. 1b). These peaks correspond to a pseudoamorphous Fe-hydroxyarsenate [$FeOHAs$] that typically precipitates instead of schwertmannite when the ratio of $As/Fe \geq 0.15$, according to the previous observations reported elsewhere (Carlson et al., 2002; Krause and Ettel, 1989). Paktunc et al. (2008) described this phase as an amorphous precursor of scorodite. Thus, increase of As concentration seems to decrease the crystallinity of the initial precipitates.

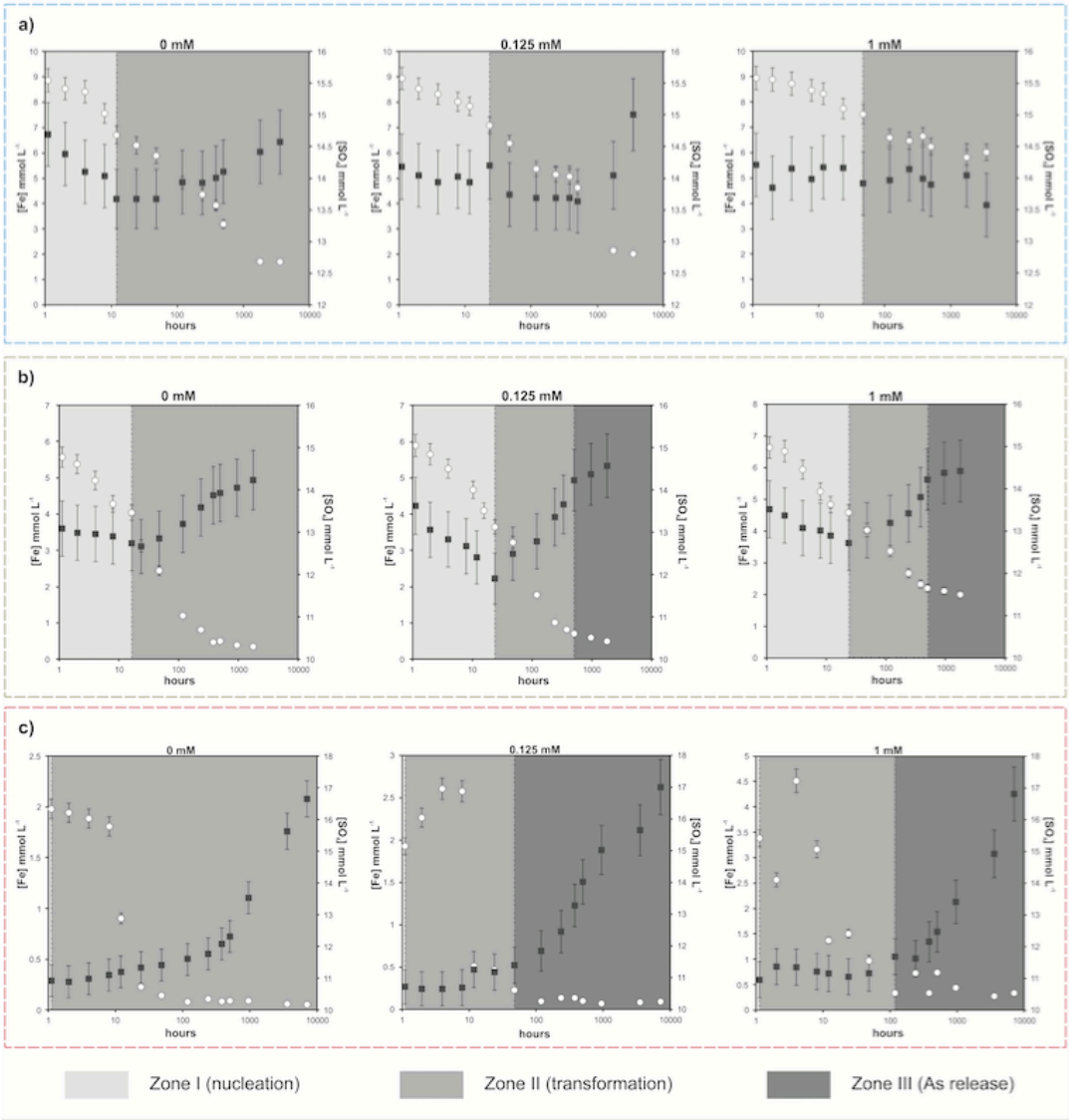

Fig. 4.2: *[Fe] and [SO_4] concentration of supernatant water at (a) 40°C (b) 60°C and (c) 85°C. Full chemical information is included as Appendix 4.*

4.3.2 Chemical evolution

The evolutions of physic-chemical parameters along the experiments are shown in Appendix 4.1. The acceleration of ageing, inducted by the temperature, leads to vary the physic-chemical parameters pending on the process having place in the experiment. Thus, EC decrease in faster in those experiments in which the precipitation rate is higher. The variation of pH is also affected by the precipitation and transformation. These changes agree with two different facts: (1) the transformation from schwertmannite to goethite involves the release of H^+, acidifiying the water media (Bigham et al., 1996; Gagliano et al., 2004), and (2) the stability of goethite in acid environments such us pH≈2 requires lower Eh (Bigham et al., 1996; Caraballo et al., 2013).

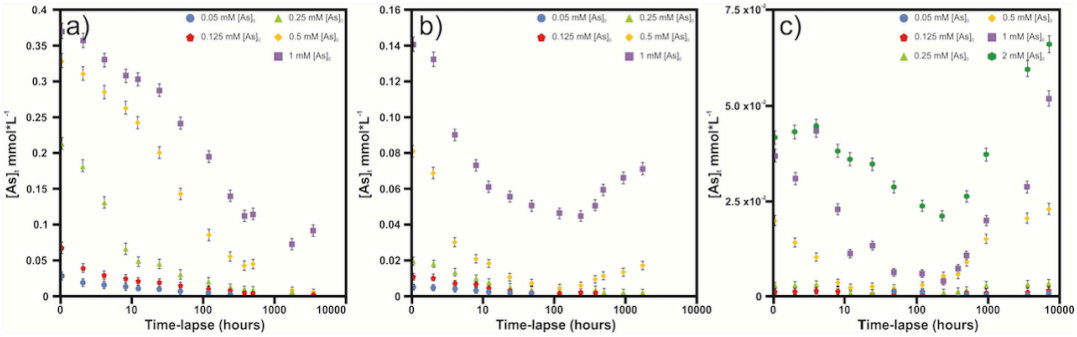

Fig. 4.3: *[As] concentration of supernatant water at (a) 40°C (b) 60°C and (c) 85°C.*

Figure 2 shows the evolution of $[Fe]_t$ and $[SO_4]_t$ along some of the ageing experiments. The remaining graphs are included in appendix. As a general description, both $[Fe]_t$ and $[SO_4]_t$ broadly have the same behavior in all the experiments for the different temperatures. At the onset of the experiments, Fe and SO_4 concentrations in solution decrease. However, $[SO_4]_t$ reaches a minimum concentration from which starts to rise up recovering the original concentration (up to ~90%). Instead, Fe in solution reaches a steady-state after the initial decreasing with values close and lower to the detection limit. Meanwhile [As] at the onset of the experiment is concomitant with $[SO_4]$ and [Fe], but at long-term As is partially released showing a similar trend that $[SO_4]$ at the end of experiments (Fig. 3).

The ageing experiments could be divided into three different zones based on the chemical and mineralogical trends observed during the experimental run: (zone I) the initial decrease of [Fe] and $[SO_4]$ is related to the nucleation and precipitation of the precursor Fe

phase, i.e. schwertmannite, except for high As concentrations; (zone II) after the minimum concentration, the release of SO_4 in solution again, while [Fe] keeps decreasing, is related to the transformation of schwertmannite into goethite; and (zone III) when the solution-goethite equilibrium is achieved marked by the steady-state of [Fe], [As] is desorbed in solution. The release of [As] in solution is of up to 10% of the initial concentration; however, this trend does not reach a steady-state but seems to continue progressively at the moment of ending the experiment. Therefore, these values must be much higher at longer time.

The main difference between the sets of aging experiments (40º, 60º and 85ºC) is the extension of these three zones. Zone I is much wider in the experiments at 40°C than in other temperatures. There is a continuous decrease of the [Fe] that gradually reaches the steady-state; therefore, the precipitation rates of Fe phases can be calculated in this set of experiments (subsection 3.3). On the contrary, the $[SO_4]_t$ variation depends on the $[As]_0$ and, in some cases in which $[As]_0$ is very high, the transformation to goethite seems not to take place. In the case of the experiments at 60°C, the precipitation zone I is more narrow and in 1 hour most part of schwertmannite or Fe-hydroxyarsenate has already precipitated. In these experiments, the minimum $[SO_4]$ is reached between 24 and 48 h and the zone II associated with the progressive release of SO_4 by the transformation to goethite is better-defined. In the experiments at 60°C with high $[As]_0$ (0.5 and 1 mM) it is possible to detect the release of As to the solution, but this fact is not as important as in the experiments at 85°C. In this last set of experiments, the precipitation zone is completed and the transformation has already started in the first hour. The $[SO_4]$ starts in the minimum and is continuously released until reaching the initial concentration used to synthesize schwertmannite. The 78% of Fe is not in solution, and precipitates till it achieves equilibrium, what takes between 12 and 48 hours. In the experiments at 85ºC, the zone III corresponding to the release of As to solution is better seen.

4.3.3 Precipitation and transformation rates

In the ageing experiments at 40º, the initial zone 1 of precipitation of the precursor Fe phase is well-defined. Hence, it is possible to calculate the precipitation rates by linear regression where the change in [Fe] is linear with time (mmol L^{-1} h^{-1}). In the As-free experiment, the precipitation rate of schwertmannite over the pH range 1.9-2.3 was 0.19 mmol Fe L^{-1} h^{-1}. Furthermore, schwertmannite precipitation rate trends to decrease with increasing the $[As]_0$ (0.11, $4.0x10^{-2}$, $3.6x10^{-2}$ and $3.2x10^{-2}$ mmol Fe L^{-1} $hour^{-1}$ in experiments where $[As]_0$ = 0.05, 0.125, 0.25, 0.5, and 1 mM). Note that the precursor phase for experiments

at 1 mM of $[As]_0$ is a Fe-hydroxyarsenate instead of schwertmannite; however, the calculated rate keeps the same trend. Correlating these rates with $[As]_0$ it seems reasonable to affirm that the precipitation of schwertmannite is retarded with the increase of $[As]_0$ in solution (Fig. 4). Although the zone 1 is less well defined in the experiments at 60ºC, the calculations of precipitation rates during the first hour and their correlation with $[As]_0$ is fully consistent with the observations found in the experiments at 40°C (Appendix 4.3).

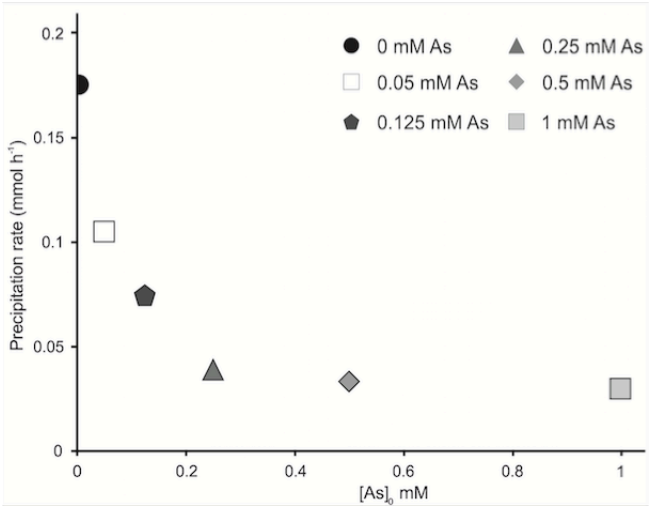

Fig. 4.4: *Calculated precipitation rates and its variation depending on* $[As]_0$

The influence of the $[As]_0$ on the transformation rates of the precursor Fe phase into goethite was observed from the calculation of the goethite proportion in the samples by linear combination fitting with the PDF analysis in the experimental sets where the zone II was better-defined, i.e. at 60º and 85°C. Figure 5 shows the results of goethite content in the samples (wt.%) vs. $[As]_0$. In the case of the experiments at 60°C, the time-lapse chosen was 10 days (Fig. 5a), while at 85°C the samples were left during 300 days (Fig. 5b). The findings indicate that the proportion of goethite and, hence, the transformation rate of schwertmannite also decreases with the increase of $[As]_0$ in solution. Thus, the transformation rate of schwertmannite to goethite is also drastically decelerated.

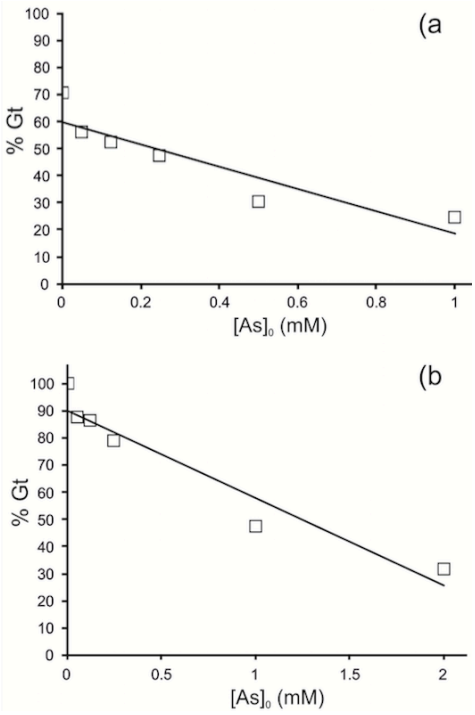

Fig. 4.5: *Goethite content of solid samples (wt.%) compared to $[As]_0$ experiments at (a) 60°C aged during 10 days, (b) 85°C aged during 300 days.*

4.3.4 Structural implications

The incorporation of As to the structure of Fe-precipitates entails several consequences. Some works suggest that S and As (as SO_4 and AsO_4, respectively) share position into the structure of schwertmannite (Antelo et al., 2012; Burton et al., 2009). Figure 6a shows PDF analyses of the entire set of ageing experiments (0, 0.05, 0.125, 0.25, 0.5 and 1 mM of As(V)) at 60 °C for samples taken at the same time interval (10 days). In addition, d-PDF shows the short-range order (< 4 Å) around As in the solid phases (Fig. 6b). This set of samples was selected as an example, but identical results were obtained for other sets of experiments (added in appendix IV). PDF results revealed that the increasing of $[As]_0$ yields precipitates with similar structural feature, lower crystallinity and shorter coherent domain based on the intensity decreasing and widening of the peaks, especially in long-range pairs (Fig. 6a).

The d-PDF (Fig. 6b) indicates that arsenate is located as bidentate binucleate inner-sphere position. This coordination is congruent with the presence of two positive peaks at

~1.68 and ~3.3 Å , related to As-O distance in a undistorted arsenate tetrahedral and As-Fe distance, respectively, where arsenate tetrahedral forms two covalent bonds with the Fe-framework (Harrington et al., 2010). In addition, two negative peaks at ~1.98 Å and ~3.0 Å, which correspond to bonds Fe-O (first neighbor) and O-O into the Fe-framework are reduced or distorted. Thus, As incorporation provokes vacancies of Fe octahedra or important deformations. The accumulation of these defects avoids the development of further periodicity in samples with high As load, reducing the coherent domain and, therefore, the crystallinity of the phase.

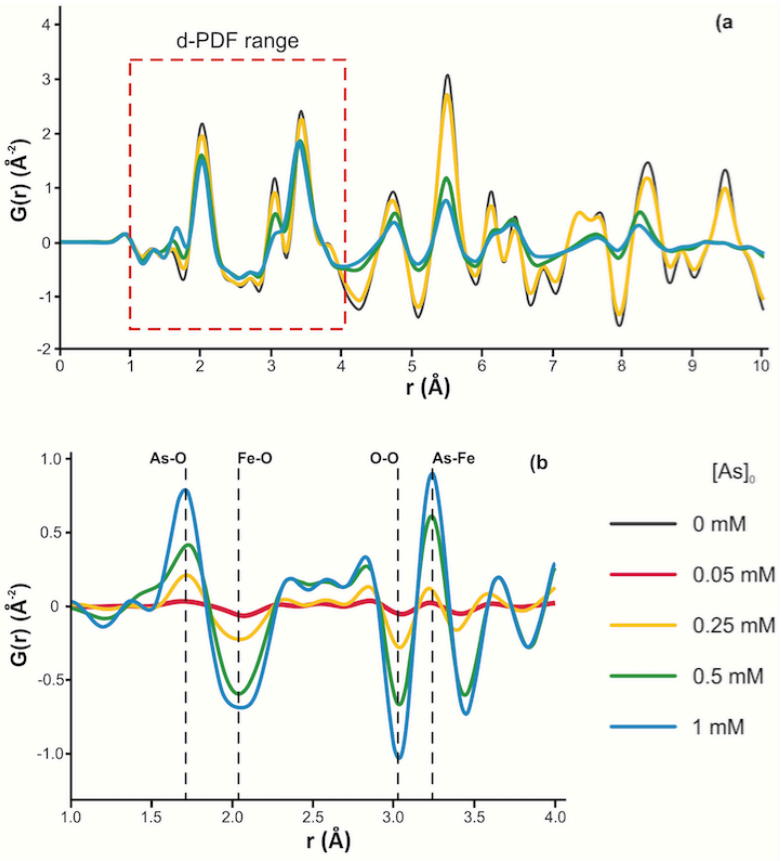

Fig. 4.6: *(a) PDF analysis and (b) d-PDF of As in samples aged during 10 days at 60°C and loaded with different [As]$_0$.*

Ageing also reduces the incorporation of As in the structure, inasmuch as the As-O peak (~1.68 Å) is slightly less intense in experiments performed at higher temperatures, although the effect of As concentration in the structure is similar in all isothermal experiments. Arsenic inhibits the fixation of sulfates in the structure, due likely to that both

share position (Burton et al., 2013; Wang et al., 2015) and to the high affinity of As with these precipitates (Fukushi et al., 2003b).

REFERENCES

Acero, P., Ayora, C., Torrentó, C., Nieto, J.M., 2006. The behavior of trace elements during schwertmannite precipitation and subsequent transformation into goethite and jarosite. Geochim. Cosmochim. Acta 70, 4130–4139. doi:10.1016/j.gca.2006.06.1367

Adra, A., Morin, G., Ona-Nguema, G., Menguy, N., Maillot, F., Casiot, C., Bruneel, O., Lebrun, S., Juillot, F., Brest, J., 2013. Arsenic scavenging by aluminum-substituted ferrihydrites in a circumneutral pH river impacted by acid mine drainage. Environ. Sci. Technol. 47, 12784–12792. doi:10.1021/es4020234

Antelo, J., Fiol, S., Gondar, D., López, R., Arce, F., 2012. Comparison of arsenate, chromate and molybdate binding on schwertmannite: Surface adsorption vs anion-exchange. J. Colloid Interface Sci. 386, 338–343. doi:10.1016/j.jcis.2012.07.008

Barham, R.J., 1997. Schwertmannite: A unique mineral, contains a replaceable ligand, transforms to jarosites, hematites, and/or basic iron sulfate. J. Mater. Res. 12, 2751–2758.

Bigham, J.M., Schwertmann, U., Carlson, L., Murad, E., 1990. A poorly crystallized oxyhydroxysulfate of iron formed by bacterial oxidation of Fe(II) in acid mine waters. Geochim. Cosmochim. Acta 54, 2743–2758. doi:10.1016/0016-7037(90)90009-A

Bigham, J.M., Schwertmann, U., Traina, S.J., Winland, R.L., Wolf, M., 1996. Schwertmannite and the chemical modeling of iron in acid sulfate waters. Geochim. Cosmochim. Acta 60, 2111–2121. doi:10.1016/0016-7037(96)00091-9

Bolanz, R.M., Maria Wierzbicka-Wieczorek, M.C.´aplovicova, Peter Uhlík, J., Göttlicher, R., Ralph Steininger, and J.M., 2013. Structural incorporation of arsenic (V) into hematite 47, 9140–9147. doi:dx.doi.org/10.1021/es305182c

Burton, E.D., Bush, R.T., Johnston, S.G., Watling, K.M., Hocking, R.K., Sullivan, L. a., Parker, G.K., 2009. Sorption of Arsenic(V) and Arsenic(III) to schwertmannite. Environ. Sci. Technol. 43, 9202–9207. doi:10.1021/es902461x

Burton, E.D., Johnston, S.G., Kraal, P., Bush, R.T., Claff, S., 2013. Sulfate availability drives divergent evolution of arsenic speciation during microbially mediated reductive transformation of schwertmannite. Environ. Sci. Technol. 47, 2221–2229.

doi:10.1021/es303867t

Caraballo, M.A., Rimstidt, J.D., Mac??as, F., Nieto, J.M., Hochella, M.F., 2013. Metastability, nanocrystallinity and pseudo-solid solution effects on the understanding of schwertmannite solubility. Chem. Geol. 360-361, 22–31. doi:10.1016/j.chemgeo.2013.09.023

Carlson, L., Bigham, J.M., Schwertmann, U., Kyek, A., Wagner, F., 2002. Scavenging of As from Acid Mine Drainage by Schwertmannite and Ferrihydrite : A Comparison with Synthetic Analogues Scavenging of As from Acid Mine Drainage by Schwertmannite and Ferrihydrite : A Comparison with Synthetic Analogues 36, 1712–1719. doi:10.1021/es0110271

Carrero, S., Pérez-López, R., Fernandez-Martinez, A., Cruz-Hernández, P., Ayora, C., Poulain, A., 2015. The potential role of aluminium hydroxysulphates in the removal of contaminants in acid mine drainage. Chem. Geol. 417, 414–423. doi:10.1016/j.chemgeo.2015.10.020

Cruz-Hernández, P., Pérez-López, R., Parviainen, A., Lindsay, M.B.J., Nieto, J.M., 2016. Trace element-mineral associations in modern and ancient iron terraces in acid drainage environments. Catena 147, 386–393. doi:10.1016/j.catena.2016.07.049

Davidson, L.E., Shaw, S., Benning, L.G., 2008. The kinetics and mechanisms of schwertmannite transformation to goethite and hematite under alkaline conditions. Am. Mineral. 93, 1326–1337. doi:10.2138/am.2008.2761

Eskandarpour, A., Onyango, M.S., Ochieng, A., Asai, S., 2008. Removal of fluoride ions from aqueous solution at low pH using schwertmannite. J. Hazard. Mater. 152, 571–579. doi:10.1016/j.jhazmat.2007.07.020

Essalhi, M., Sizaret, S., Barbanson, L., Chen, Y., Lagroix, F., Demory, F., Nieto, J.M., Sáez, R., Capitán, M.Á., 2011. A case study of the internal structures of gossans and weathering processes in the Iberian Pyrite Belt using magnetic fabrics and paleomagnetic dating. Miner. Depos. 46, 981–999. doi:10.1007/s00126-011-0361-8

Farrow, C.L., Juhás, P., Liu, J.W., Bryndin, D., Bozin, E.S., Bloch, J., Proffen, T., Billinge, S.J.L., 2009. PDFgui user guide.

Fernandez-Martinez, A., Timon, V., Romaman-Ross, G., Cuello, G.J., Daniels, J.E., Ayora, C., 2010. The structure of schwertmannite, a nanocrystalline iron oxyhydroxysulfate. Am. Mineral.

95, 1312–1322. doi:10.2138/am.2010.3446

Fukushi, K., Sasaki, M., Sato, T., Yanase, N., Amano, H., Ikeda, H., 2003a. A natural attenuation of arsenic in drainage from an abandoned arsenic mine dump. Appl. Geochemistry 18, 1267–1278. doi:10.1016/S0883-2927(03)00011-8

Fukushi, K., Sato, T., Yanase, N., 2003b. Solid-solution reactions in As(V) sorption by schwertmannite. Environ. Sci. Technol. 37, 3581–3586. doi:10.1021/es026427i

Gagliano, W.B., Brill, M.R., Bigham, J.M., Jones, F.S., Traina, S.J., 2004. Chemistry and mineralogy of ochreous sediments in a constructed mine drainage wetland. Geochim. Cosmochim. Acta 68, 2119–2128. doi:10.1016/j.gca.2003.10.038

Hammersley, A.P., Svensson, S.O., Hanfland, M., Fitch, A.N., Häusermann, D., 1996. Two-dimensional detector software: From real detector to idealised image or two-theta scan. High Press. Res. 14, 235–248.

Harrington, R., Hausner, D.B., Bhandari, N., Strongin, D.R., Chapman, K.W., Chupas, P.J., Middlemiss, D.S., Grey, C.P., Parise, J.B., 2010. Investigation of surface structures by powder diffraction: a differential pair distribution function study on arsenate sorption on ferrihydrite. Inorg. Chem. 49, 325–330. doi:10.1021/ic9022695

Juhás, P., Davis, T., Farrow, C.L., Billinge, S.J.L., 2013. PDFgetX3: A rapid and highly automatable program for processing powder diffraction data into total scattering pair distribution functions. J. Appl. Crystallogr. 46.

Krause, E., Ettel, V.A., 1989. Solubilities and stabilities of ferric arsenate compounds. Hydrometallurgy 22, 311–337. doi:10.1016/0304-386X(89)90028-5

Li, W., Harrington, R., Tang, Y., Kubicki, J.D., Aryanpour, M., Reeder, R.J., Parise, J.B., Phillips, B.L., 2011. Differential pair distribution function study of the structure of arsenate adsorbed on nanocrystalline γ-alumina. Environ. Sci. Technol. 45, 9687–9692. doi:10.1021/es200750b

Loan, M., Cowley, J.M., Hart, R., Parkinson, G.M., 2004. Evidence on the structure of synthetic schwertmannite. Am. Mineral. 89, 1735–1742.

Maillot, F., Morin, G., Juillot, F., Bruneel, O., Casiot, C., Ona-Nguema, G., Wang, Y., Lebrun, S., Aubry, E., Vlaic, G., Brown, G.E., 2013. Structure and reactivity of As(III)- and As(V)-rich

schwertmannites and amorphous ferric arsenate sulfate from the Carnoulès acid mine drainage, France: Comparison with biotic and abiotic model compounds and implications for As remediation. Geochim. Cosmochim. Acta 104, 310–329. doi:10.1016/j.gca.2012.11.016

Mandal, B.K., Suzuki, K.T., 2002. Arsenic round the world: A review. Talanta 58, 201–235. doi:10.1016/S0039-9140(02)00268-0

Nieto, J.M., Sarmiento, A.M., Canovas, C.R., Olias, M., Ayora, C., 2013. Acid mine drainage in the Iberian Pyrite Belt: 1. Hydrochemical characteristics and pollutant load of the Tinto and Odiel rivers. Environ. Sci. Pollut. Res. 20, 7509–7519. doi:10.1007/s11356-013-1634-9

Nordstrom, D.K., Wilde, F.D., 1998. Reduction-oxidation potential (electrode method), in: In National Field Manual for the Collection of Water-Quality Data. p. 20.

Paktunc, D., Dutrizac, J., Gertsman, V., 2008. Synthesis and phase transformations involving scorodite, ferric arsenate and arsenical ferrihydrite: Implications for arsenic mobility. Geochim. Cosmochim. Acta 72, 2649–2672. doi:10.1016/j.gca.2008.03.012

Parviainen, A., Cruz-Hernández, P., Pérez-López, R., Nieto, J.M., Delgado-López, J.M., 2015. Raman identification of Fe precipitates and evaluation of As fate during phase transformation in Tinto and Odiel River Basins. Chem. Geol. 398, 22–31. doi:10.1016/j.chemgeo.2015.01.022

Pérez-López, R., Asta, M.P., Román-Ross, G., Nieto, J.M., Ayora, C., Tucoulou, R., 2011. Synchrotron-based X-ray study of iron oxide transformations in terraces from the Tinto-Odiel river system: Influence on arsenic mobility. Chem. Geol. 280, 336–343. doi:10.1016/j.chemgeo.2010.11.021

Regenspurg, S., Peiffer, S., 2005. Arsenate and chromate incorporation in schwertmannite. Appl. Geochemistry 20, 1226–1239. doi:10.1016/j.apgeochem.2004.12.002

Schwertmann, U., Cornell, R.M., 1991. Iron oxides in the laboratory. New York.

Schwertmann, U., Fitzpatrick, R.W., 1992. Iron minerals in surface environments. Catena Suppl.

Wang, X., Gu, C., Feng, X., Zhu, M., 2015. Sulfate Local Coordination Environment in Schwertmannite. Environ. Sci. Technol. 49, 10440–10448. doi:10.1021/acs.est.5b02660

Yu, J.Y., Heo, B., Choi, I.K., Cho, J.P., Chang, H.W., 1999. Apparent solubilities of schwertmannite and ferrihydrite in natural stream waters polluted by mine drainage. Geochim. Cosmochim. Acta 63, 3407–3416. doi:10.1016/S0016-7037(99)00261-6

CHAPTER V

GENERAL CONCLUSIONS

CONCLUSIONS

The ageing of Fe phases, as well as the behavior of the environmentally significant trace elements, in sulfide-derived acid mine drainages (AMD) has been aimed to highlight throughout the development of the present Doctoral Thesis. The main objectives set at the beginning of this work were to: (1) study in detail, i.e. at micrometer scale, the chemical and mineralogical composition of Fe-phases in natural (newly-formed and fossil) terraces formed along the riverbeds impacted by acid drainage, (2) identify the mineral transformation process and the long-term behavior of the involved elements, (3) evaluate the role of As(V) on the kinetic rates of precipitation and maturation of the precipitates, (4) elucidate structural changes caused by incorporation of As(V), and (5) compare the obtained data in the laboratory with those observed on field. From the experiments conducted and considering the results obtained, this study arrives to the following conclusions:

- The first part of the study focuses on the newly-formed and ancient fluvial terraces in the IPB. Schwertmannite is the principal phase currently forming in the riverbeds affected by AMD characterized by low pH (2.5-3.1) and high concentrations of sulfate. In AMD conditions, the terrace precipitates act as a sink for As, and to some extent divalent cations such as Cu, Co, Pb, and Zn are also trapped from the solution. In the deeper layers with older sediments, metastable schwertmannite has transformed partially or entirely into goethite and jarosite. After long-term phase transformation along thousands of years from precursor schwertmannite to goethite and eventually to hematite through diagenetic processes, the well-crystallized goethite and hematite in the ancient terrace samples contain relatively elevated concentrations of trace elements reflecting the ARD conditions of the ancient Tinto River. The phase transformations influence the long-term retention capacity of As because the consecutive phases are less effective sorbents than the initial sink. This should be taken into account when designing environmental models, because the changes in the mineralogy of the terraces may trigger a reverse process after the natural attenuating effect of schwertmannite.
- On the basis of this study, Raman spectroscopy is a suitable tool for the study of Fe(III) oxides, oxyhydroxides and oxyhydroxysulfates, and it could replace bulk XRD analysis. Though, Raman spectroscopy is well-known technique, it is not established in the study of Fe(III) precipitates in AMD environment. For these studies, Raman spectroscopy is especially suitable as it offers easy and reliable detection on a micro to millimeter scale of

phases, such as schwertmannite, difficult to identify by XRD in a bulk sample with multimineral paragenesis. However, the XRD provides an estimation of the relative mineral ratios which Raman spectroscopy fails to do. Though, in the case of schwertmannite, it is challenging with even XRD due to its low crystallinity.

- Regarding the long-term fate of some of the main pollutants retained in Fe terraces formed along riverbeds impacted by acid mine drainage (AMD): Comprehensive analyses including chemical digestion, Raman μ-spectroscopy, electron probe microanalysis, and synchrotron-based μ-X-ray fluorescence were performed on iron terrace samples taken in fluvial courses of the Iberian Pyrite Belt (SW Iberian Peninsula). Samples were taken from actively-forming modern terraces as well as ancient terraces isolated due to river migration over time. Schwertmannite was the main newly-formed phase precipitated from the polluted water and comprised the upper part of modern terraces. This schwertmannite was highly positively correlated to As as well as Cu, Mn, S, and Zn, indicating that this phase controlled the uptake of these elements. However, progressive maturation of schwertmannite to goethite in the deeper part of modern terraces and especially in ancient terraces appears responsible for a decrease in this correlation and hence an increase in element mobility. This loss of affinity for contaminants is particularly evident in the hematite resulting from the transformation of goethite in the ancient terraces. The spatial distribution of hematite is negatively correlated with the concentration of most trace elements; Pb was the only trace element to show a higher affinity for this most crystalline phase after aging. Therefore, schwertmannite that retains contaminants in the newly-formed sediments may serve as a long-term source of these contaminants to the environment due to mineralogical transformations.
- This research has proved the interference of As(V) during schwertmannite transformation into goethite and its re-crystallization. In addition, kinetics of precipitation and transformation have been calculated at short, medium and long term with different concentrations of As(V). Arsenic controls the transformation processes on the phases, but also is released from their structures once these become more crystalline. In addition, using the d-PDF it has been possible to detect the structural implications of introducing As to schwertmannite, even forming a new amorphous phase at high $[As]_0$. The remobilization of As during the maturation of the AMD sediments could have huge implications in the long-term fate of AMD-related pollutants. In addition, this information must be considered in the management of the wastes obtained in the passive AMD

treatments. However, this study plans to be expanded to include the formation of more stable phases such as hematite, to evaluate the behavior of trace elements during the complete transformation of AMD precipitates.

Despite the studies carried out during the development of this thesis, there are some questions regarding the behavior of trace metals during their diagenesis. Future studies should highlight the preparation of a new series of batch experiments that would form hematite from the synthesis of schwertmannite. Above all, it is important to focus those studies on the possible liberation and retention of trace elements held in the precipitates. Furthermore, the structural defects should be thoroughly studied by synthetic and natural experiments. On the other hand, a possible use of the wastes generated by passive treatment systems should be designed since present day proposals (incineration) might remobilize the pollutants and bring them back to the natural circle. Finally, it should be highlighted the need for a rigorous characterization of the pseudo-amorphous phase detected in those experiments with high As concentrations due to the retention of a considerable part of As in solution.

CONCLUSIONES

El envejecimiento de las fases de Fe, así como el comportamiento de los metales traza asociados a sulfuros metálicos más importantes para el medio ambiente en drenajes ácidos de mina (AMD en sus siglas en inglés *acid mine drainage*) han sido los principales objetivos fijados durante el desarrollo de la tesis doctoral. Los principales objetivos planteados al comienzo de este trabajo fueron: (1) estudiar en detalle, por ejemplo a escala milimétrica, la composición química y mineralógica de las fases de Fe en terrazas naturales (recién formadas y fósiles) formadas a lo largo de las cuencas afectadas por los drenaje ácidos, (2) identificar el proceso transformación mineral y el comportamiento largo plazo de los elementos implicados (3) evaluar el papel de As(V) en los ratios cinéticos de precipitación y maduración de los precipitados, (4) dilucidar los cambios estructurales causados por la incorporación de AS(V), y (5) comparar los datos obtenidos en el laboratorio con aquellos observados en el campo. De los experimentos realizado y considerando los resultado obtenidos, este estudio ha llegado a las siguiente conclusiones:

- La primera parte del estudio se centra en el terrazas fluviales modernas y antiguas de la Faja Pirítica Ibérica. La schwertmannita es la principal fase que actualmente se está formando en las cuencas afectadas por AMD, caracterizadas por formarse a un pH bajo (2.5-3.1) y altas concentraciones de sulfatos. En condiciones de AMD, los precipitados de las terrazas actúan como captadores para el As, y, hasta cierto punto, algunos cationes divalentes como Cu, Co, Pb, y Zn son también retirados de la solución. En las capas más profundas con sedimentos más antiguos, la schwertmannita metaestable se ha transformado parcial o completamente en goethita y jarosita. Después de una fase de transformación a largo plazo de más de miles de años y de que la schwertmannita precursora haya pasado a goethita y, eventualmente, a hematite a través de procesos diagenéticos, la goethita y la hemática bien cristalizadas en las muestras de terrazas antiguas contienen concentraciones relativamente altas de elementos traza que reflejan las condiciones ARD del antiguo Río Tinto. Las fases de transformación influyen en la capacidad de retención a largo plazo del As ya que la fases consecutivas son sorbentes menos efectivos que los captadores iniciales. Esto debe ser tenido en cuenta cuando se diseñan modelos medio ambientales puesto que los cambios en la mineralogía de las terrazas puede provocar un proceso contrario después de efecto atenuador natural de la schwertmannita.

- Basándonos en este estudio, la espectroscopia Raman es un instrumento apropiado para el estudio de Fe(III) óxidos, oxihidróxidos y oxihidrosulfatos y puede reemplazar el análisis XRD. Aunque la espectroscopia Raman es una técnica bien conocida, no está consolidada en el estudio de precipitados de Fe(III) en medios AMD. Para estos estudios, la espectroscopia Raman es especialmente apropiada dado que ofrece una detección fácil y fiable a estala mico- o milimétrica de fases, como la schwertmanita, que son difíciles de identificar en muestras *bulk* con paragénesis multimineral. Sin embargo, XRD ofrece una estimación de ratios relativamente minerales que la espectroscopia Raman no es capaz de hacer. Ain así, en el caso de la schwertmanita es un rato incluso con XRD dada su baja cristalinidad.

- En lo que se refiere al destino a largo plazo de los principales contaminantes retenidos en las terrazas Fe formadas a lo largo de cuencas afectadas por AMD: estudios exhaustivos que incluyen la digestión química, la espectroscopia Raman, análisis de microsonda, y fluorescencia de rayos-X con radiación sincrotrón se realizaron en muestras de terrazas de Fe tomadas de cursos fluviales de la Faja Pirítica Ibérica (Sur-Oeste de la Península Ibérica). Las muestras se tomaron de terrazas moderas en formación, y terrazas antiguas aisladas por la migración del río a lo largo del tiempo. La schwertmannita era la fase principal y recientemente formada precipitada en el agua contaminada y se posa en la parte superior de las terrazas modernas. Esta schwertmannita fresca está alta y positivamente correlacionada con el As, así como con Cu, Mn, S, y Zn, lo que indica que esta fase controló el consumo de estos elementos. Sin embargo, la maduración progresiva de la schwertmannita en goethita en la parte más profunda de las terrazas modernas, y especialmente en las terrazas antiguas, parece ser la responsable de la disminución de esta correlación, y por tanto, el aumento de la movilidad de los elementos. Esta pérdida de afinidad con los contaminantes es particularmente evidente en el hematite resultante de la transformación de la goethita en las terrazas antiguas. La distribución espacial del hematite está negativamente correlacionada con la concentración de la mayoría de los elementos traza; Pb fue el único elemento traza en mostrar una mayor afinidad por esta fase cristalina después del envejecimiento. Asimismo, la schwertmannita que retiene los contaminantes es los sedimentos recién formados puede servir como fuente a largo plazo de estos contaminantes en el medio ambiente dada las transformaciones mineralógicas.

- Por último, en este estudio se ha probado la interferencia del As(V) durante la transformación de la schwertmannita en goethita y su recristalización. Además, la cinética de la precipitación la transformación se han calculado a corto, medio y largo plazo con diferente concentraciones de As(V). El arsénico controla los procesos de transformación de las fases, pero también es liberado de su estructura una vez que éstos se convierten en fases más cristalinas. Además, el uso de d-PDF ha permitido detectar las implicaciones a nivel de estructura de la introducción de As en la schwertmannita, incluso formando nuevas fases amorfas en alto $[As]_0$. La removilización del As durante la maduración de sedimentos AMD podría tener grandes implicaciones en el destino a largo plazo de contaminantes relacionados con AMD. Asimismo, esta transformación debe tenerse en consideración en el tratamiento de desperdicios causado por tratamientos pasivos AMD. Sin embargo, se plantea que este estudio puede expandirse para incluir la formación de fases más estables como hematite, para evaluar el comportamiento de los elementos traza durante la completa transformación de precipitados AMD.

A pesar de los estudios realizados durante el desarrollo de esta tesis, existen aún algunas cuestiones relacionadas con el comportamiento de los metales traza durante su diagénesis. Estudios futuros deben subrayar la preparación de nuevas series de experimentos *batch* que pudieran formar hematite de la síntesis de schwertmannita. Sobre todo, es importante enfocar esos estudios en la posible liberación y retención de elementos traza contendidos en los precipitados. Al mismo tiempo, los defectos estructurales deben ser estudiados minuciosamente mediante experimentos sintéticos y naturales. Por otro lado, un posible uso de los desperdicios generados por sistemas de tratamiento pasivos deberían ser diseñados dado que las propuestas actuales pueden removilizar los contaminantes y devolverlos al ciclo natural. Finalmente, se debería insistir en la necesidad de una caracterización rigurosa de las fases pseudo-amorfas detectadas en aquellos experimentos con altas concentraciones de As dada la retención de una parte considerable del As en solución.

APPENDIX

APPENDIX CHAPTER II

Raman Identification of the Fe-precipitates and evaluation of As fate during phase transformation in Tinto and Odiel River Basins

Chemical Geology 398 (2015) 22–31

Contents lists available at ScienceDirect

Chemical Geology

journal homepage: www.elsevier.com/locate/chemgeo

Raman identification of Fe precipitates and evaluation of As fate during phase transformation in Tinto and Odiel River Basins

Annika Parviainen [a,b,*], Pablo Cruz-Hernández [c], Rafael Pérez-López [c], José Miguel Nieto [c], José Manuel Delgado-López [b]

[a] Department of Mineralogy and Petrology, University of Granada, Avda. Fuente Nueva s/n, E-18002 Granada, Spain
[b] Instituto Andaluz de Ciencias de la Tierra (IACT), Avda. de Las Palmeras 4, E-18100 Armilla, Granada, Spain
[c] Department of Geology, University of Huelva, Campus 'El Carmen' s/n, E-21071 Huelva, Spain

ARTICLE INFO

Article history:
Received 3 November 2014
Received in revised form 23 January 2015
Accepted 26 January 2015
Available online 3 February 2015

Editor: J. Fein

Keywords:
Acid Mine Drainage
Iron terraces
Schwertmannite
Goethite
Hematite
Arsenic

ABSTRACT

Newly-formed Fe terrace samples and corresponding water samples of Tinto and Odiel Rivers, as well as, ancient terrace samples representing conditions of ancient Tinto River, were collected and studied by optical microscopy, Raman spectroscopy, X-ray diffraction, scanning electron microscopy, microprobe analysis, pseudo-total digestions, and by chemical analytics. The newly-formed terraces showed that currently schwertmannite is precipitating on the riverbed acting as a sink for arsenic. In a matter of months, this metastable phase transforms into goethite and, eventually, jarosite which are found in the deeper sediments below one centimeter. Due to long-term transformation, well-crystallized goethite and diagenetic hematite were the major phases in the ancient terraces. The microanalyses suggested that goethite retained slightly higher concentrations of As than hematite suggesting that As is mobilized in the transformation process. Additionally, this study shows that Raman spectroscopy is an efficient tool in the mineralogical characterization of Fe(III) oxides, hydroxides, and oxyhydroxysulfates at micro to millimeter scale in these types of samples. However, Raman spectra did not provide insights on the incorporation of As within the crystal lattice of schwertmannite, probably due to its low concentration.

1. Introduction

The outcropping massive sulfides of the Iberian Pyrite Belt (IPB) and the subsequent formation of gossans (thick cap of iron oxides formed as a result of chemical weathering) have influenced the microbiochemistry of the Tinto and Odiel River basins, SW Spain (Nieto et al., 2007, 2013). Sulfide oxidation led to natural Acid Rock Drainage (ARD) over millions of years, and intensive mining since 4500 years ago (Nocete et al., 2014) provoked Acid Mine Drainage (AMD) enhancing the extreme acidic conditions of the river systems. Over prolonged time span a unique microbiochemical environment was created, and iron oxyhydroxides and oxyhydroxysulfates precipitated forming terrace-like iron formations i.e. the precipitates settled as thick, stepped iron accumulations on the riverbed. The ancient Fe terraces are located tens of meters above the current river and they may be as old as several million years (Fernández-Remolar et al., 2005; Essalhi et al., 2011). The Tinto River has been pointed out as a terrestrial analog to iron formations on Early Earth and Meridiani Planum on Mars (Fernández-Remolar et al., 2005).

In AMD-after mining environments, metastable schwertmannite [$Fe_8O_8(OH)_{5.5}(SO_4)_{1.25}$] has proven to be good at scavenging arsenic (AsV) from solution (Acero et al., 2006; Asta et al., 2010). However, over time the schwertmannite tends to transform spontaneously into more crystalline phases such as goethite [α-FeOOH] in a matter of months (Acero et al., 2006). Bigham et al. (1996) describe this reaction:

$$Fe_8O8(OH)_{5.5}(SO_4)_{1.25(s)} + 2.5H_2O \rightarrow 8FeOOH_{(s)} + 1.25SO_4^{2-}{}_{(aq)} + 2.5H^+{}_{(aq)}. \quad (1)$$

The eventual precipitation of jarosite [$KFe_3(SO_4)_2(OH)_6$] is also reported (Acero et al., 2006).

On a longer time scale of centuries, goethite is transformed into hematite [Fe_2O_3] through diagenetic processes (Pérez-López et al., 2011) according to the following reaction described by Langmuir (1971):

$$2FeOOH_{(s)} \rightarrow Fe_2O_{3(s)} + H_2O_{(aq)}. \quad (2)$$

Identifying these phases and quantifying the potentially toxic elements that they may carry by adsorption or co-precipitation are

* Corresponding author at: Department of Mineralogy and Petrology, University of Granada, Avda. Fuente Nueva s/n, E-18002 Granada, Spain.
E-mail addresses: aparviainen@ugr.es (A. Parviainen), pablo.cruz@dgeo.uhu.es (P. Cruz-Hernández), rafael.perez@dgeo.uhu.es (R. Pérez-López), jmnieto@uhu.es (J.M. Nieto), jmdl@ic.csic.es (J.M. Delgado-López).

http://dx.doi.org/10.1016/j.chemgeo.2015.01.022
0009-2541/

Frost, R.L., Wills, R.-A., Weier, M.-L., Martens, W., 2005. Comparison of the Raman spectra of natural and synthetic K- and Na-jarosites at 298 and 77 K. J. Raman Spectrosc. 6, 435–444.
Fukushi, K., Sato, T., Yanase, N., 2003. Solid-solution reactions in As(V) sorption by schwertmannite. Environ. Sci. Technol. 37, 3581–3586.
Fukushi, K., Sato, T., Yanase, N., Minato, J., Yamada, H., 2004. Arsenate sorption on schwertmannite. Am. Mineral. 89, 1728–1734.
Giménez, J., Martínez, M., de Pablo, J., Rovira, M., Duro, L., 2007. Arsenic sorption onto natural hematite, magnetite, and goethite. J. Hazard. Mater. 141, 575–580.
Hubbard, C.G., Stuart Black, S., Coleman, M.L., 2009. Aqueous geochemistry and oxygen isotope compositions of acid mine drainage from the Río Tinto, SW Spain, highlight inconsistencies in current models. Chem. Geol. 265, 321–334.
Langmuir, D., 1971. Particle size effect on the reaction goethite = hematite + water. Am. J. Sci. 271, 147–156.
Leistel, J.M., Marcoux, E., Thiéblemont, D., Quesada, C., Sánchez, A., Almodóvar, G.R., Pascual, E., Sáez, R., 1998. The volcanic-hosted massive sulphide deposits of the Iberian Pyrite Belt review and preface to the thematic issue. Mineral. Deposita 33, 2–30.
Mamindy-Pajany, Y., Hurel, C., Marmier, N., Roméo, M., 2011. Arsenic (V) adsorption from aqueous solution onto goethite, hematite, magnetite and zero-valent iron: effects of pH, concentration and reversibility. Desalination 281, 93–99.
Mazzetti, L., Thistlethwaite, P.J., 2002. Raman spectra and thermal transformations of ferrihydrite and schwertmannite. J. Raman Spectrosc. 33, 104–111.
Müller, K., Ciminelli, V.S.T., Dantas, M.S.S., Willscher, S., 2010. A comparative study of As(III) and As(V) in aqueous solutions and adsorbed on iron oxy-hydroxides by Raman spectroscopy. Water Res. 44, 5660–5672.
Murad, E., 1997. Identification of minor amounts of anatase in kaolins by Raman spectroscopy. Am. Mineral. 82, 203–206.
Nieto, J.M., Sarmiento, A.M., Olías, M., Canovas, C.R., Riba, I., Kalman, J., Delvalls, T.A., 2007. Acid mine drainage pollution in the Tinto and Odiel Rivers (Iberian Pyrite Belt, SW Spain) and bioavailability of the transported metals to the Huelva Estuary. Environ. Int. 33, 445–455.
Nieto, J.M., Sarmiento, A.M., Canovas, C.R., Olías, M., Ayora, C., 2013. Acid mine drainage in the Iberian Pyrite Belt: 1. Hydrochemical characteristics and pollutant load of the Tinto and Odiel Rivers. Environ. Sci. Pollut. Res. 20, 7509–7519.
Nocete, F., Sáez, R., Bayona, M.R., Nieto, J.M., Peramo, A., López, P., Gil-Ibarguchi, J.I., Inácio, N., García, S., Rodríguez, J., 2014. Gold in the southwest of the Iberian Peninsula during the 3rd millennium BC. J. Archaeol. Sci. 41, 691–704.
Pérez-López, R., Asta, M.P., Román-Ross, G., Nieto, J.M., Ayora, C., Tucoulou, R., 2011. Synchrotron-based X-ray study of iron oxide transformations in terraces from the Tinto–Odiel River system: influence on arsenic mobility. Chem. Geol. 280, 336–343.
Sáez, R., Pascual, E., Toscano, M., Almodóvar, G.R., 1999. The Iberian type of volcano-sedimentary massive sulfide deposits. Mineral. Deposita 34, 549–570.
Sarmiento, A.M., Nieto, J.M., Casiot, C., Elbaz-Poulichet, F., Egal, M., 2009. Inorganic arsenic speciation at river basin scales: the Tinto and Odiel Rivers in the Iberian Pyrite Belt, SW Spain. Environ. Pollut. 157, 1202–1209.
Tornos, F., 2006. Environment of formation and styles of volcanogenic massive sulfides: the Iberian Pyrite Belt. Ore Geol. Rev. 28, 259–307.

APPENDIX CHAPTER III

Trace element-mineral association in modern and ancient iron terraces in acid drainage environments

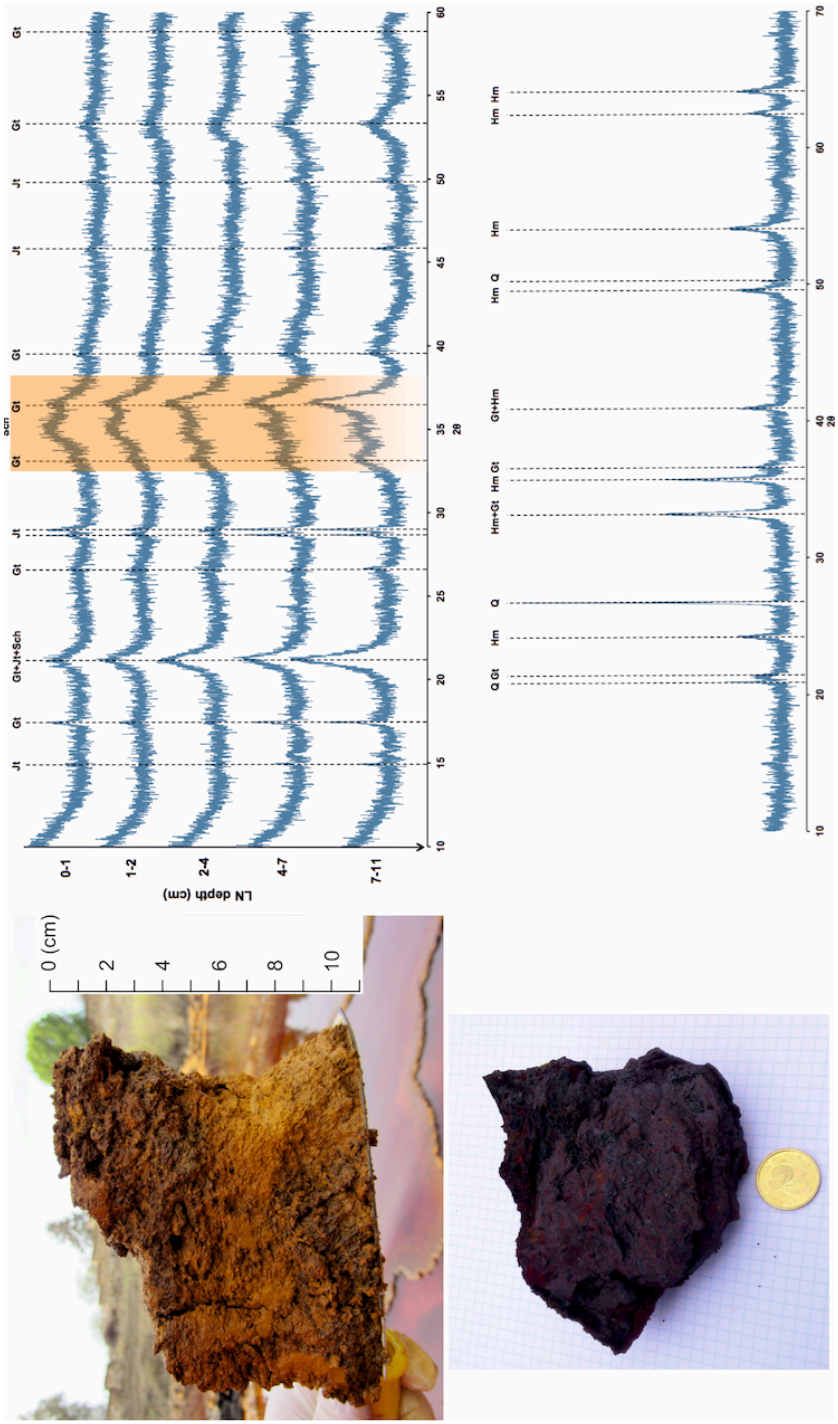

Natural samples (modern and ancient terraces) and XRD patterns. The fresh terrace has been separated in levels to perform differentiated XRD analysis by depths

	PC1	PC2	PC3	PC4	PC5	PC6	PC7	PC8	PC9
Schwertmannite in modern terrace									
Cumulative % of variance	71	84	91	96	98	100			
As	0.909	-0.117	0.037	0.217	-0.290	-0.167			
Fe	0.951	-0.050	0.053	0.101	-0.163	0.229			
Cu	0.846	0.154	-0.178	0.325	0.349	-0.018			
Zn	0.818	0.685	-0.156	-0.282	-0.073	-0.023			
Mn	0.683	-0.451	-0.387	-0.319	0.060	-0.016			
S	0.832	-0.087	0.566	-0.217	0.165	-0.033			
Schwertmannite and goethite in modern terrace									
Cumulative % of variance	74	88	94	97	99	100			
As	0.819	0.136	-0.108	0.503	-0.210	-0.048			
Fe	0.958	-0.033	-0.050	0.009	0.118	0.254			
Cu	0.825	0.222	0.571	-0.139	-0.098	-0.032			
Zn	0.705	0.731	0.081	-0.028	-0.088	-0.031			
Mn	0.689	-0.305	-0.080	0.013	0.427	-0.132			
S	0.627	-0.0 49	-0.366	-0.376	-0.220	-0.048			
Goethite in ancient terrace									
Cumulative % of variance	43	62	72	81	88	93	96	99	100
As	0.312	0.488	-0.162	0.818	0.251	0.056	-0.031	0.051	-0.009
Fe	0.845	-0.107	0.009	-0.049	-0.097	0.017	0.042	0.022	0.284
Cu	-0.695	-0.356	0.062	-0.071	0.295	0.097	0.049	-0.277	0.004
Zn	-0.157	-0.239	0.085	-0.088	0.035	-0.051	-0.077	0.365	-0.051
Mn	-0.510	-0.535	0.809	-0.180	0.336	0.081	0.013	0.070	0.007
S	-0.088	0.682	0.067	-0.049	-0.241	0.466	-0.053	-0.035	-0.107
Hematite in ancient terrace									
Cumulative % of variance	46	69	85	91	94	96	98	99	100
As	0.830	-0.092	-0.041	-0.395	0.349	0.145	-0.026	0.040	-0.017
Fe	-0.367	-0.688	-0.046	-0.061	-0.064	-0.044	0.013	-0.051	0.174
Cu	0.582	0.257	0.197	0.111	0.166	-0.222	-0.089	0.013	0.006
Zn	-0.336	0.488	0.177	0.083	-0.153	0.278	0.097	-0.028	-0.009
Mn	0.126	0.113	0.778	0.423	0.152	0.051	0.020	-0.018	0.009
S	0.520	0.517	0.014	-0.044	-0.035	-0.168	0.313	0.027	-0.061

Principal component loadings of elements in each analysis shown in Figure 3.6.

Catena 147 (2016) 386–393

Contents lists available at ScienceDirect

Catena

journal homepage: www.elsevier.com/locate/catena

Trace element-mineral associations in modern and ancient iron terraces in acid drainage environments

Pablo Cruz-Hernández [a,*], Rafael Pérez-López [a], Annika Parviainen [b], Matthew B.J. Lindsay [c], José M. Nieto [a]

[a] Department of Earth Sciences, University of Huelva, Campus 'El Carmen', Huelva E-21071, Spain
[b] Andalusian Institute of Earth Sciences, CSIC–UGR, Avda. de las Palmeras 4, Armilla, Granada, Spain
[c] Department of Geological Sciences, University of Saskatchewan, Saskatoon, SK, S7N 5E2, Canada

ARTICLE INFO

Article history:
Received 29 April 2016
Received in revised form 14 July 2016
Accepted 27 July 2016
Available online 31 July 2016

Keywords:
Schwertmannite
Goethite
Hematite
Acid drainage
Trace elements behavior

ABSTRACT

Iron-rich sediments commonly cover riverbeds that have been affected by acid drainage associated with sulfide-mineral oxidation. Freshly-formed precipitates correspond to poorly-crystalline oxyhydroxysulfates that recrystallize over time. This study examined the distribution and mineral association of trace elements (e.g., As, Cu, Zn) in modern and ancient (~6 Ma) Fe terraces in the Tinto river basin, Spain. The mineral composition of the terraces was determined by Raman μ-spectroscopy. Chemical digestions, electron probe microanalyses, and synchrotron-based μ-X-ray fluorescence mapping were used to examine As, Cu, and Zn distribution and corresponding mineral associations. Fresh precipitates at modern terrace surfaces were dominated by schwertmannite, which contained high As, Cu, Mn, and Zn concentrations. However, schwertmannite transforms into goethite over days to weeks in the deeper part of the current terraces and into hematite over centuries. Affinity for trace elements was generally highest for schwertmannite and lowest for hematite, which suggests that their retention by Fe terraces decreases during mineral transformation. Hence, schwertmannite acts as temporary sink for contaminants, which are again released over long time periods. These findings should be considered for management and treatment of possible water resources affected by acid mine drainage.

1. Introduction

The natural weathering of outcropping sulfide ore bodies under meteoric conditions often produces acid rock drainage (ARD). Oxidative dissolution of sulfide minerals can lead to widespread acidification and contamination of water resources. Acid mine drainage (AMD) is generated where sulfide-mineral oxidation is accelerated, such as in mining operations that include excavations, earth works, and waste deposits. The consequences of AMD are generally more severe than ARD because mining activities increase exposed surface area of sulfide-bearing rocks (Amos et al., 2015; Lindsay et al., 2015; Olías et al., 2004; Webster et al., 1998). Dissolution of pyrite [FeS_2] and other sulfides in the presence of oxygen and water releases Fe(II) and SO_4, and generates protons causing acidification of waters. Potentially hazardous trace elements (e.g., As, Cu, Zn) associated to sulfides are also liberated during oxidative dissolution. Subsequent oxidation of Fe(II) can promote spontaneous precipitation of Fe(III) oxyhydroxides and oxyhydroxysulfates from acid-sulfate waters. These waters host extremophile bacterial species such as *Thiobacillus ferrooxidans* and *Leptospirillum ferrooxidans* that catalyze Fe(II) oxidation and accelerate subsequent precipitation reactions (Boon and Heijnen, 1998; Leduc et al., 2002).

Schwertmannite [$Fe_{16}O_{16}(OH)_{12}(SO_4)_2$] is thought to initially be the most thermodynamically stable phase in AMD impacted waters (Bigham et al., 1996). This poorly-crystalline oxyhydroxysulfate phase has a high capacity to sequester As and other potentially hazardous trace elements (Fernandez-Martinez et al., 2010; Fukushi et al., 2003, 2004). However, schwertmannite is metastable and transforms at pH 2–3 into more crystalline phases such as goethite [FeO(OH)] and jarosite [$KFe_3(SO_4)_2(OH)_6$] within weeks (Bigham et al., 1996; Davidson et al., 2008). The pH regimes often favor goethite over jarosite precipitation because jarosite forms at lower pH and higher Fe(III) concentrations (Acero et al., 2006). Goethite can subsequently transform into hematite [Fe_2O_3] over the centuries through diagenetic processes (Davidson et al., 2008; Langmuir, 1971). Some studies have pointed out that transformation rates could be affected by high concentrations of trace elements. While the overall rate of schwertmannite transformation to more stable phases decreases with increasing arsenate (Fukushi et al., 2003) and, to a lesser extent, chromate (Regenspurg and Peiffer, 2005) loading, the apparent rate of hematite formation increases in the presence of these ions (Ford, 2002).

Formation of Fe terraces within AMD impacted rivers begins with accumulation and consolidation of schwertmannite on riverbeds (Cáceres et al., 2013). Transformation of schwertmannite into goethite, jarosite, and hematite has previously been observed in Fe terraces within AMD-impacted rivers (Asta et al., 2010; Parviainen et al., 2015;

* Corresponding author.
E-mail address: pablo.cruz@dgeo.uhu.es (P. Cruz-Hernández).

http://dx.doi.org/10.1016/j.catena.2016.07.049
0341-8162/

Acknowledgments

This research was financed by the Spanish Ministry of Economy and Competitiveness through the EMPATIA project (Ref. CGL2013-48460-C2-1-R). The work of Dr. A. Parviainen was funded by the KAUTE Foundation, Finland. Dr. R. Pérez-López acknowledges the Spanish Ministry of Science and Innovation and the "Ramón y Cajal Subprogramme" (MICINN-RYC 2011). P. Cruz-Hernández was supported by a graduate scholarship from the Spanish Ministry of Economy and Competitiveness (METODICA, CGL2010-21956-C02-02). Dr. Lindsay acknowledges support from the NSERC Discovery Grants Program (Grant No. RGPIN-2014-06589). Portions of this research were performed at GeoSoilEnviroCARS (Sector 13), Advanced Photon Source (APS), Argonne National Laboratory. GeoSoilEnviroCARS is supported by the National Science Foundation - Earth Sciences (EAR-1128799) and Department of Energy - GeoSciences (DE-FG02-94ER14466). This research used resources of the Advanced Photon Source, a U.S. Department of Energy (DOE) Office of Science User Facility operated for the DOE Office of Science by Argonne National Laboratory under Contract No. DE-AC02-06CH11357. We would also like to thank Dr. Markus Egli (Editor) and two anonymous reviewers for the support and comments that significantly improved the quality of the original paper.

Appendix A. Supplementary data

Supplementary data to this article can be found online at http://dx.doi.org/10.1016/j.catena.2016.07.049.

References

Acero, P., Ayora, C., Torrentó, C., Nieto, J.M., 2006. The behavior of trace elements during schwertmannite precipitation and subsequent transformation into goethite and jarosite. Geochim. Cosmochim. Acta 70, 4130–4139. http://dx.doi.org/10.1016/j.gca.2006.06.1367.

Amils, R., González-Toril, E., Fernández-Remolar, D., Gómez, F., Aguilera, Á., Rodríguez, N., Malki, M., García-Moyano, A., Fairén, A.G., de la Fuente, V., Luis Sanz, J., 2007. Extreme environments as Mars terrestrial analogs: the Rio Tinto case. Planet. Space Sci. 55, 370–381. http://dx.doi.org/10.1016/j.pss.2006.02.006.

Amos, R.T., Blowes, D.W., Bailey, B.L., Sego, D.C., Smith, L., Ritchie, I.M., 2015. Waste-rock hydrogeology and geochemistry. Appl. Geochem. 57, 140–156. http://dx.doi.org/10.1016/j.apgeochem.2014.06.020.

Asta, M.P., Ayora, C., Román-Ross, G., Cama, J., Acero, P., Gault, A.G., Charnock, J.M., Bardelli, F., 2010. Natural attenuation of arsenic in the Tinto Santa Rosa acid stream (Iberian Pyritic Belt, SW Spain): the role of iron precipitates. Chem. Geol. 271, 1–12. http://dx.doi.org/10.1016/j.chemgeo.2009.12.005.

Bigham, J.M., Schwertmann, U., Traina, S.J., Winland, R.L., Wolf, M., 1996. Schwertmannite and the chemical modeling of iron in acid sulfate waters. Geochim. Cosmochim. Acta 60, 2111–2121. http://dx.doi.org/10.1016/0016-7037(96)00091-9.

Boon, M., Heijnen, J., 1998. Chemical oxidation kinetics of pyrite in bioleaching processes. Hydrometallurgy 48, 27–41. http://dx.doi.org/10.1016/S0304-386X(97)00072-8.

Bowell, R.J., 1994. Sorption of arsenic by iron oxides and oxyhydroxides in soils. Appl. Geochem. 9, 279–286.

Burton, E.D., Bush, R.T., Johnston, S.G., Watling, K.M., Hocking, R.K., Sullivan, L.A., Parker, G.K., 2009. Sorption of arsenic(V) and arsenic(III) to schwertmannite. Environ. Sci. Technol. 43, 9202–9207. http://dx.doi.org/10.1021/es902461x.

Cáceres, L.M., Ollas, M., De Andrés, J.R., Rodríguez-Vidal, J., Clemente, L., Galván, L., Medina, B., 2013. Geochemistry of quaternary sediments in terraces of the Tinto River (SW Spain): paleoenvironmental implications. Catena 101, 1–10. http://dx.doi.org/10.1016/j.catena.2012.09.011.

Courtin-Nomade, A., Bril, H., Neel, C., Lenain, J.-F., 2003. Arsenic in iron cements developed within tailings of a former metalliferous mine—Enguialès, Aveyron, France. Appl. Geochem. 18, 395–408. http://dx.doi.org/10.1016/S0883-2927(02)00098-7.

Das, S., Hendry, M.J., 2011. Application of Raman spectroscopy to identify iron minerals commonly found in mine wastes. Chem. Geol. 290, 101–108. http://dx.doi.org/10.1016/j.chemgeo.2011.08.001.

Davidson, L.E., Shaw, S., Benning, L.G., 2008. The kinetics and mechanisms of schwertmannite transformation to goethite and hematite under alkaline conditions. Am. Mineral. 93, 1326–1337. http://dx.doi.org/10.2138/am.2008.2761.

Essalhi, M., Sizaret, S., Barbanson, L., Chen, Y., Lagroix, F., Demory, F., Nieto, J.M., Sáez, R., Capitán, M.Á., 2011. A case study of the internal structures of gossans and weathering processes in the Iberian Pyrite Belt using magnetic fabrics and paleomagnetic dating. Miner. Deposita 46, 981–999. http://dx.doi.org/10.1007/s00126-011-0361-8.

Fernandez-Martinez, A., Timon, V., Romaman-Ross, G., Cuello, G.J., Daniels, J.E., Ayora, C., 2010. The structure of schwertmannite, a nanocrystalline iron oxyhydroxysulfate. Am. Mineral. 95, 1312–1322. http://dx.doi.org/10.2138/am.2010.3446.

Fernández-Remolar, D.C., 2008. Geological record of an acidic environment driven by iron hydrochemistry: the Tinto River system. J. Geophys. Res. 108, 1–15. http://dx.doi.org/10.1029/2002JE001918.

Filippi, M., Doušová, B., Machovič, V., 2007. Mineralogical speciation of arsenic in soils above the Mokrsko-west gold deposit, Czech Republic. Geoderma 139, 154–170. http://dx.doi.org/10.1016/j.geoderma.2007.01.015.

Ford, R.G., 2002. Rates of hydrous ferric oxide crystallization and the influence on coprecipitated arsenate. Environ. Sci. Technol. 36, 2459–2463. http://dx.doi.org/10.1021/es015768d.

Frost, R.L., Wills, R.A., Weier, M.L., Martens, W., 2005. Comparison of the Raman spectra of natural and synthetic K- and Na-jarosites at 298 and 77 K. J. Raman Spectrosc. 36, 435–444. http://dx.doi.org/10.1002/jrs.1317.

Fukushi, K., Sato, T., Yanase, N., 2003. Solid-solution reactions in As(V) sorption by schwertmannite. Environ. Sci. Technol. 37, 3581–3586. http://dx.doi.org/10.1021/es0264278.

Fukushi, K., Sato, T., Yanase, N., Minato, J., Yamada, H., 2004. Arsenate sorption on schwertmannite. Am. Mineral. 89, 1728–1734.

Gimenez, J., Martinez, M., de Pablo, J., Rovira, M., Duro, L., 2007. Arsenic sorption onto natural hematite, magnetite, and goethite. J. Hazard. Mater. 141, 575–580. http://dx.doi.org/10.1016/j.jhazmat.2006.07.020.

Langmuir, D., 1971. Particle size effect on the reaction goethite — hematite + water.pdf. Am. J. Sci.

Leduc, D., Leduc, L.G., Ferroni, G.D., 2002. Quantification of bacterial populations indigenous to acidic drainage streams. Water Air Soil Pollut. 135, 1–21. http://dx.doi.org/10.1023/A:1014778301817.

Lindsay, M.B.J., Moncur, M.C., Bain, J.G., Jambor, J.L., Ptacek, C.J., Blowes, D.W., 2015. Geochemical and mineralogical aspects of sulfide mine tailings. Appl. Geochem. 57, 157–177. http://dx.doi.org/10.1016/j.apgeochem.2015.01.009.

Liu, H., Chen, T., Frost, R.L., 2014. An overview of the role of goethite surfaces in the environment. Chemosphere 103, 1–11. http://dx.doi.org/10.1016/j.chemosphere.2013.11.065.

Macías, F., Caraballo, M.A., Rotting, T.S., Pérez-López, R., Nieto, J.M., Ayora, C., 2012. From highly polluted Zn-rich acid mine drainage to non-metallic waters: implementation of a multi-step alkaline passive treatment system to remediate metal pollution. Sci. Total Environ. 433, 323–330. http://dx.doi.org/10.1016/j.scitotenv.2012.06.084.

Mamindy-Pajany, Y., Hurel, C., Marmier, N., Roméo, M., 2011. Arsenic (V) adsorption from aqueous solution onto goethite, hematite, magnetite and zero-valent iron: effects of pH, concentration and reversibility. Desalination 281, 93–99. http://dx.doi.org/10.1016/j.desal.2011.07.046.

Mazzetti, L., Thistlethwaite, P.J., 2002. Raman spectra and thermal transformations of ferrihydrite and schwertmannite. J. Raman Spectrosc. 33, 104–111. http://dx.doi.org/10.1002/jrs.830.

Müller, K., Ciminelli, V.S.T., Dantas, M.S.S., Willscher, S., 2010. A comparative study of As(III) and As(V) in aqueous solutions and adsorbed on iron oxy-hydroxides by Raman spectroscopy. Water Res. 44, 5660–5672. http://dx.doi.org/10.1016/j.watres.2010.05.053.

Newville, M.G., 2001. IFEFFIT: interactive XAFS analysis and FEFF fitting. J. Synchrotron Radiat. 8, 322–324. http://dx.doi.org/10.4135/9781412983846.

Nieto, J.-M., Sarmiento, A.M., Cánovas, C.R., Ollas, M., Ayora, C., 2013. Acid mine drainage in the Iberian Pyrite Belt: 1. Hydrochemical characteristics and pollutant load of the Tinto and Odiel rivers. Environ. Sci. Pollut. Res. Int. 20, 7509–7519. http://dx.doi.org/10.1007/s11356-013-1634-9.

Nocete, F., Sáez, R., Bayona, M.R., Nieto, J.M., Peramo, A., López, P., Gil-Ibarguchi, J.I., Inácio, N., García, S., Rodríguez, J., 2014. Gold in the southwest of the Iberian Peninsula during the 3rd millennium BC. J. Archaeol. Sci. 41, 691–704. http://dx.doi.org/10.1016/j.jas.2013.10.006.

Ollas, M., Nieto, J.M., Sarmiento, A.M., Cerón, J.C., Cánovas, C.R., 2004. Seasonal water quality variations in a river affected by acid mine drainage: the Odiel River (south west Spain). Sci. Total Environ. 333, 267–281. http://dx.doi.org/10.1016/j.scitotenv.2004.05.012.

Ollas, M., Nieto, J.M., Pérez-López, R., Cánovas, C.R., Macías, F., Sarmiento, A.M., Galván, L., 2016. Controls on acid mine water composition from the Iberian Pyrite Belt (SW Spain). Catena 137, 12–23. http://dx.doi.org/10.1016/j.catena.2015.08.018.

Parviainen, A., Cruz-Hernández, P., Pérez-López, R., Nieto, J.M., Delgado-López, J.M., 2015. Raman identification of Fe precipitates and evaluation of As fate during phase transformation in Tinto and Odiel River basins. Chem. Geol. 398, 22–31. http://dx.doi.org/10.1016/j.chemgeo.2015.01.022.

Pérez-López, R., Asta, M.P., Román-Ross, G., Nieto, J.M., Ayora, C., Tucoulou, R., 2011. Synchrotron-based X-ray study of iron oxide transformations in terraces from the Tinto-Odiel river system: influence on arsenic mobility. Chem. Geol. 280, 336–343. http://dx.doi.org/10.1016/j.chemgeo.2010.11.021.

Regenspurg, S., Peiffer, S., 2005. Arsenate and chromate incorporation in schwertmannite. Appl. Geochem. 20, 1226–1239. http://dx.doi.org/10.1016/j.apgeochem.2004.12.002.

Sáez, R., Pascual, E., Toscano, M., Almodóvar, G.R., 1999. The Iberian type of volcano-sedimentary massive sulphide deposits. Miner. Deposita 34, 549–570. http://dx.doi.org/10.1007/s001260050220.

Sarmiento, A.M., Ollas, M., Nieto, J.M., Cánovas, C.R., Delgado, J., 2009. Natural attenuation processes in two water reservoirs receiving acid mine drainage. Sci. Total Environ. 407, 2051–2062. http://dx.doi.org/10.1016/j.scitotenv.2008.11.011.

Solé, V.A., Papillon, E., Cotte, M., Walter, P., Susini, J., 2007. A multiplatform code for the analysis of energy-dispersive X-ray fluorescence spectra. Spectrochim. Acta B At. Spectrosc. 62, 63–68. http://dx.doi.org/10.1016/j.sab.2006.12.002.

Webster, J.G., Swedlund, P.J., Webster, K.S., 1998. Trace metal adsorption onto an acid mine drainage iron (III) oxy hydroxy sulfate. Environ. Sci. Technol. 32, 1361–1368. http://dx.doi.org/10.1021/es9704390.

APPENDIX CHAPTER IV

The role of As(V) in the precipitation and ageing rates of iron oxides of acid mine drainage

No As	0	1	2	4	8	12	24	48	120	240	384	504	1800	3600
As	0	n.d.	n.d.	n.d.	n.d.	n.d.	n.d.	n.d.	n.d.	n.d.	n.d.	n.d.	n.d.	n.d.
Fe	8,98	8,88	8,57	8,43	7,56	6,72	6,31	5,91	4,81	4,36	3,93	3,18	1,70	1,70
S	15,0	14,7	14,4	14,1	14,0	13,7	13,7	13,7	13,9	13,9	14,0	14,1	14,4	14,6
pH		2,25	2,20	2,19	2,15	2,14	2,06	2,11	1,99	2,14	2,08	2,07	1,79	1,64
CE	mS/cm	2,24	2,37	2,43	2,51	2,51	2,84	2,88	3,94	4,58	5,30	5,02	4,45	4,40
Eh	eV	690	671	681	675	679	665	685	672	636	630	632	631	632

0.05 mM	0	1	2	4	8	12	24	48	120	240	384	504	1800	3600
As	0,06	0,03	0,02	0,01	0,01	0,01	0,01	0,01	0,00	0,00	n.d.	0,00	n.d.	n.d.
Fe	8,98	8,67	8,53	8,25	7,93	7,62	7,72	6,99	5,31	4,74	3,74	4,01	1,88	1,79
S	15,0	14,6	14,2	14,1	14,1	14,1	14,2	14,0	13,9	14,0	13,9	13,9	13,9	13,9
pH		2,27	2,23	2,21	2,16	2,14	2,09	2,13	2,06	1,99	1,95	1,94	1,76	1,68
CE	mS/cm	2,17	2,27	2,35	2,45	2,48	2,77	2,83	3,56	4,15	4,93	4,37	4,49	4,41
Eh	eV	694	691	687	686	686	683	691	679	653	652	664	651	655

0.125 mM	0	1	2	4	8	12	24	48	120	240	384	504	1800	3600
As	0,14	0,07	0,04	0,03	0,02	0,02	0,02	0,01	0,01	0,01	n.d.	0,00	n.d.	n.d.
Fe	8,98	8,80	8,53	8,34	8,01	7,84	7,07	6,37	5,34	5,13	4,94	4,64	2,13	2,02
S	15,0	14,2	14,0	13,9	14,0	13,9	14,2	13,7	11,5	11,5	11,4	11,1	14,0	15,0
pH		2,28	2,24	2,20	2,16	2,15	2,15	2,12	2,12	2,05	2,01	2,04	1,76	1,69
CE	mS/cm	2,13	2,25	2,35	2,45	2,48	2,79	3,02	3,52	3,93	3,91	3,86	4,35	4,28
Eh	eV	693	690	692	696	688	664	688	672	657	658	668	600	630

0.25 mM	0	1	2	4	8	12	24	48	120	240	384	504	1800	3600
As	0,27	0,22	0,18	0,13	0,07	0,05	0,05	0,03	0,02	0,01	0,01	0,01	0,00	n.d.
Fe	8,98	8,87	8,68	8,51	8,21	8,08	8,00	6,71	5,51	5,18	5,03	4,77	3,24	2,49
S	15,0	14,4	14,4	14,0	14,1	13,8	14,2	13,9	13,9	14,1	14,3	14,5	14,5	14,2
pH		2,34	2,32	2,29	2,22	2,20	2,18	2,13	2,15	2,10	2,06	2,13	1,85	1,72
CE	mS/cm	1,92	1,95	2,04	2,24	2,34	2,64	2,78	3,23	3,81	4,04	3,76	3,50	3,32
Eh	eV	694	693	691	690	690	679	685	674	652	658	659	653	654

0.5 mM	0	1	2	4	8	12	24	48	120	240	384	504	1800	3600
As	0,54	0,33	0,31	0,29	0,27	0,25	0,20	0,14	0,09	0,06	0,04	0,04	0,00	0,00
Fe	8,98	8,92	8,90	8,81	8,51	8,26	7,80	7,32	6,13	5,81	5,66	5,61	4,94	5,19
S	15,0	14,3	14,3	14,5	14,3	13,6	14,3	14,1	11,7	11,6	11,3	11,5	13,9	13,6
pH		2,34	2,34	2,33	2,30	2,28	2,22	2,19	2,23	2,12	2,09	2,16	1,97	1,85
CE	mS/cm	1,96	1,94	1,93	1,95	1,97	2,29	2,46	2,94	3,21	3,24	3,11	2,78	2,64
Eh	eV	694	689	689	690	691	681	673	672	663	661	669	612	648

1 mM	0	1	2	4	8	12	24	48	120	240	384	504	1800	3600
As	1,06	0,37	0,36	0,33	0,31	0,31	0,29	0,24	0,20	0,14	0,11	0,11	0,07	0,09
Fe	8,98	8,95	8,87	8,71	8,45	8,33	7,75	7,52	6,57	6,45	6,43	6,26	5,82	6,02
S	15,0	14,2	13,8	14,1	14,0	14,2	14,2	13,9	11,5	11,6	11,2	11,4	14,0	13,6
pH		2,31	2,29	2,29	2,27	2,28	2,24	2,25	2,29	2,34	2,24	2,28	2,07	1,96
CE	mS/cm	2,15	2,12	2,11	2,10	2,07	2,28	2,34	2,55	2,69	2,95	2,61	2,32	2,21
Eh	eV	692	689	690	690	691	686	684	660	651	654	657	664	661

No As	0	1	2	4	8	12	24	48	120	240	384	504	960	1800
As	0	n.d.	n.d.	n.d.	n.d.	n.d.	n.d.	n.d.	n.d.	n.d.	n.d.	n.d.	n.d.	n.d.
Fe	8,98	5,57	5,37	4,94	4,25	4,05	3,08	2,43	1,20	0,80	0,46	0,49	0,39	0,35
S	18,7	13,1	13,0	12,9	12,9	12,8	12,7	12,8	13,2	13,6	13,9	13,9	14,1	14,2
pH		2,01	2,02	2,015	2,01	1,95	1,947	1,94	1,81	1,75	1,83	1,77		
CE	mS/cm	3,3	3,3	3,28	3,63	3,83	4,01	4,64	5,38	5,48	5,81	5,83		
Eh	eV	680	678	683	702	683	670	664	624	629	614	603		

0.05 mM	0	1	2	4	8	12	24	48	120	240	384	504	960	1800
As	0,06	0,00	0,00	0,00	0,00	0,00	0,00	0,00	n.d.	n.d.	n.d.	n.d.	n.d.	n.d.
Fe	8,98	5,78	5,41	5,03	4,54	4,13	3,75	3,12	1,34	0,89	0,58	0,50	0,45	0,37
S	18,7	13,7	13,2	13,3	13,1	13,0	12,7	12,5	13,1	13,5	13,9	14,0	14,0	14,2
pH		2,04	2,04	2,03	2,08	2,02	2	1,98	1,85	1,79	1,85	1,8		
CE	mS/cm	3,19	3,25	3,27	3,48	3,58	3,85	4,37	5,22	5,39	5,84	5,71		
Eh	eV	696	696	696	702	692	671	660	637	642	607	608		

0.125 mM	0	1	2	4	8	12	24	48	120	240	384	504	960	1800
As	0,14	0,01	0,01	0,01	0,00	0,00	0,00	0,00	n.d.	n.d.	n.d.	n.d.	n.d.	n.d.
Fe	8,98	5,89	5,65	5,23	4,65	4,08	3,64	3,20	1,78	0,98	0,81	0,72	0,59	0,51
S	18,7	13,6	13,0	12,8	12,7	12,4	11,9	12,5	12,8	13,4	13,7	14,2	14,4	14,5
pH		2,06	2,07	2,06	2,12	2,08	2,01	1,97	1,89	1,75	1,86	1,81		
CE	mS/cm	3,12	3,15	3,25	3,39	3,55	3,78	4,02	4,99	5,42	5,8	6,01		
Eh	eV	697	694	690	697	678	675	677	646	642	611	600		

0.25 mM	0	1	2	4	8	12	24	48	120	240	384	504	960	1800
As	0,27	0,02	0,02	0,01	0,01	0,01	0,00	0,00	0,00	0,00	0,00	0,00	0,00	0,00
Fe	8,98	6,32	5,75	5,40	4,66	4,37	3,76	3,43	2,83	1,81	1,63	1,27	1,10	0,92
S	18,7	13,5	13,1	13,1	12,8	12,0	11,8	12,0	13,1	13,7	14,0	14,2	14,4	14,7
pH		2,09	2,09	2,094	2,14	2,12	2,11	2,01	1,96	1,82	1,9	1,85		
CE	mS/cm	3,03	3,09	3,2	3,31	3,4	3,51	3,73	4,34	4,95	5,35	5,6		
Eh	eV	701	698	696	700	686	684	680	649	651	630	610		

0.5 mM	0	1	2	4	8	12	24	48	120	240	384	504	960	1800
As	0,54	0,08	0,06	0,03	0,02	0,02	0,01	0,01	0,00	0,00	0,01	0,01	0,01	0,02
Fe	8,98	6,95	6,80	5,74	4,95	4,48	4,26	3,84	3,35	2,81	2,30	2,24	2,15	2,05
S	18,7	13,9	13,7	13,4	13,0	12,4	11,9	12,8	13,2	13,5	13,7	13,8	14,0	14,1
pH		2,16	2,12	2,135	2,15	2,02	2,04	2,02	1,99	1,89	1,96	1,84		
CE	mS/cm	2,75	2,91	3,11	3,27	3,36	3,47	3,73	3,99	4,27	4,75	5,12		
Eh	eV	685	675	693	694	687	685	680	648	664	644	630		

1 mM	0	1	2	4	8	12	24	48	120	240	384	504	960	1800
As	1,06	0,13	0,14	0,09	0,07	0,05	0,05	0,05	0,04	0,04	0,05	0,06	0,06	0,07
Fe	8,98	6,64	6,52	5,93	5,27	4,85	4,58	4,03	3,39	2,67	2,32	2,20	2,13	2,00
S	18,7	13,5	13,4	13,1	13,0	12,9	12,7	13,0	13,2	13,4	13,8	14,2	14,4	14,4
pH		2,23	2,2	2,2	2,2	2,09	2,1	2,13	2,08	2,03	2	1,87		
CE	mS/cm	2,37	2,45	2,64	3,03	3,19	3,17	3,12	3,51	3,47	4,58	4,98		
Eh	eV	691	680	692	695	692	690	684	657	665	639	624		

				days	→		1	2	5	10	16	21	40	150	300
No As	**0**	**1**	**2**	**4**	**8**	**12**	**24**	**48**	**120**	**240**	**384**	**504**	**960**	**3600**	**7200**
As	0	n.d.	n.d.	n.d.	n.d.	n.d.	n.d.	n.d.	n.d.	n.d.	n.d.	n.d.	n.d.	n.d.	n.d.
Fe	8,98	1,98	1,94	1,89	1,81	0,90	0,23	0,14	0,083	0,11	0,084	0,094	0,095	0,061	0,057
S	18,7	10,9	10,9	11,0	11,1	11,2	11,3	11,4	11,6	11,8	12,1	12,3	13,5	15,6	16,7
pH		1,81	1,79	1,84	1,85	1,8	1,7	1,71	1,89	1,93	1,96	1,87	1,47	1,55	1,62
EC	mS/cm	4,18	4,3	4,18	4,55	5,1	5,35	5,28	4,98	4,83	4,79	4,86	5,05	5,05	6,63
Eh	eV	690	680	676	683	665	610	602	556	569	562	558	580	614	583

0.05 mM	**0**	**1**	**2**	**4**	**8**	**12**	**24**	**48**	**120**	**240**	**384**	**504**	**960**	**3600**	**7200**
As	0,06	n.d.	n.d.	n.d.	n.d.	n.d.	n.d.	n.d.	n.d.	n.d.	0,00	0,00	0,00	0,00	0,00
Fe	8,98	2,52	2,16	2,70	1,77	1,04	0,31	0,16	0,10	0,13	0,14	0,10	0,07	0,07	0,09
S	18,7	10,7	10,6	11,0	10,9	11,5	11,5	11,7	11,9	12,9	13,3	13,9	14,6	16,0	16,8
pH		1,85	1,89	1,93	1,91	1,86	1,7	1,74	1,82	1,96	2,18	2,08	1,41	1,51	1,62
EC	mS/cm	4,11	4,22	4,07	4,35	4,95	5,33	5,28	5,06	5,2	5,16	5,49	4,9	5,21	6,32
Eh	eV	690	690	690	685	660	625	602	553	540	531	523	590	606	586

0.12 mM	**0**	**1**	**2**	**4**	**8**	**12**	**24**	**48**	**120**	**240**	**384**	**504**	**960**	**3600**	**7200**
As	0,14	0,00	0,00	0,00	0,00	0,00	0,00	0,00	0,00	0,00	0,00	0,00	0,00	0,00	0,00
Fe	8,98	1,93	2,27	2,58	2,61	0,51	0,47	0,23	0,10	0,14	0,14	0,10	0,07	0,09	0,10
S	18,7	10,7	10,7	10,6	10,7	11,3	11,2	11,4	11,9	12,5	13,3	14,0	15,0	15,7	17,0
pH		1,92	1,84	1,86	1,93	1,89	1,77	1,69	2,08	2,08	2,17	2,13	1,37	1,39	1,61
EC	mS/cm	3,92	4,12	3,81	4,03	4,53	5,15	5,34	5,09	5	5,13	5,34	4,77	5,45	6,28
Eh	eV	697	681	691	689	655	640	614	560	553	534	530	594	609	577

0.25 mM	0	1	2	4	8	12	24	48	120	240	384	504	960	3600	7200
As	0,27	0,00	0,00	0,00	0,00	0,00	0,00	0,00	0,00	0,00	0,00	0,00	0,00	0,00	0,00
Fe	8,98	2,28	2,44	2,77	2,02	0,87	1,17	0,30	0,11	0,15	0,11	0,12	0,10	0,12	0,12
S	18,7	10,7	10,6	10,6	10,8	11,1	11,0	11,2	11,6	11,4	11,6	12,3	14,6	16,1	16,9
pH		1,92	1,89	1,95	1,95	1,92	1,8	1,76	1,81	1,88	1,79	1,84	1,35	1,53	1,55
EC	mS/cm	3,84	3,97	3,67	4,1	4,32	4,55	5,3	5,05	4,8	4,67	4,74	4,59	5,02	6,32
Eh	eV	700	690	696	678	663	658	612	557	582	574	566	602	606	580

0.5 mM	0	1	2	4	8	12	24	48	120	240	384	504	960	3600	7200
As	0,54	0,00	0,01	0,01	0,00	0,00	0,00	0,00	0,00	0,01	0,01	0,01	0,01	0,02	0,02
Fe	8,98	2,85	2,76	3,58	1,76	1,18	1,26	0,79	0,15	0,17	0,18	0,13	0,27	0,23	0,18
S	18,7	11,0	11,2	11,3	11,0	11,1	11,2	11,5	11,9	12,4	12,7	13,4	14,6	15,7	16,8
pH		1,98	1,89	2,03	1,97	1,98	1,83	1,82	1,83	2,05	2,13	1,94	1,41	1,47	1,62
EC	mS/cm	3,6	3,61	3,49	4,01	4,18	4,44	4,94	4,99	4,87	4,84	5,42	4,06	5,41	6,45
Eh	eV	695	694	699	686	660	655	630	570	563	549	537	634	621	563

1 mM	0	1	2	4	8	12	24	48	120	240	384	504	960	3600	7200
As	1,06	0,04	0,02	0,04	0,02	0,01	0,01	0,01	0,01	0,00	0,01	0,01	0,02	0,03	0,05
Fe	8,98	3,39	2,57	4,51	3,18	1,33	1,52	0,98	0,30	0,73	0,75	0,34	0,45	0,29	0,34
S	18,7	11,0	11,4	11,4	11,2	11,2	11,1	11,2	11,7	11,6	12,2	12,5	13,4	14,9	16,9
pH		2,05	1,95	2,14	2,01	2,07	1,91	1,86	1,88	1,9	1,86	1,85	1,52	1,6	1,61
EC	mS/cm	3,2	3,47	3,01	3,4	3,9	4,24	4,54	4,75	4,16	4,27	4,34	3,85	4,91	6,15
Eh	eV	687	678	685	684	663	650	640	582	612	598	585	639	591	563

2 mM	0	1	2	4	8	12	24	48	120	240	384	504	960	3600	7200
As	2,18	0,03	0,03	0,04	0,04	0,04	0,04	0,03	0,02	0,02	0,01	0,02	0,04	0,06	0,07
Fe	8,98	2,37	2,75	3,90	2,80	1,28	1,74	1,50	0,34	0,44	0,65	0,35	0,41	0,54	0,70
S	18,7	11,0	10,9	11,1	11,2	10,9	10,7	10,9	11,2	12,3	13,2	13,3	13,5	14,7	16,4
pH		2,07	2,09	2,13	2,06	2,05	1,99	1,98	1,89	2,05	2,3	2,23	1,6	1,64	1,69
EC	mS/cm	3,15	3,08	2,96	3,33	3,73	3,61	3,48	4,12	4,1	4,26	4,98	3,06	4,33	5,05
Eh	eV	691	688	679	672	658	657	650	590	588	560	540	639	598	564

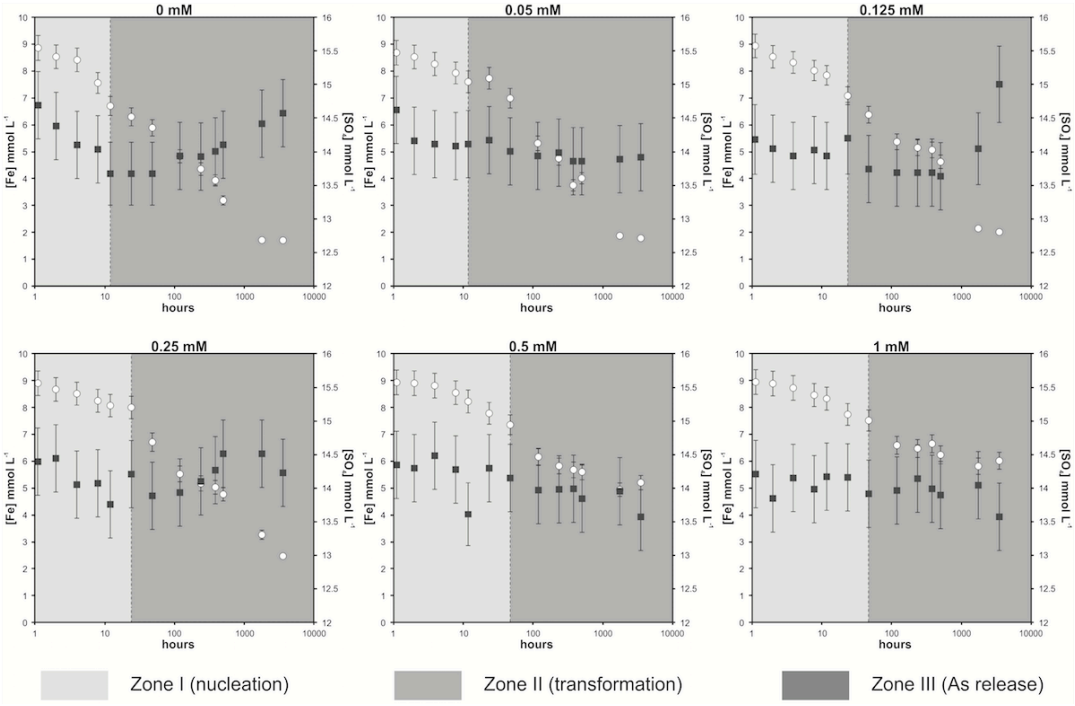

Zone distribution and [Fe] and [SO_4] concentration durind the expriments at 40°C

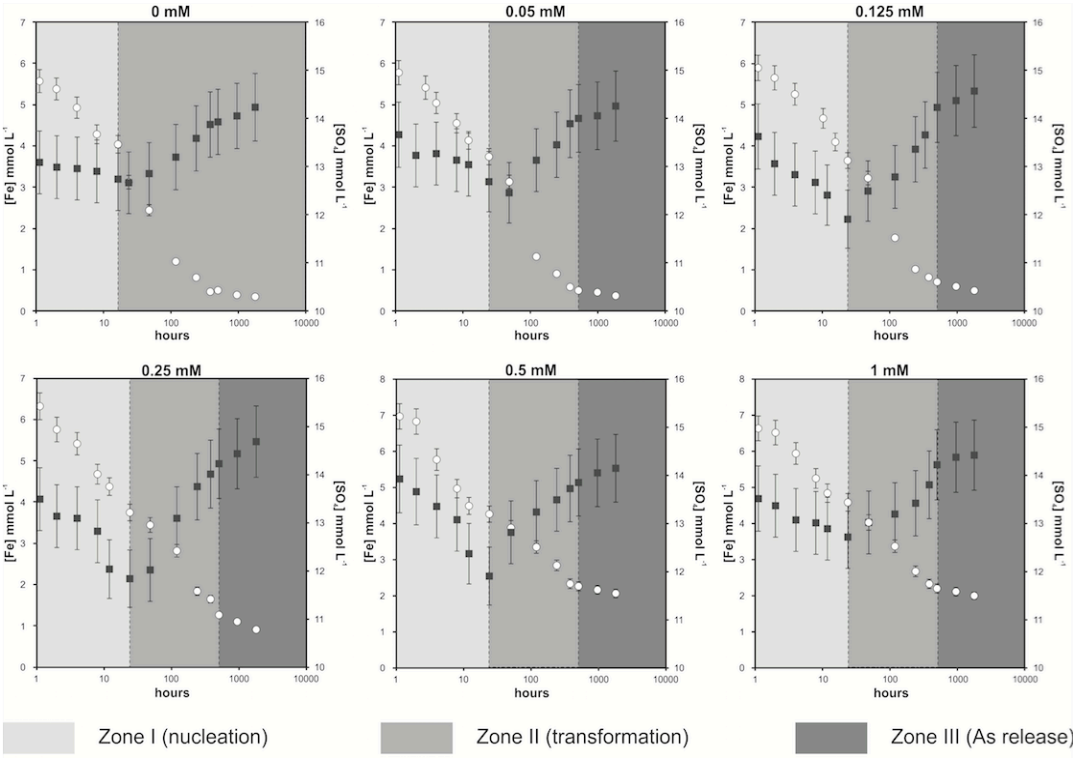

Zone distribution and [Fe] and [SO_4] concentration durind the expriments at 60°C

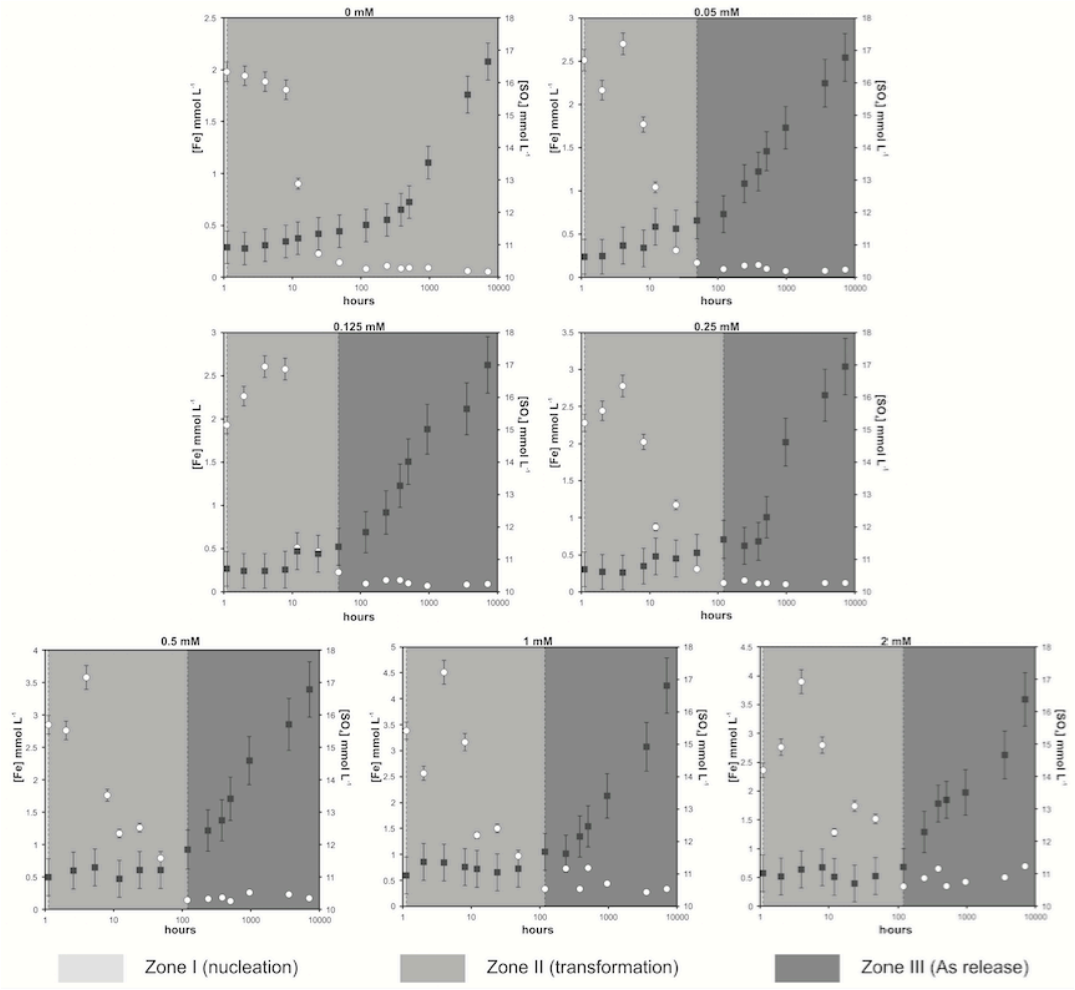

Zone distribution and [Fe] and [SO_4] concentration during expriments at 85°C

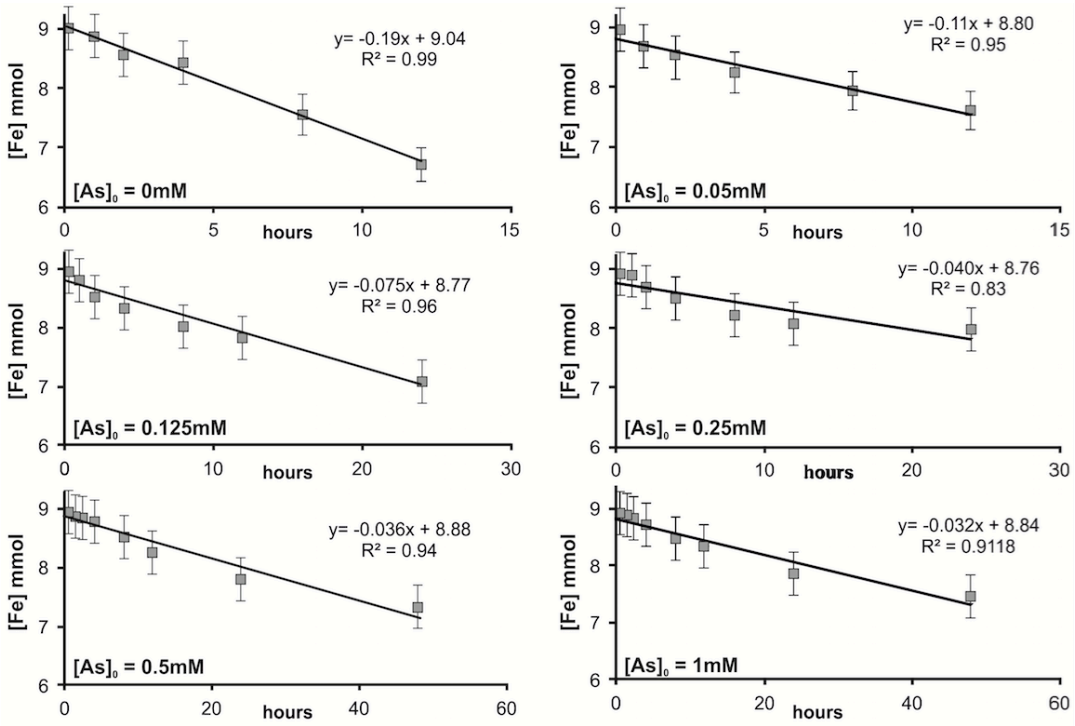

[Fe] during the precipitate period in experiments carried out at 40°C. It has been calculated the precipitation rate based on the trend.

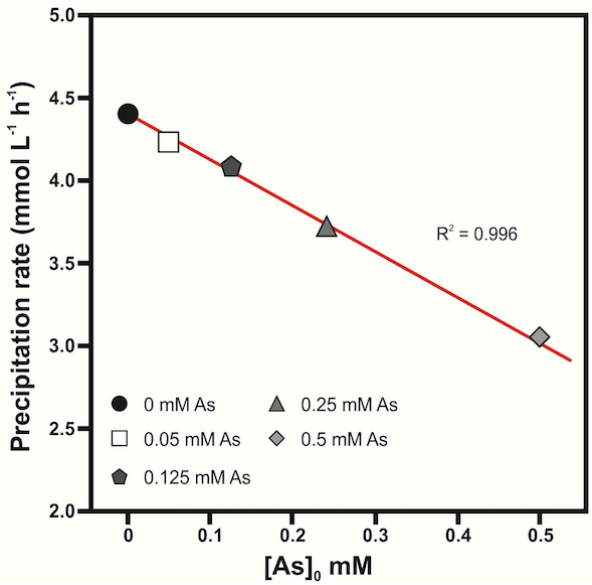

Precipitation rates calculated during the first hour of experiment at 60°C ($[Fe]_0$-$[Fe]_{1hour}$ vs. $[As]_0$)

Available online at www.sciencedirect.com

ScienceDirect

Procedia Earth and Planetary Science 00 (2017) 000–000

Procedia
Earth and Planetary Science

www.elsevier.com/locate/procedia

15th Water-Rock Interaction International Symposium, WRI-15

Role of Arsenic during the Aging of Acid Mine Drainage Precipitates

Pablo Cruz-Hernández[a1], Rafael Peréz-López[a] and José Miguel Nieto[a]

[a]*Department of Geology, University of Huelva, Campus 'El Carmen' s/n, 21071, Huelva, Spain*

Abstract

Iron-rich sediments cover the riverbeds affected by acid mine drainage (AMD) resulting from sulfide mineral oxidation. Precipitates are mainly composed of schwertmannite, which is a poorly-crystalline Fe-oxyhydroxysulfate that recrystallizes over a short-time period to goethite. Schwertmannite precipitation has a strong capacity for removal of some toxic elements like As. This study examines the influence of the initial As(V) concentration on the kinetics of precipitation and transformation of schwertmannite by means of batch experiments. A set of schwertmannites were synthetized with different As concentrations, and solid-solution interactions were allowed at 60ºC during different time periods (from 1 h to 75 d). The increase of the initial As concentration notably the precipitation of schwertmannite and its transformation to goethite. Moreover, the transformation of schwertmannite into goethite entails the release of sulfate and, at a longer time scale, of part of the previously retained As. Thus, As acts as a retardant for schwertmannite transformation; however, this toxic element is released from the precipitates once the schwertmannite is transformed, which is *per se* an environmental paradox. Furthermore, schwertmannite precipitation also plays an important role in the AMD treatment systems; hence, the long-term behavior of these precipitates should be considered for the solid waste management.

Peer-review under responsibility of the organizing committee of WRI-15.

Keywords: acid mine drainage; arsenic; schwertmannite; goethite

* Corresponding author. Tel.: +34-959-239-682; fax: +34-959-219-810.
E-mail address: Pablo.cruz@dgeo.uhu.es

1878-5220
Peer-review under responsibility of the organizing committee of WRI-15.

5. Conclusions

This research has shown the interference of As(V) during schwertmannite transformation into goethite. The remobilization of As during the maturation of the AMD sediments could have important implications in the long-term fate of AMD-related pollutants. In addition, this information must be considered in the management of the wastes obtained in the passive AMD treatments. However, this study plans to be expanded to include the formation of more stable phases such as hematite, to evaluate the behavior of trace elements during the complete transformation of AMD precipitates.

Acknowledgments

The Spanish Ministry of Economy and Competitiveness financed this research through the project EMPATIA (Ref. CGL2013-48460-C2-1-R). Dr. R. Pérez-López acknowledges the Spanish Ministry of Science and Innovation and the 'Ramón y Cajal Subprogramme' (MICINN-RYC 2011). P. Cruz-Hernández was supported by a graduate scholarship from the Spanish Ministry of Economy and Competitiveness (METODICA, CGL2010-21956-C02-02).

References:

1. Bigham, JM, Schwertmann, U, Carlson, L, Murad, E. A poorly crystallized oxyhydroxysulfate of iron formed by bacterial oxidation of Fe(II) in acid mine waters. *Geochim. et Cosmochim. Acta* 1990; **54**: 2743–2758.
2. Fernandez-Martinez, a., Timon, V., Romaman-Ross, G., Cuello, G. J., Daniels, J. E., Ayora, C. The structure of schwertmannite, a nanocrystalline iron oxyhydroxysulfate. *Am. Mineral.* 2010; **95**: 1312–1322.
3. Fukushi, K., Sato, T., Yanase, N. Solid-solution reactions in As(V) sorption by schwertmannite. *Environ. Sci. Technol.* 2003; **37**: 3581–3586.
4. Carrero, S., Pérez-López, R., Fernandez-Martinez, A., Cruz-Hernández, P., Ayora, C., Poulain, A. The potential role of aluminium hydroxysulphates in the removal of contaminants in acid mine drainage. *Chem. Geol.* 2015; **417**: 414–423.
5. Acero, P., Ayora, C., Torrentó, C., Nieto, J. M. The behavior of trace elements during schwertmannite precipitation and subsequent transformation into goethite and jarosite. *Geochim. et Cosmochim. Acta* 2006; **70**: 4130–4139.
6. Ford, R. G. Rates of hydrous ferric oxide crystallization and the influence on coprecipitated arsenate. *Environ. Sci. Technol.* 2002; **36**: 2459–2463.
7. Loan, M., Cowley, J. M., Hart, R., Parkinson, G. M. Evidence on the structure of synthetic schwertmannite. *Am. Mineral.* 2004; **89**: 1735–1742.

OTHER PUBLICATIONS

Science of the Total Environment 481 (2014) 217–231

Contents lists available at ScienceDirect

Science of the Total Environment

journal homepage: www.elsevier.com/locate/scitotenv

Sources of mercury in groundwater and soils of west Gijón (Asturias, NW Spain)

B. González-Fernández [a,*], E. Menéndez-Casares [a], Mónica Meléndez-Asensio [b], Susana Fernández-Menéndez [c], F. Ramos-Muñiz [d], P. Cruz-Hernández [e], A. González-Quirós [a]

[a] Dpto. de Explotación y Prospección de Minas, Universidad de Oviedo, C/Independencia, 13, 33004 Oviedo, Asturias, Spain
[b] Instituto Geológico y Minero de España, C/Matemático Pedrayes, 25, 33005 Oviedo, Asturias, Spain
[c] Dpto. de Geología, Universidad de Oviedo, C/Arias de Velasco, s/n, 33005 Oviedo, Asturias, Spain
[d] Urb. Las Pedreras 25, Vega, 33391 Gijón, Asturias, Spain
[e] Dpto. de Geología, Facultad de Ciencias Experimentales, Avda. Fuerzas Armadas, s/n, 21071 Huelva, Spain

HIGHLIGHTS

- Mercury in Gijón groundwater is not of natural origin.
- Mercury concentration in soils is abnormally high.
- Springs with higher concentrations of Hg have high levels of SO_4.
- Isotopic values of $\delta^{34}S$ and $\delta^{18}O_{SO4}$ indicate an anthropic origin for the sulphate.
- Atmospheric deposition from nearby industries is the most likely source of mercury.

ARTICLE INFO

Article history:
Received 4 October 2013
Received in revised form 7 February 2014
Accepted 7 February 2014
Available online 3 March 2014

Keywords:
Springs
Geochemical backgrounds in soils
Mercury
Sulphate
Isotopes
Soil mercury leachate

ABSTRACT

This work aimed to determine the cause of the presence of high concentrations of mercury in several springs that exhibit a low concentration of metals in the bedrocks of their recharge areas in Gijón, NW Spain and the extent of this contamination. On the basis of geological mapping, different lithological substrata were analysed at the regional scale with the objective of establishing the base level of mercury in natural soils. The mercury content was simultaneously analysed in several water samples, and the following parameters were also determined: major anions and cations, As, Pb, $\delta^{34}S$, and $\delta^{18}O_{SO4}$. The soils of the recharge area of the springs exhibited Hg concentrations that were higher than the base level established for sandstone at the regional level, and four of the total number of springs analysed exhibited Hg concentrations higher than 1 μg/l. In addition, the sulphate concentration exceeded the values that this type of aquifer shows in other parts of the region. A comparison between the regionally geochemical background of soils and mercury concentration in springs and soils of the study area did not exhibit a direct relationship, suggesting an anthropogenic and timely origin (most likely from industrial emissions) for this metal. The $\delta^{34}S$ and $\delta^{18}O_{SO4}$ values of dissolved sulphate from the springs with a higher Hg concentration also indicate an anthropogenic origin.

1. Introduction

On earth, naturally occurring mercury deposits are generally found as Cinnabar (HgS), which is the most important mercury ore. This sulphide mineral ore is abundant at relatively few locations but occurs in small amounts in many rocks. The mercury in rocks steadily contributes small amounts of this metal to the atmosphere and natural waters via weathering processes (Nriagu, 1989). When rock substrata are rich in mercury, mineral soils and sediments may also contain mercury derived from the weathering of parent material. However, most of the mercury present in soils is derived from anthropogenic sources. This mercury could be leached into surface and groundwater from rocks and soils (Wang et al., 2004).

Mercury pollution is a global environmental problem that has serious implications for human health, both immediate and long term. Mercury is considered to be a hazardous substance when present at high concentrations. Currently, human activity is considered the main

* Corresponding author.
E-mail addresses: mbeagf@uniovi.es (B. González-Fernández), ecasares@uniovies (E. Menéndez-Casares), mmelendez@igme.es (M. Meléndez-Asensio), smdez@indurot.uniovi.es (S. Fernández-Menéndez), paco.ramos@telefonica.net (F. Ramos-Muñiz), pablo.cruz@dgeo.uhu.es (P. Cruz-Hernández), andresgquiros@gmail.com (A. González-Quirós).

http://dx.doi.org/10.1016/j.scitotenv.2014.02.034
0048-9697/

Otero XL, Vidal P, Calvo R, Macías F. Trace elements in biodeposits and sediments below from mussel culture in the Ría de Arousa (Galicia- NW Spain). Environ Pollut 2005;136:119–34. http://dx.doi.org/10.1016/j.envpol.2004.11.026.

Pacyna EG, Pacyna JM, Steenhuisen F, Wilson S. Global anthropogenic mercury emission inventory for 2000. Atmos Environ 2006;40:4048–63. http://dx.doi.org/10.1016/j.atmosenv.2006.03.041.

Pirrone N, Costa P, Pacyna JM, Ferrara R. Mercury emissions to the atmosphere from natural and anthropogenic sources in the Mediterranean region. Atmos Environ 2001;35(17):2997–3006. [PII:S1352-2310(01)00103-0].

Pirrone N, Cinnirella S, Feng X, Finkelman RB, Friedli HR, Leaner J, et al. Global mercury emissions to the atmosphere from anthropogenic and natural sources. Atmos Chem Phys 2010;10:5951–64. http://dx.doi.org/10.5194/acp-10-5951-2010.

Praveena SM, Radojevic M, Abdullah MH. The assessment of mangrove sediment quality in Mengkabong Lagoon: an index analysis approach. Int J Environ Sci Educ1306-3065 2007;2(3):60–8. [Detailed computation and interpretation of the above indices have been described by Nude et al. (2011)].

Nude PM, Foli G, Yidana M. Geochemical assessment of impact of mine spoils on the quality of stream sediments within the Obuasi mines environment, Ghana. Int J Geosci 2007;2:259–66.

Ryan PC, Hillier S, Wall AJ. Stepwise effects of the BCR sequential chemical extraction procedure on dissolution and metal release from common ferromagnesian clay minerals: a combined solution chemistry and X-ray powder diffraction study. Sci Total Environ 2008;407(1):603–14. http://dx.doi.org/10.1016/j.scitotenv.2008.09.019.

Selin N, Jacob DJ. Seasonal and spatial patterns of mercury wet deposition in the United States: constraints on the contribution from North American anthropogenic sources. Atmos Environ 2008;42:5193–204. http://dx.doi.org/10.1016/j.atmosenv.2008.02.069.

Tack FMG, Verloo MG. Chemical speciation and fractionation in soil and sediment heavy metal analysis: a review. Int J Environ Anal Chem 1995;59(2):225–38. http://dx.doi.org/10.1080/03067319508041330.

Tessier A, Campbell PGC, Bisson M. Sequential extraction procedure for the speciation of particulate trace metals. Anal Chem 1979;51(7):844–51. http://dx.doi.org/10.1021/ac50043a017.

U.S. Environmental Protection Agency (U.S. EPA). Mercury study report to congress. EPA-452/R-97-003. Washington DC: Office of Air Quality Planning and Standards, Office of Research and Development; 1997.

UNEP. Global mercury assessment. United Nations Environment Programme Chemicals; 2002 [Available at http://www.unep.org/hazardoussubstances/Mercury/MercuryPublications/ReportsPublications/GlobalMercuryAssessmentReportDecember2002/tabid/3617/Default.aspx].

UNEP. Mercury programme. Available inhttp://www.unep.org/hazardoussubstances/Mercury/tabid/434/Default.aspx, 2003.

Wang Q, Kim D, Dionysios DD, Sorial GA, Timberlake D. Sources and remediation for mercury contamination in aquatic systems — a literature review. Environ Pollut 2004;131(2):323–36. http://dx.doi.org/10.1016/j.envpol.2004.01.010.

Chemical Geology 417 (2015) 414–423

Contents lists available at ScienceDirect

Chemical Geology

journal homepage: www.elsevier.com/locate/chemgeo

The potential role of aluminium hydroxysulphates in the removal of contaminants in acid mine drainage

Sergio Carrero [a,*], Rafael Pérez-López [a], Alejandro Fernandez-Martinez [b,c], Pablo Cruz-Hernández [a], Carlos Ayora [d], Agnieszka Poulain [e]

[a] Department of Geology, University of Huelva, Campus 'El Carmen', 21071 Huelva, Spain
[b] CNRS, ISTerre, F-38041 Grenoble, France
[c] Université Grenoble Alpes, ISTerre, F-38041 Grenoble, France
[d] Institute of Environmental Assessment and Water Research, CSIC, Jordi Girona 18, 08034 Barcelona, Spain
[e] ESRF, 71, Avenue des Martyrs, 38043 Grenoble, France

ARTICLE INFO

Article history:
Received 23 February 2015
Received in revised form 4 September 2015
Accepted 13 October 2015
Available online 22 October 2015

Keywords:
Titration
Basaluminite
Schwertmannite
Arsenic
Trace element removal
Acid mine drainage

ABSTRACT

Sorption of trace elements onto poorly-crystalline Al-hydroxysulphate minerals from acid mine drainage (AMD) has received less attention compared to similar Fe(III)-phases because the former are less abundant in many mine drainage environments. In addition, Al-hydroxysulphates precipitate at a higher pH, so their sorption characteristics could be masked or less significant after sorption of trace elements to Fe minerals, which form at lower pH. In this study, oxidation and titration experiments were conducted with Fe(II)-rich AMD solutions under atmospheric and anoxic conditions to elucidate, individually, the sorption capacity of trace elements in solution by Fe and Al-hydroxysulphates. Under atmospheric conditions, precipitation of Fe(III) as schwertmannite, led to total removal of Fe, As, Cr and Pb in solution and 50% of Al. Subsequently, contaminant-depleted solution began to be controlled by precipitation of basaluminite, which acted as an effective sink for the remaining Al, Cu and Si. On the contrary, under anoxic conditions, neutralisation of Fe(II)-rich solutions led first to the basaluminite precipitation, keeping all Fe available in solution and unveiling a heretofore unknown affinity for As and Cr. Basaluminite retains 60% of As in solution compared to 100% removal of As by schwertmannite. However, the sorption capacity of basaluminite is even more significant than that of Fe-phases, considering that Al concentrations in solution were much lower than those of Fe. These findings give new insights into the processes controlling contaminant mobility in anoxic environments (e.g., the bottom of AMD-affected water reservoirs) and pose new opportunities for treatment strategies.

1. Introduction

Contamination of receiving waters and sediments by acid mine drainage (AMD) is one of the main environmental problems associated with mining of sulphide-bearing ore deposits (Nordstrom, 1982a; Nordstrom and Alpers, 1999). These acidic waters have high concentrations of sulphate and metal(oid)es and result from the continuous exposure of sulphide-rich mining wastes, derived mainly from coal fields or massive sulphide ores, to oxygen and water. Pollution by AMD is a serious environmental problem affecting active and abandoned mining areas around the world. Examples of contamination by AMD are described in detail in the Appalachian coalfields (USA) (Powell, 1988; Herlihy et al., 1990), in the Gangreung coalfield (Korea) (Yu and Heo, 2001; Kim and Chon, 2001) and in the Iberian Pyrite Belt (IPB; Iberian Peninsula) (Leblanc et al., 2000; Sáinz et al., 2002; Sarmiento et al., 2009), among many others. The IPB is one of the most strongly AMD-affected areas worldwide (Nieto et al., 2013). In addition, processes that form AMD can operate within mine waste materials long after mining has stopped and AMD leachates can persist for many decades or even centuries after mine operations cease (Younger, 1997).

Acid mine drainage is characterised by high concentrations of sulphate, iron (from sulphide mineral oxidation, mainly pyrite) and aluminium (from weathering of the host rocks), in addition to the presence of other trace elements. In cases with limited oxygen renewal, such as in underground shafts, the emerging acidic water is depleted in oxygen, and thus contains high concentrations of Fe(II). In atmospheric conditions, the presence of oxygen and, mainly, the activity of extremophile microorganisms catalyse the total oxidation of Fe(II) to Fe(III) after a few metres of flow (Nordstrom and Alpers, 1999). Under such conditions, both AMD hydrochemistry and mineralogy are controlled mainly by the SO_4-Fe(III) and SO_4-Al systems (Bigham et al., 1996; Nordstrom and Alpers, 1999).

In AMD-affected streams, high concentrations of ferric iron and sulphate favour the spontaneous precipitation of schwertmannite [$Fe_8O_8(OH)_{(8-2x)}(SO_4)_x \cdot nH_2O$; with x varying from 1 to 1.75], a

* Corresponding author.
E-mail address: sergio.carrero@dgeo.uhu.es (S. Carrero).

http://dx.doi.org/10.1016/j.chemgeo.2015.10.020
0009-2541/

Nieto, J.-M., Sarmiento, A.M., Cánovas, C.R., Olías, M., Ayora, C., 2013. Acid mine drainage in the Iberian Pyrite Belt: 1. Hydrochemical characteristics and pollutant load of the Tinto and Odiel Rivers. Environ. Sci. Pollut. Res. Int. 20, 7509–7519.
Nordstrom, D.K., 1982a. Aqueous pyrite oxidation and the consequent formation of secondary iron minerals. In: Kittrick, J.A., Fanning, D.S., Hossner, L.R. (Eds.), Acid Sulfate Weathering. Soil Science Society of America Publication, pp. 37–56.
Nordstrom, D.K., 1982b. The effect of sulfate on aluminum concentrations in natural waters: some stability relations in the system Al2O3-SO3-H2O at 298 K. Geochim. Cosmochim. Acta 46, 681–692.
Nordstrom, D.K., Alpers, C.N., 1999. Geochemistry of acid mine waters. In: Plumlee, G.S., Logsdon, M. (Eds.), Society & Economic Geologists 6A, pp. 133–160.
Nordstrom, D.K., Wilde, F.D., 1998. Reduction-oxidation potential (electrode method), Section 6.5, Chapter A6. National Field Manual for the Collection of Water-Quality Data, p. 20.
Parkhurst, D.L., Appelo, C.A.J., 1999. User's Guide to PhreeqC (version 2) A Computer Program for Speciation, and Inverse Geochemical Calculations.
Powell, J.D., 1988. Origin and influence of coal mine drainage on streams of the United States. Environ. Geol. Water Sci. 11, 141–152.
Prietzel, J., Mayer, B., 2005. Isotopic fractionation of sulfur during formation of basaluminite, alunite, and natroalunite. Chem. Geol. 215, 525–535.
Randall, S.R., Sherman, D.M., Ragnarsdottir, K.V., 2001. Sorption of As(V) on green rust (Fe4(II)Fe2(III)(OH)12SO4·3H2O) and lepidocrocite (gamma-FeOOH): surface complexes from EXAFS spectroscopy. Geochim. Cosmochim. Acta 65, 1015–1023.
Refait, P., Girault, P., Jeannin, M., Rose, J., 2009. Influence of arsenate species on the formation of Fe(III) oxyhydroxides and Fe(II–III) hydroxychloride. Colloids Surf. A Physicochem. Eng. Asp. 332, 26–35.
Sáinz, A., Grande, J.A., de la Torre, M.L., Sánchez-Rodas, D., 2002. Characterisation of sequential leachate discharges of mining waste rock dumps in the Tinto and Odiel rivers. J. Environ. Manag. 64, 345–353.
Sánchez-España, J., López, P.E., Santofimia, P.E., 2007. The oxidation of ferrous iron in acidic mine effluents from the Iberian Pyrite Belt (Odiel Basin, Huelva, Spain): field and laboratory rates. J. Geochem. Explor. 92, 120–132.
Sánchez-España, J., López, P.E., Santofimia, P.E., Reyes, A.J., Matín, R.J.A., 2006. The removal of dissolved metals by hydroxysulphate precipitates during oxidation and neutralization of acid mine waters, iberian pyrite belt. Aquat. Geochem. 12, 269–298.
Sánchez-España, J., Yusta, I., Diez-Ercilla, M., 2011. Schwertmannite and hydrobasaluminite: a re-evaluation of their solubility and control on the iron and aluminium concentration in acidic pit lakes. Appl. Geochem. 26, 1752–1774.
Sarmiento, A.M., Nieto, J.-M., Olías, M., Cánovas, C.R., 2009. Hydrochemical characteristics and seasonal influence on the pollution by acid mine drainage in the Odiel river Basin (SW Spain). Appl. Geochem. 24, 697–714.
Schwertmann, U., 1984. The influence of aluminium on iron oxides: IX. Dissolution of Al-Goethites in 6 m HCl. Clay Miner. 19, 9–19.
Schwertmann, U., Wolska, E., 1990. The influence of aluminum on iron oxides. XV. Al-for-Fe substitution in synthetic lepidocrocite. Clay Clay Miner. 38, 209–212.
Schwertmann, U., Bigham, J.M., Murad, E., 1995. The first occurrence of schwertmannite in a natural stream environment. Eur. J. Mineral. 7, 547–552.
Singer, P.C., Stumm, W., 1970. Acidic mine drainage: the rate determining step. Science 167, 1121–1123.
Tamura, H., Goto, K., Yotsuyanagi, T., Nagayana, M., 1974. Spectrophotometric determination of iron(II) with 1,10-phenanthroline in the presence of large amounts of iron(III). Talanta 21, 314–318.
Torres, E., Ayora, C., Canovas, C.R., García-Robledo, E., Galván, L., Sarmiento, A.M., 2013. Metal cycling during sediment early diagenesis in a water reservoir affected by acid mine drainage. Sci. Total Environ. 461-462, 416–429.
Tyler, G., Carrasco, R., Nieto, J.-M., Pérez-López, R., Ruiz, M.J., Sarmiento, A.M., 2004. Optimization of major and trace element determination in acid mine drainage samples by ultrasonic nebulizer-ICP-OES (USN-ICP-OES). Pittcon Conference (Chicago, USA) (pp. 9000–1000).
Wagman, D.D., Evans, H.H., Parker, V.B., Schumm, R.H., Harlow, I., Bailey, S.M., Churney, K.L., Butall, R.L., 1982. The NBS Tables of Chemical Thermodynamic Properties. Selected values for inorganic and organic substances in SI units.
Younger, P.L., 1997. The longevity of minewater pollution: a basis for decision-making. Sci. Total Environ. 194-195, 457–466.
Yu, J.Y., Heo, B., 2001. Dilution and removal of dissolved metals from acid mine drainage along Imgok Creek, Korea. Appl. Geochem. 16, 1041–1053.
Yu, J.Y., Heo, B., Choi, I.K., Cho, J.P., Chang, H.W., 1999. Apparent solubilities of schwertmannite and ferrihydrite in natural stream waters polluted by mine drainage. Geochim. Cosmochim. Acta 63, 3407–3416.

Science of the Total Environment 556 (2016) 196–206

Contents lists available at ScienceDirect

Science of the Total Environment

journal homepage: www.elsevier.com/locate/scitotenv

Initial geochemical characteristics of fluid fine tailings in an oil sands end pit lake

Kathryn A. Dompierre [a], Matthew B.J. Lindsay [b,*], Pablo Cruz-Hernández [c], Geoffrey M. Halferdahl [d]

[a] Department of Civil and Geological Engineering, University of Saskatchewan, Saskatoon, Saskatchewan, Canada S7N 5A9
[b] Department of Geological Sciences, University of Saskatchewan, Saskatoon, Saskatchewan S7N 5E2, Canada
[c] Department of Geology, University of Huelva, Campus 'El Carmen', E-21071 Huelva, Spain
[d] Environmental Research and Development, Syncrude Canada Limited, Edmonton, Alberta T6N 1H4, Canada

HIGHLIGHTS

- First study of fluid fine tailings geochemistry in oil sands end pit lake
- Carbonate dissolution has promoted ion exchange reactions.
- Microbial iron and sulfate reduction influence pore-water chemistry.
- Biogeochemical processes have likely enhanced tailings settlement.
- Long-term geochemical evolution of oil sands end pit lakes remains unknown.

GRAPHICAL ABSTRACT

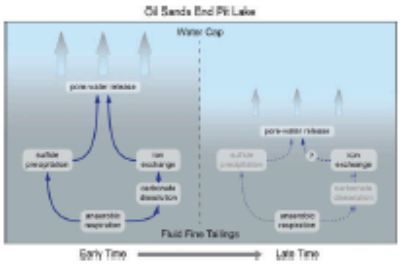

ARTICLE INFO

Article history:
Received 23 November 2015
Received in revised form 2 March 2016
Accepted 2 March 2016
Available online 11 March 2016

Editor: D. Barceló

Keywords:
Oil sands
Tailings
End pit lakes
Process-affected water
Mine closure
Reclamation

ABSTRACT

Geochemical characteristics of fluid fine tailings (FFT) were examined in Base Mine Lake (BML), which is the first full-scale demonstration oil sands end pit lake (EPL) in northern Alberta, Canada. Approximately 186 Mm^3 of FFT was deposited between 1994 and 2012, before BML was established on December 31, 2012. Bulk FFT samples ($n = 588$) were collected in July and August 2013 at various depths at 15 sampling sites. Temperature, solid content, electrical conductivity (EC), pH, Eh and alkalinity were measured for all samples. Detailed geochemical analyses were performed on a subset of samples ($n = 284$). Pore-water pH decreased with depth by approximately 0.5 within the upper 10 m of the FFT. Major pore-water constituents included Na (880 ± 96 mg L^{-1}) and Cl (560 ± 95 mg L^{-1}); Ca (19 ± 4.1 mg L^{-1}), Mg (11 ± 2.0 mg L^{-1}), K (16 ± 2.3 mg L^{-1}) and NH_3 (9.9 ± 4.7 mg L^{-1}) were consistently observed. Iron and Mn concentrations were low within FFT pore water, whereas SO_4 concentrations decreased sharply across the FFT–water interface. Geochemical modeling indicated that $FeS_{(s)}$ precipitation was favoured under SO_4-reducing conditions. Pore water was also under-saturated with respect to gypsum [$CaSO_4 \cdot 2H_2O$], and near saturation with respect to calcite [$CaCO_3$], dolomite [$CaMg(CO_3)_2$] and siderite [$FeCO_3$]. X-ray diffraction (XRD) suggested that carbonate-mineral dissolution largely depleted calcite and dolomite. X-ray absorption near edge structure (XANES) spectroscopy revealed the presence of $FeS_{(s)}$, pyrite [FeS_2], and siderite. Carbonate-mineral dissolution and secondary mineral precipitation have likely contributed to FFT dewatering and settlement. However, the long-term importance of these processes within EPLs remains unknown. These results provide a reference for assessing the long-term geochemical evolution of oil sands EPLs, and offer insight into the chemistry of pore water released from FFT to the overlying water cover.

* Corresponding author at: 114 Science Place, Department of Geological Sciences, University of Saskatchewan, Saskatoon, Saskatchewan S7N 5E2, Canada.
E-mail address: matt.lindsay@usask.ca (M.B.J. Lindsay).

http://dx.doi.org/10.1016/j.scitotenv.2016.03.002
0048-9697/

McAnena, A., Poulton, S., 2013. Experimental dissolution of $FeCO_3$ under controlled sulfidic conditions. Mineral. Mag. 77, 1718.
Osacky, M., Geramian, M., Dyar, M.D., Sklute, E.C., Valter, M., Ivey, D.G., Liu, Q., Etsell, T.H., 2013a. Characterisation of petrologic end members of oil sands from the Athabasca region, Alberta, Canada. Can. J. Chem. Eng. 91, 1402–1415.
Osacky, M., Geramian, M., Ivey, D.G., Liu, Q., Etsell, T.H., 2013b. Mineralogical and chemical composition of petrologic end members of Alberta oil sands. Fuel 113, 148–157.
Parkhurst, D.L., Appelo, C.A.J., 2013. Description of input and examples for PHREEQC version 3—A Computer Program for Speciation, Batch-reaction, One-dimensional Transport, and Inverse Geochemical Calculations. U.S. Geological Survey Techniques and Methods, book 6, chap. A43 (497 pp., http://pubs.usgs.gov/tm/06/a43, accessed).
Postma, D., 1981. Formation of siderite and vivianite and the pore-water composition of a recent bog sediment in Denmark. Chem. Geol. 31, 225–244.
Prakash, S., Vendenberg, J.A., Buchak, E., 2011. The oil sands pit lake model — sediment diagenesis module. In: Chan, F., Marinova, D., Anderssen, R.S. (Eds.), MODSIM2011, 19th International Congress on Modelling and Simulation. Modelling and Simulation Society of Australia and New Zealand, Perth, Australia, pp. 3761–3767.
Prietzel, J., Thieme, J., Eusterhues, K., Eichert, D., 2007. Iron speciation in soils and soil aggregates by synchrotron-based X-ray microspectroscopy (XANES, μ-XANES). Eur. J. Soil Sci. 58, 1027–1041.
Ramesh Kumar, A., Riyazuddin, P., 2012. Seasonal variation of redox species and redox potentials in shallow groundwater: a comparison of measured and calculated redox potentials. J. Hydrol. 444–445, 187–198.
Ramos-Padrón, E., Bordenave, S., Lin, S., Bhaskar, I.M., Dong, X., Sensen, C.W., Fournier, J., Voordouw, G., Gieg, L.M., 2011. Carbon and sulfur cycling by microbial communities in a gypsum-treated oil sands tailings pond. Environ. Sci. Technol. 45, 439–446.
Ravel, B., Newville, M., 2005. ATHENA, ARTEMIS, HEPHAESTUS: data analysis for X-ray adsorption spectroscopy using IFEFFIT. J. Synchrotron Radiat. 12, 537–541.
Schwertmann, U., Cornell, R.M., 2000. Iron oxides in laboratory: preparation and characterization. Second, Completely Revised and Extended ed. WILEY-VCH Verlag GmbH, Weinheim.
Siddique, T., Fedorak, P.M., Foght, J.M., 2006. Biodegradation of short-chain n-alkanes in oil sands tailings under methanogenic conditions. Environ. Sci. Technol. 40, 5459–5464.
Siddique, T., Fedorak, P.M., MacKinnon, M.D., Foght, J.M., 2007. Metabolism of BTEX and naphtha compounds to methane in oil sands tailings. Environ. Sci. Technol. 41, 2350–2356.
Siddique, T., Penner, T., Semple, K., Foght, J.M., 2011. Anaerobic biodegradation of longer-chain n-alkanes coupled to methane production in oil sands tailings. Environ. Sci. Technol. 45, 5892–5899.
Siddique, T., Penner, T., Klassen, J., Nesbø, C., Foght, J.M., 2012. Microbial communities involved in methane production from hydrocarbons in oil sands tailings. Environ. Sci. Technol. 46, 9802–9810.
Siddique, T., Kuznetsov, P., Kuznetsova, A., Arkell, N., Young, R., Li, C., Guigard, S., Underwood, E., Foght, J.M., 2014a. Microbially-accelerated consolidation of oil sands tailings. Pathway I: changes in porewater chemistry. Front. Microbiol. 5 (Article 106).
Siddique, T., Kuznetsov, P., Kuznetsova, A., Li, C., Young, R., Arocena, J.M., Foght, J.M., 2014b. Microbially-accelerated consolidation of oil sands tailings. Pathway II: solid-phase biogeochemistry. Front. Microbiol. 5 (Article 107).
Silva, C.A.R., Liu, X., Millero, F.J., 2002. Solubility of siderite ($FeCO_3$) in NaCl solutions. J. Solut. Chem. 31, 97–108.
Stasik, S., Wendt-Potthoff, K., 2014. Interaction of microbial sulphate reduction and methanogenesis in oil sands tailings ponds. Chemosphere 103, 59–66.
Stasik, S., Loick, N., Knöller, K., Weisener, C., Wendt-Potthoff, K., 2014. Understanding biogeochemical gradients of sulfur, iron and carbon in an oil sands tailings pond. Chem. Geol. 382, 44–53.
Zeng, T., Arnold, W.A., Toner, B.M., 2013. Microscale characterization of sulfur speciation in lake sediments. Environ. Sci. Technol. 47, 1287–1296.
Zhang, J., Dong, H., Liu, D., Fischer, T.B., Wang, S., Huang, L., 2012. Microbial reduction of Fe(III) in illite–smectite minerals by methanogen *Methanosarcina mazei*. Chem. Geol. 292–293, 35–44.